CZECH TECHNICAL UNIVERSITY IN PRAGUE

Faculty of Nuclear Sciences and Physical Engineering

Department of Physics

Diploma thesis

Correlation femtoscopy in proton-gold collisions at the STAR experiment

Bc. Lukáš Holub

Supervisor: RNDr. Chaloupka Petr, Ph.D.

Prague, 2018

ČESKÉ VYSOKÉ UČENÍ TECHNICKÉ V PRAZE
Fakulta jaderná a fyzikálně inženýrská
Katedra fyziky

Diplomová práce

Korelační femtoskopie ve srážkách proton-zlato na experimentu STAR

Bc. Lukáš Holub
Vedoucí práce: RNDr. Petr Chaloupka, Ph.D.
Praha, 2018

Název práce:
Korelační femtoskopie ve srážkách proton-zlato na experimentu STAR

Autor: Lukáš Holub
Obor: Experimentální jaderná a částicová fyzika
Druh práce: Diplomová práca
Vedoucí práce: RNDr. Petr Chaloupka, Ph.D., Katedra fyziky, Fakulta jaderná a fyzikálně inženýrská, České vysoké učení technické v Praze

Abstrakt: Z predpovedi kvantovej chromdynamiky (QCD) existuje fázový prechod od stavu hadrónov do stavu neviazaných gluónov a kvarkov - quark-gluonová plazma (QGP). Tento stav hmoty existuje pri extrémne vysokej teplote alebo hustote. V súčastnosti je možné experimentálne vytvoriť QGP v laboratóriách, ako je BNL alebo CERN, v ktorých môžme študovať fázu hmoty v neviazanej oblasti QCD, formovanie hadrónovej hmoty a interakcie medzi hadrónmi. V tejto práci prezentujeme predbežnú analýzu korelačných femtoskopických meraní dvoch identických nabitých piónov z kolízií $p+Au$ pre $\sqrt{s_{NN}} = 200\,GeV$ z experimentu STAR v RHIC. Získané 1D korelačné funkcie vykazujú závislosť na multiplicite a na transverzálnej hybnosti páru. Taktiež sú fitované Gauss a Levy distribúciami s cieľom získať informácie o veľkosti systému v čase kinetického zmrazenia. Okrem toho sú konštruované aj 3D korelačné funkcie, ktoré vykazujú podobné správanie a umožňujú jasne sledovať silné nefemtoskopické účinky.

Klíčová slova: QCD, kvark-gluonová plazma, korelačná femtoskopia,

Title:

Correlation femtoscopy in proton-gold collisions at the STAR experiment

Author: Lukáš Holub

Abstract: According to prediction of the quantum chromodynamics (QCD) there is a phase transition from a state of hadrons to a state of deconfined gluons and quarks - the quark-gluon plasma (QGP). This state of matter exists at extremely high temperatures or densities. Nowadays, it is possible to create QGP in the laboratories such as BNL or CERN in which we can study a phase of matter in the deconfined region of QCD, the formation of hadronic matter and the interaction between hadrons. In this work, we present a preliminary analysis of the femtoscopy measurements of two identical charged pions from $p+Au$ collisions at $\sqrt{s_{NN}} = 200\,GeV$ from STAR experiment at RHIC. The obtained 1-dimensional correlation functions show dependence on multiplicity and transverse pair momentum. There are also fitted with Gauss and Levy distributions in order to extract an information about the size of the system at the time of kinetic freeze-out. Moreover, 3-dimensional correlation functions are constructed as well, showing a similar behavior and allowing to clearly observe strong non-femtoscopic effects.

Keywords: QCD, quark-gluon plasma, correlation femtoscopy

Acknowledgement:
I would like to thank my supervisor RNDr. Petr Chaloupka, Ph.D. for his instructions, advices and language corrections.

Contents

List of Figures

Chapter 1

Introduction

Quantum Chromodynamics (QCD) is a type of quantum field theory which describes the strong interaction between the fundamental particles, quarks and gluons. These particles make up hadrons, which are divided either into baryons (formed by three quarks such as the proton, neutron) or into mesons (formed by quark-antiquark pair such as the pion, kaon). Isolated quarks have not been observed so far.

In the prediction of QCD there is a possibility of transition from a state formed by hadrons to a state which is composed from deconfined quarks and gluons - the quark-gluon plasma (QGP). It is believed that this state of matter existed at the beginning of the Universe.

In present, QGP can be also created in laboratories where it can be studied. However, this system exists only for a very short period of time with typical space-time extents of the order of $10^{-15}\,m$. Using the correlation femtoscopy one can obtain information about the space-time characteristics of the system at the moment of particle emission.

This work presents a first analysis of femtoscopic correlations of two identical charged pion from $p{+}Au$ collisions at $\sqrt{s_{NN}} = 200\,GeV$. The whole thesis is divided into six chapters. In the first chapter we introduce a brief overview of the Standard Model, QCD and QGP. In the second chapter is a description of the geometry and space-time evolution of the collision. At the end of this chapter basic signatures of the QGP are discussed. The third chapter contains description of the STAR detector at RHIC. Theoretical backgrounds of femtoscopy are discussed in chapter four. Here, the derivation of the two-particle correlation function for identical particles as well as parametrization of the coordinate system are discussed. Then the main idea of the non-identical correlation femtoscopy is described. Subsequently, femtoscopy in the dynamical system and non-femtoscopic correlation are discussed. At the end of this chapter results from other femtoscopic experiments are shown. The last chapter summarizes our own analysis of the STAR experimental data. It discusses the applied selection criteria for construction of correlation functions and measurements. The correlation functions are extracted for several multiplicity and k_T bins. The measured 1-dimensional correlation functions are fitted by Gauss and Levy distributions. From these fits we obtain the parameters describing the extents of the particle-emitting sources. 3-dimensional correlation functions are extracted at the end of this chapter. Here the multiplicity and k_T dependence of these functions can be observed together with strong non-femtoscopic effects.

Chapter 2

Quark-gluon plasma

2.1 Standard model

The Standard model is a gauge field theory based on the symmetry group $SU(3) \otimes SU(2) \otimes SU(1)$ that was developed in stages from later half of the 20th century up to mid of 1970s. The purpose of this theory is to describe a relationship between **fundamental particles** that are governed by **fundamental interactions**. As we know the whole Universe has four fundamental interactions, namely

1. the Electromagnetic interaction
2. the Weak interaction
3. the Strong interaction
4. the Gravitational interaction.

The first three interaction can be "simply" and well described by the Standard model however this model omits the gravitational interaction. The problem is that the quantum theory describes micro-world while the general theory of relativity describes the macro-world and it is difficult to fit these two theories into the one single framework. In spite of the fact that we are not able to include one fundamental interaction into this model, it still works well because of the fact that for the minuscule scale of particles, the effect of gravity is so weak as to be negligible [18]. But this is not the only problem. There are also important questions that it does not answer, such as

- What is dark matter or dark energy?
- What happened to the antimatter after the big bang?
- Why are there three generations of quarks and leptons with such a different mass scale?

2.1.1 Fundamental particles

The term fundamental particles is a naming of group of particles whose substructure is unknown. In general, these particles can be divided into two subgroups: the fundamental fermions and the fundamental boson.

Fundamental fermions

Fundamental fermions are particles with spin of 1/2 that respect the Pauli exclusion principle. These particles can be splitted into two groups called quarks and leptons. There are six particles in each group which are grouped into three generations.

The quarks are distinguished according their flavor as

$$\begin{matrix} u & c & t \\ d & s & b. \end{matrix}$$

Each quark carries a fraction of the elementary charge either (2/3) or (−1/3) and one of the three colors: red, green, or blue. In nature the quarks have never been observed individually, but only inside bound colorless strongly interacting particles called hadrons which are divided into mesons and baryons. Mesons are bound states of quark-antiquark pairs while baryon are bound states of three quarks.

The leptons are also grouped into the three generations where each generation consists of one lepton and its corresponding neutrino.

$$\begin{matrix} e^- & \mu^- & \tau^- \\ \nu_e & \nu_\mu & \nu_\tau. \end{matrix}$$

Electron, muon and tau carry the elementary charge while corresponding neutrinos carry no charge.

For every quark and lepton there is also a corresponding antiparticle, the particle with the same mass and opposite charge.

Fundamental bosons

The fundamental bosons are vector particles with a spin of 1 that carry any of the fundamental interactions of the nature. This class contains gluon (g), photon (γ), Z boson (Z^0) and W boson ($W^\pm$). The massless electrically neutral photon is associated with the electromagnetic interaction. The gluons are mediators of the strong interaction while the massive electrically neutral Z bosons and electrically charged $W^\pm$ bosons mediate the weak interaction.

The Higgs boson (H) is the massive scalar spin-zero elementary particle that explains why the other elementary particles, except the photon and gluon, are massive.

Following figure (Fig.2.1) shows the overview of all previously discussed fundamental particles and their properties.

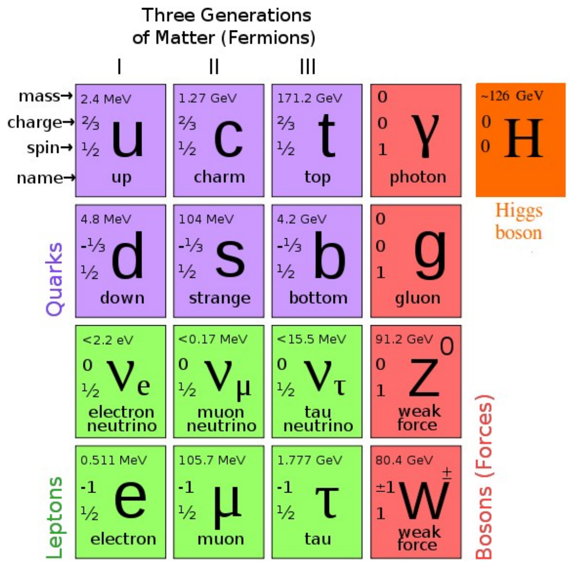

Figure 2.1: Fundamental particles in the Standard model and their properties. Taken from [16].

2.1.2 Fundamental interactions

As we mentioned above the Standard model contains three fundamental interactions, namely strong, weak and electromagnetic. Each of these interactions is characterized by the corresponding gauge theory with a symmetry group and can be explained as exchange of mediators, the already discussed gauge bosons.

The mediator of the electromagnetic interaction is the photon and this interaction is described by the Quantum Electrodynamics (QED) that is an abelian gauge theory with the symmetry group U(1). Since the photon has zero mass, the range of this force is infinity. The QED Lagrangian for a spin-1/2 field interacting with the electromagnetic field is given in natural units by the real part of

$$\mathcal{L}_{EM} = \bar{\psi}(i\gamma^{\mu}(\partial_{\mu} + ieA_{\mu} + ieB_{\mu}) - m)\psi - \frac{1}{4}F_{\mu\nu}F^{\mu\nu}, \tag{2.1}$$

where γ^{μ} are Dirac matrices, ψ is a bispinor field of spin-1/2 particle (e.g. electron/positron field), A_{μ} is the covariant four-potential of the electromagnetic field generated by the electron itself, B_{μ} is the external field imposed by external source and $F_{\mu\nu}$ is the electromagnetic field tensor.

The weak interaction is mediated by the massive $W^{\pm}$ and Z bosons, and therefore the range of this force is very short. The theory of the weak interaction is called quantum flavourdynamics (QFD). However, the term QFD is rarely used because the weak interaction is best understood in terms of electro-weak theory (EWT). The non-abelian gauge theory EWT is a quantum field theory that is unified description of electromagnetism and weak interaction. The unification is accomplished under an $SU(2)_L \otimes U(1)$ gauge symmetry group. The corresponding gauge bosons are the three

W bosons of weak isospin from SU(2) (W_1, W_2, and W_3), and the B boson of weak hyper-charge from U(1) all of which are massless. From the combination of these gauge bosons, one is able to obtain $W^{\pm}$, Z^0 and γ bosons. The general form of Lagrangian for the EWT can be written as

$$\mathcal{L}_{EW} = \mathcal{L}_K + \mathcal{L}_N + \mathcal{L}_C + \mathcal{L}_H + \mathcal{L}_{HV} + \mathcal{L}_{WWV} + \mathcal{L}_{WWVV} + \mathcal{L}_Y, \tag{2.2}$$

where $\mathcal{L}_K$ is the kinetic term that contains all the quadratic terms of the Lagrangian, which include the dynamic terms and the mass terms, $\mathcal{L}_N$ and $\mathcal{L}_C$ contain the interaction between the fermions and gauge bosons, $\mathcal{L}_H$ contains the Higgs three-point and four-point self interaction terms, $\mathcal{L}_{HV}$ contains the Higgs interactions with gauge vector bosons, $\mathcal{L}_{WWV}$ contains the gauge three-point self interactions, $\mathcal{L}_{WWVV}$ contains the gauge four-point self interactions, $\mathcal{L}_Y$ contains the Yukawa interactions between the fermions and the Higgs field.

The last fundamental force, which is contained in the Standard model, is the strong interaction with gluons as the mediators. Although the gluons are also massless particles like the photons, the strong interaction can reach up only units of fermi - $10^{-15}\,m$. This behavior is quite interesting and can be explained by the quantum chromodynamics (QCD), which will be discussed in detail in the following section.

Although the Standard model does not contain the gravitation force and its presumed mediator the graviton and can not give an explanation of some phenomena it is one of the most widely accepted theoretical models in the particle physics.

Table 2.1 shows the summary of the fundamental interactions, their mediators and the ranges.

Fundamental fource	Exchange boson	Mass (in MeV/c^2)	Expected range
Electromagnetic	Photon (γ)	0	∞
Weak	$W^{\pm}$, Z^0	$W^{\pm} = 80600$ $Z^0 = 93160$	$10^{-17} - 10^{-16}\,m$
Strong	Gluon (g)	0	$10^{-15}\,m$
Gravity	? Graviton ?	Not known to exist expected 0	∞

Table 2.1: Fundamental interactions in the Standard model and their properties.

2.2 Quantum chromodynamics

The quantum chromodynamics (QCD) is the non-abelian gauge theory that describes the strong interaction, between quarks and gluons, with the SU(3) symmetry group.

As mentioned above, the mediators of this fundamental force are the massless gluons that carry the supplementary color (anti-color) charge. There are three different color charges (red, green and blue) that create eight different gluons that occur in our world. The quarks interact with each other, with the possibility to change the relevant color [10]. Since leptons do not interact with gluons, they are not affected by this sector. The QCD Lagrangian of the quarks coupled to the gluon fields is given by

$$\mathcal{L}_{QCD} = \sum_{\psi} \bar{\psi}_i (i\gamma^\mu(\partial_\mu \delta_{ij} - i g_s G^a_\mu T^a_{ij}) - m_\psi \delta_{ij})\psi_j - \frac{1}{4} G^a_{\mu\nu} G^{\mu\nu}_a, \tag{2.3}$$

where ψ_i is the Dirac spinor of the quark field and i=(r,g,b) represents color, γ^μ are the Dirac matrices, G^a_μ is the 8-component (a=1,2,3,...8) SU(3) gauge field, T^a_{ij} are 3x3 Gell-Mann matrices (generators of the SU(3) color group), $G^a_{\mu\nu}$ are the field strength tensors for the gluons and g_s is the strong coupling constant.

2.2.1 The QCD coupling constant

The strength of the strong interaction is encoded into a factor which is called the coupling constant that is usually denoted as α_s. The exchange of one gluon is proportional to a factor $g_s^2 = 4\pi\alpha_s$. Each of the two vertices where the gluon and the quark get in touch contributes a factor of $g_s = \sqrt{4\pi\alpha_s}$. [2]

In QCD the coupling constant α_s actually is not a constant at all because it effectively depends on the transferred four-momentum Q as [15].

$$\alpha_s(Q^2) = \frac{\alpha_s(\mu^2)}{1 + \beta_0 \alpha_s(\mu^2) \ln\left(\frac{Q^2}{\mu^2}\right)} \quad with \quad \beta_0 = \frac{11N_c - 2n_f}{12\pi} \tag{2.4}$$

where N_c is the number of colors (3 - red, green, blue) and n_f is the number of flavours (6 in the Standard model), μ^2 is called renormalization scale that is introduced by the renormalization process.

For comparison, in the quantum electrodynamics (QED) the coupling constant, better known as *fine structure constant*, is

$$\alpha(Q^2) = \frac{\alpha(\mu^2)}{1 + \beta_0 \alpha(\mu^2) \ln\left(\frac{Q^2}{\mu^2}\right)} \quad with \quad \beta_0 = -\frac{1}{3\pi}. \tag{2.5}$$

We know that the running QED coupling constant decreases with decreasing Q^2 to the asymptotic value $\alpha(0) \approx 1/137$. However, running QCD coupling constant increases with decreasing Q^2 and for small values of Q^2, α_s can be about 50 times greater than QED coupling constant and that is why the strong interaction is strong.

This behavior of the α_s results in the confinement of quarks and explains the fact that they are never seen in isolation but only in strongly interacting matter. Let us demonstrate the main idea of the color confinement.

Suppose, we have a quark-antiquark pair which is in a color singlet state. One may try to separate the quark from the antiquark by pulling them apart. The interaction between the quarks gets stronger as the distance between them gets larger, similar to what happens in the spring. In fact, when a spring is stretched beyond the elastic limit, it breaks to produce two springs. In the case of the quark pair, a new quark-antiquark pair will be created when pulled beyond certain distance. Part of the stretching energy goes into the creation of the new pair, and as a consequence, one can not have quarks as free particles, see in (Fig.2.2, right panel).[1]

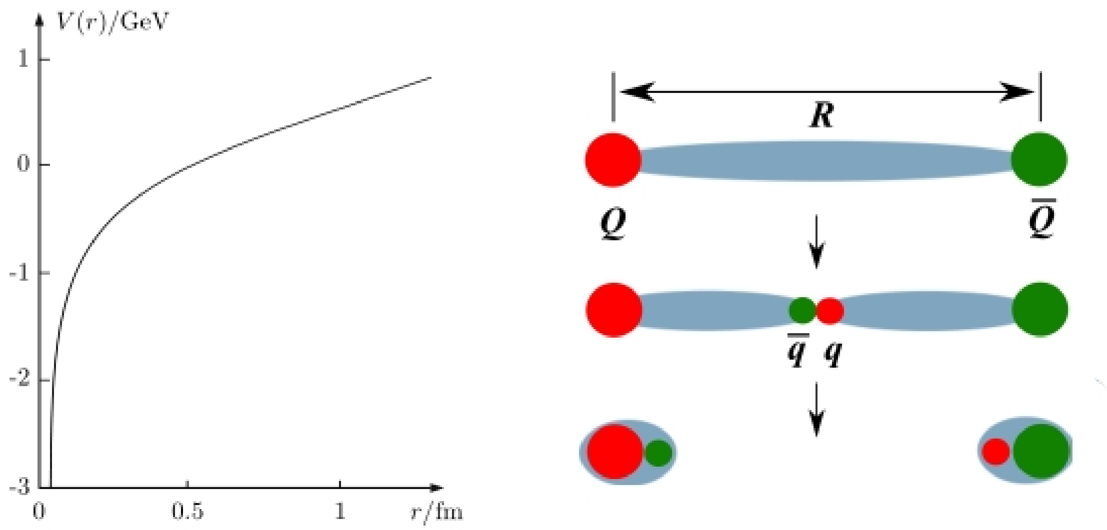

Figure 2.2: **Left)** The behavior of potential between quark-antiquark pair. **Right)** The QCD string between the static quark-antiquark pair breaks due to light quark-antiquark pair creation. Taken from [43]

The above discussion was only for imagination. However, to understand what really happens, one must make very difficult calculations in QCD. It can be shown that the effective quark-antiquark potential is well approximated by Cornell potential [79], see in (Fig.2.2, left panel)

$$V(r) = -\frac{4\alpha_s}{3r} + kr \tag{2.6}$$

where k is the string tension that represents the strength of the quark confinement, r is the distance between quarks and α_s is the coupling constant.

The first term of the potential is well known Coulomb-like potential that depends on the factor $1/r$. The second term, a string potential, is more interesting because this term causes the fact that quarks can never be seen in isolation under normal conditions.

However, at very large Q, the coupling strength between color charged particles is so small that quarks and gluons can be thought to be free particles. This property of the strong interaction is known as asymptotic freedom. The α_s lies in the range $0.1 - 0.3$ at values of Q that can be probed experimentally, see in (Fig.2.3).

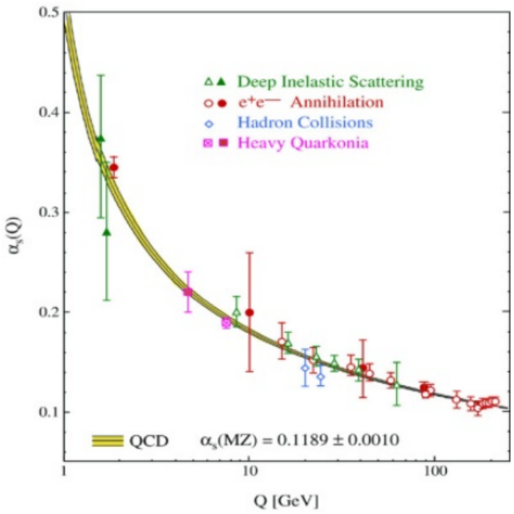

Figure 2.3: It shows a compilation of the values for α_s, derived from many different experiments, and for different momenta Q of the exchanged gluons. Taken from [6]

2.3 Quark-gluon plasma

According to prediction of the QCD there is a possible state of matter that is no longer confined in the hadron interiors but can propagate in the whole volume occupied by the system. This state of matter is called quark-gluon plasma (QGP) and can exist at extremely high temperature or density. At these extreme conditions the QCD predicts a phase transition from hadronic state to the QGP. An example of the phase transition can be seen in (Fig.2.4). However, one can ask himself whether the existence of such a state of matter is not in conflict with the confinement hypothesis. We note that the plasma is white as a whole. Thus, the color charges are still confined in the colorless system.

Due to the difficulty of calculations of the soft QCD, the properties of the hadronic matter are poorly known at the moderate temperatures. This difficulty lies in the strength of the strong interaction. While the perturbative expansion, where the system is treated as non-interacting, appears to be the only effective and universal computational method in the quantum field theory, a large value of the QCD coupling constant excludes applicability of the method for the system of quarks and gluons. However, the QCD possesses a remarkable property, that we mentioned above, called the asymptotic freedom. Therefore, the interactions with a large momentum transfer can be treated in the perturbative way [63].

An increase of the transferred momentum can be done by increase of the temperature of the whole system. According to lattice QCD calculations the critical temperature of the phase transition is around $T_c \approx 170\,MeV$. At this temperature the energy density is $\epsilon_c \sim 1\,GeV/fm^3$ and we expect to achieve the asymptotic freedom regime (smallness of the coupling constant) [10] where the QGP is created. The QGP can be also established during the adiabatic compression of the nuclear matter at the temperature $T \approx 0\,MeV$. Since it is believed that the system can reach such a high baryon chemical density μ_B, where the binding between the quarks will be broken up and the QGP will be formed. In the (Fig.2.5) is shown a phase diagram of QCD and in (Fig.2.6) two ways of production of the QGP are sketched.

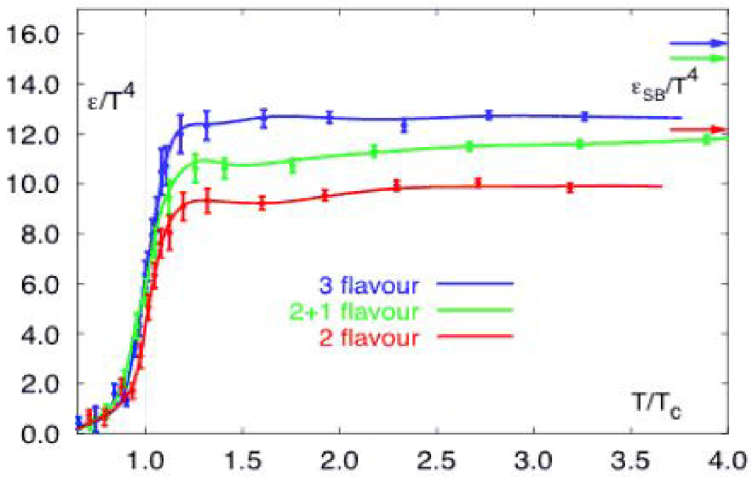

Figure 2.4: The energy density divided by the 4th power of the temperature, computed on the lattice with different number of sea flavours, shows a marked rise near the critical temperature. The arrows on top show the limit for a perfect Bose gas. Taken from [34].

It is believed that in the first moments of the Universe, a few microseconds after the Big Bang, the temperature and pressure of the matter were sufficient high to create a deconfined state of quarks and gluons. At the present time, such conditions are not very usual in the nature. One of the places where the QGP could exist are the centers of the neutron stars. However, more convenient is to observe the QGP in the early moments of the ultra relativistic heavy-ion collisions. This deconfined medium exists only for a fleeting moment of few femtoseconds so it is impossible to directly observe QGP within this small lifetime. However the detection of various particles from QGP might prove to be useful as signatures and plasma diagnostic tools. It is recognized that there may be no unique signal which will alone lead to the identification of quark gluon plasma. Instead, a number of different signals come out from the medium which may

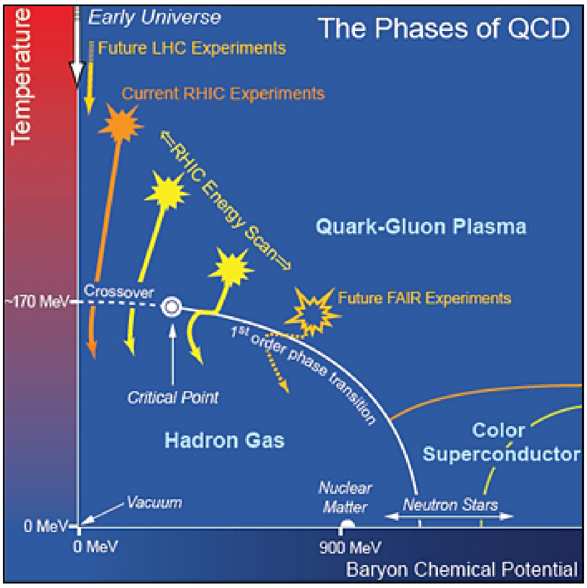

Figure 2.5: Schematic QCD phase diagram for nuclear matter. The solid lines show the phase boundaries for the indicated phases. The solid circle depicts the critical point. Taken from [8].

be treated as the QGP signatures. These signals include, for example enhancement of direct photons and dileptons due to QGP thermal radiation, strangeness enhancement, J/ψ suppression, jet quenching, elliptic flow or heavy quarks and more. Some of them will be discussed in the next chapter.

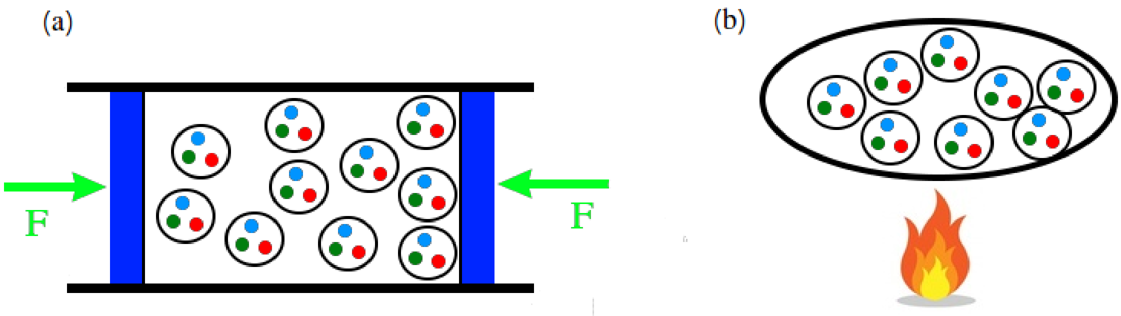

Figure 2.6: Sketch of two principles to produce the dense hadronic matter: compression (a) and heating (b).

Chapter 3

Heavy-ion collisions

In order to change the hadronic matter into the phase of deconfined quarks and gluons, the temperature of the system must be above T_c and density above ϵ_c. To reach such a temperature and density on the Earth, the ultra relativistic heavy-ion collisions are used. In laboratories like CERN (Geneva, Switzerland), BNL (New York, USA), GSI (Darmstadt, Germany), and GANIL (Caen, France), nuclei are accelerated at energies that range from MeV to TeV beam energies.

3.1 Geometry of heavy-ion collision

Geometry of the collision in relativistic heavy-ion collisions is characterized by a degree of the overlap of the two nuclei. The distance parameter $|\vec{b}|$ is a parameter which characterizes the overlapping region and is defined as the distance between the center of nuclei, where $\vec{b}$ is perpendicular to the beam direction. A pictorial view of relativistic heavy-ion collisions is presented in (Fig.3.1).

In the region of overlapping, the participating nucleons interact with each other, while in non-overlapping region, the spectator nucleons continue along their trajectories [87]. However, it is impossible to measure the impact parameter directly in the experiment. Therefore the *centrality* (c) is defined and measured instead of the impact parameter

$$c = \frac{\int_0^b \frac{d\sigma}{da} da}{\int_0^\infty \frac{d\sigma}{da} da}. \tag{3.1}$$

The most central collisions correspond to $|\vec{b}| \sim 0\, fm$, or in another words, head-on collisions. On the other hand, no overlapping area is for the most peripheral collisions correspond to $|\vec{b}| \sim 2R\, fm$, where R is radius of the nucleus. Nuclei are Lorenz contracted in beam direction therefore the maximum time of overlapping is determined as $\tau = \frac{2R}{\gamma c}$, where γ is Lorentz factor and c is speed of light.

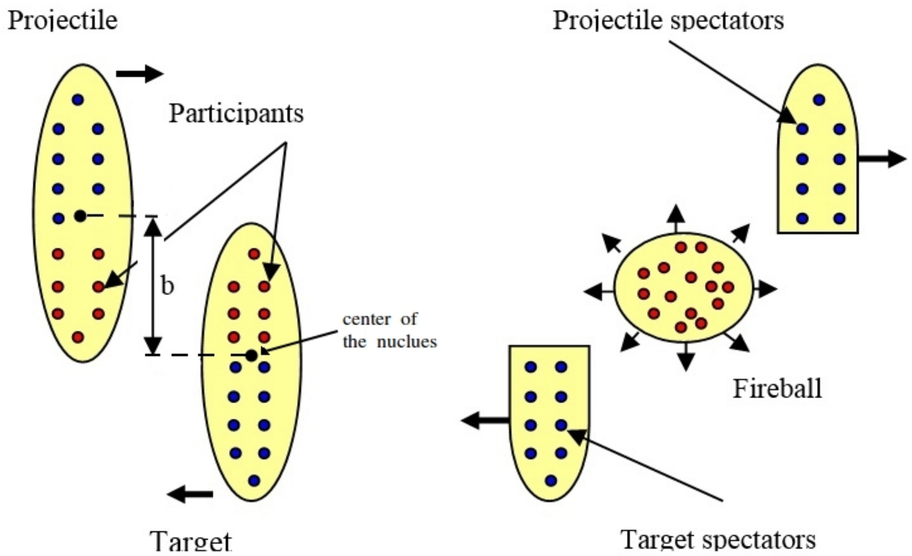

Figure 3.1: Nucleus-nucleus collision with impact parameter b.

3.2 Space-time evolution of the collision

Different phases of evolution of the collision are predicted according to theoretical models and on the basis of data collected so far. Nuclei that are accelerated to ultra relativistic energies become Lorentz-contracted. In heavy-ion collisions, a large number of nucleons is involved in the processes while the collision takes place in a very tight region.

As is mentioned in previous chapter, the formation of the QGP is possible only if critical temperature and energy density are reached. If the system does not reach such conditions after collision of the nuclei then the system will run into a hadron gas that is not too interesting in study of the QGP, the left side of the (Fig.3.2).

In the right side of the (Fig.3.2), it is shown the evolution of the heavy-ion collision in the case of the QGP formation. This evolution can be divided into the following phases.[5]

- Pre-equilibrium - nuclei pass through each other and partons (quarks and gluons) scatters among each other and give rise to an abundant production of deconfined quarks and gluons. During the scattering, partons lose part of their initial energy in the interaction region, creating fireball. At this stage a large quantity of photons is also produced, direct photons that are real or virtual. Virtual photons decay in lepton-antilepton pairs.

- Thermalization - elastic and inelastic interactions between partons in QGP lead to the thermalization phase. Inelastic interactions can modify the flavour composition of particles. Due to its internal pressure, the system at thermal equilibrium rapidly expands. While expanding, system cools down.

- Hadronization - the expanding system of QGP cools down and reaches the transition temperature. At this point the hadronization begins and quarks and gluons of the QGP condensate into new hadrons.

- Chemical freeze-out - the system expands further and get to the temperature of chemical freeze-out T_{ch}. The composition of the hadrons do not change anymore. However, they collide elastically.

- Thermal freeze-out - if the temperature of the thermal freeze-out T_f is reached, elastic scatterings between hadrons cease and kinematical spectra of the resulting matter also become fixed, After this moment, hadrons fly out freely.

There are three characteristic times during the evolution. The first one is *initial formation time* (τ_0), at this time the pre-equilibrium stage of the collision ends. The second time is *chemical freeze-out time* (τ_{ch}), where inelastic collisions cease and chemical composition of the matter is fixed. The last one is *thermal freeze-out time* (τ_f), when system is so diluted that even elastic collisions cease.

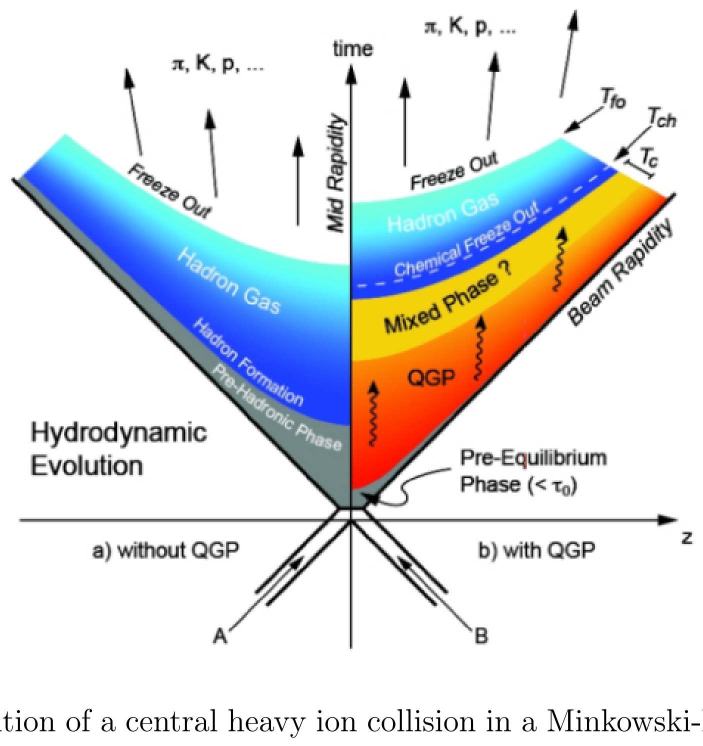

Figure 3.2: Evolution of a central heavy ion collision in a Minkowski-like plane. Taken from [5]

As mentioned above, the only way how we can get any information about the QGP is to inferred them from the properties of the particles remaining after the thermal freeze-out. In next section, we described some signatures of the QGP.

3.3 Signatures of the QGP

In this section we introduce some experimental observables that can provide information about the possible QGP phase.

3.3.1 Direct photon

As every thermal source the QGP also emit thermal radiation, real and virtual photons which are produced in quark-antiquark annihilation ($q\bar{q} \to g\gamma$) and Compton scattering ($g\bar{q} \to \gamma q$) processes, see in (Fig.3.3). These direct photons only interact through electromagnetic interaction and have a large mean free path compared to the size of the fireball so they escape the system without re-scattering carrying information on the earliest deconfined stage. [61]

At high p_T, direct photon production is dominated by hard scattering processes and can thus be used to study the validity of binary or N_{coll} scaling of high p_T particle production. At low p_T, direct photons are produced in the QGP and the hadron gas phase. However, measuring direct photons experimentally is difficult because there is also large background of photons which are emitted during the hadronic gas phase. Owing to this difficulty it is not easy to extract clear spectra of direct photons from the QGP because there is a lot of other processes that create large photon background.

In (Fig.3.4) one can see nuclear modification factor R_{AA}, for ALICE data that were measured in $Pb+Pb$ collisions at $\sqrt{s_{NN}} = 2.76\,TeV$. R_{AA} was used to quantify nuclear effects in heavy-ion collisions. It was calculated for direct photons using the pQCD calculation from [67] as pp reference. R_{AA} shows strong enhancement of the direct photon production at low p_T over the expectation from N_{coll} scaled pp collisions, as well as the validity of binary scaling at high p_T. These data were compared to various models that incorporate a QGP and found to be consistent with the measurement [72].

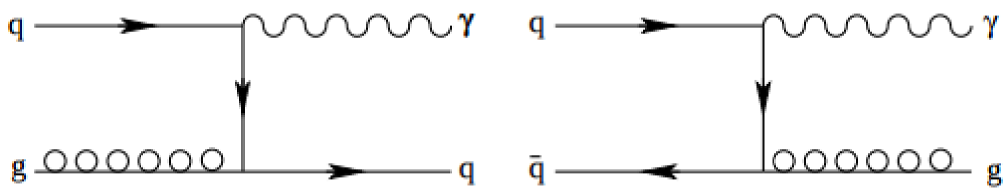

Figure 3.3: Lowest order contributions to photon production from the QGP: Compton scattering (left) and quark-antiquark annihilation (right). Taken from [75]

3.3.2 Strangeness enhancement

In elementary particle collisions, the strange quarks can be produced only as constituents of strange hadrons. In case that the QGP is formed, the pairs of strange and

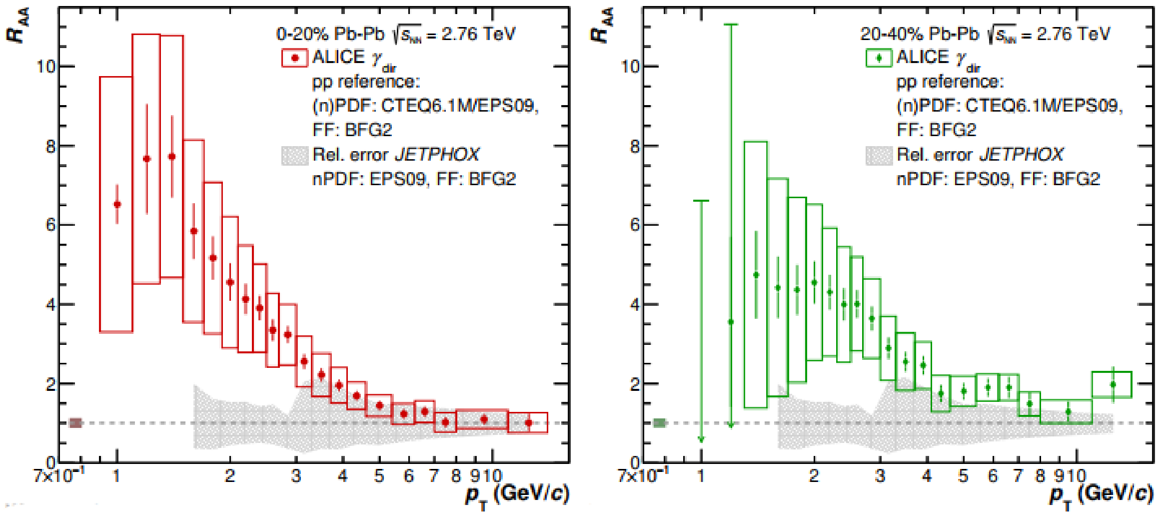

Figure 3.4: Nuclear modification factor R_{AA} for the $0-20\%$ (left) and $20-40\%$ (right) centrality classes. Taken from [72]

anti-strange quarks may be also produced by the gluon fusion without any additional non-strange quarks. Since the threshold for such a reaction is about $200\,MeV$, which is on the order of the expected QGP temperature, an enhancement of strangeness production should be observed [85].

In (Fig.3.5) the yields per wounded nucleon relative to $p{+}Be$ of Λ, Ξ and Ω and their anti-particles in $Pb{+}Pb$ and $p{+}Pb$ at $158\,A\,GeV/c$ are plotted as a function of the number of wounded nucleons. Wounded nucleon is the nucleon which undergo at least one primary inelastic collision with another nucleon. The enhancements are shown separately for particles containing at least one valence quark in common with the nucleon (left) and for those with no valence quark in common with the nucleon (right), since it is known that the particles of two groups may exhibit different production features. One can see, within the $Pb{+}Pb$ sample, an increase of the particle yields per wounded nucleon with the number of wounded nucleons for all the particles except for the $\bar{\Lambda}$. [40].

Similar effect can be seen in ratio of ϕ/π^- as a function of the center-of-mass energy per nucleon pair ($\sqrt{s_{NN}}$). The ratio ϕ/π^- increases with energy in $A + A$ and also in $p + p$ collisions. This indicates that the yield of the ϕ increases faster than yield of the π^-, see in (right Fig.3.6). Dependence of the ratio ϕ/π^- as a function of N_{part} for five different collisions can be seen in (left Fig.3.6). We see that the ratio first increases with N_{part} and then seems to be saturated in the high N_{part} region. This enhancement of the production of ϕ meson in heavy-ion environment has been predicted to be a signal of QGP formation [20].

Another interesting ratio, which can give us information about the transition from the hadron matter to deconfined matter of the quarks and gluons, is K^+/π^+. It was

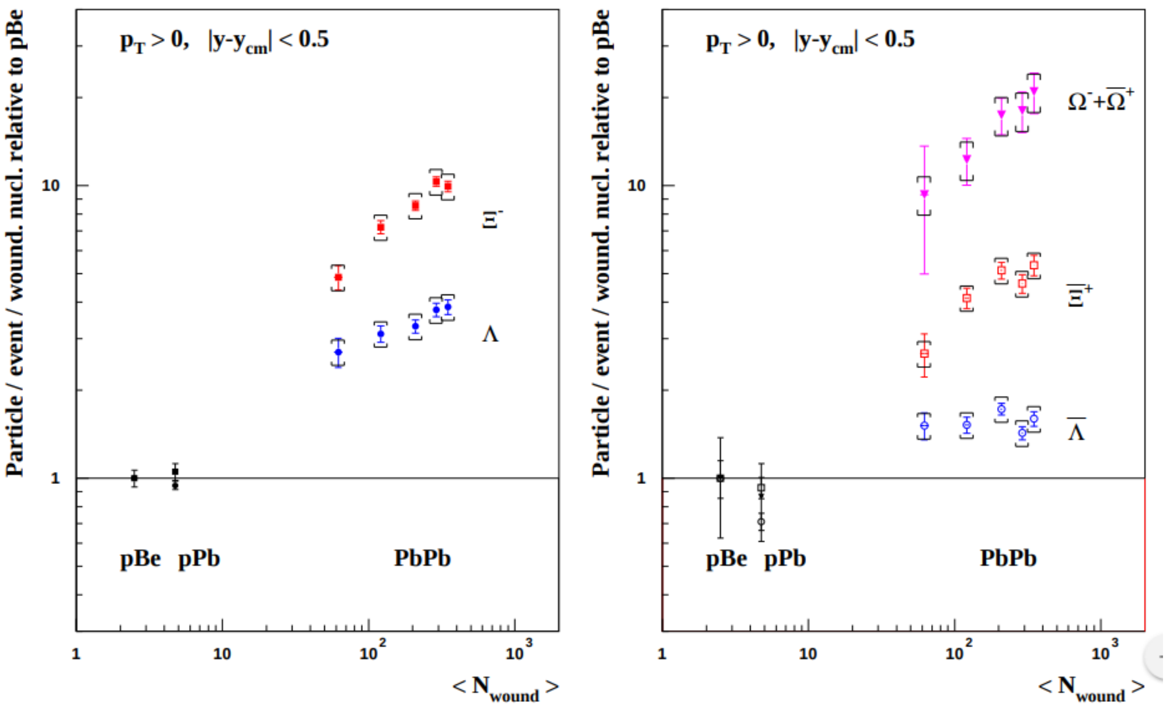

Figure 3.5: Hyperon yields per wounded nucleon per unit of rapidity at central rapidity relative to p+Be as a function of the number of wounded nucleons. Taken from [40].

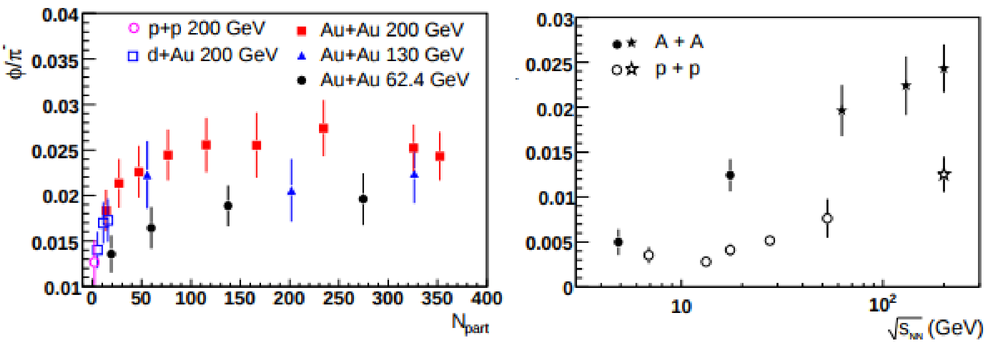

Figure 3.6: Right figure: Energy dependence of the ratio ϕ/π in $A + A$ and $p + p$ collisions. Stars data were measured at STAR experiment at RHIC. Left figure: Dependence of the ratio ϕ/π as a function of N_{part} for different collision systems. Both figure were taken from [20].

suggested in [48] and [49] that the transition to a deconfined state of matter may cause anomalies in the energy dependence of pion and strangeness production in nucleus-nucleus collisions. The ratio K^+/π^+ reflects the strangeness content relative to entropy in heavy-ion collisions compared to p+p collisions. Fig.3.7 shows the energy dependence of K/π particle ratio. RHIC BES results are compared with those from AGS, SPS and LHC. Data for BES Au+Au collisions are found to be consistent with the previous experiments. The peak position in energy dependence of K^+/π^+ has been suggested as the signature of a phase transition from hadron gas to a QGP, for more details about analysis and results see [24].

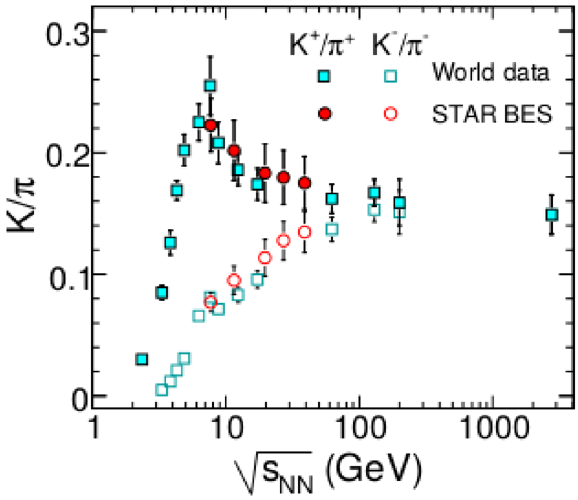

Figure 3.7: K/π ratio for central $0-5\%$ $Au{+}Au$ collisions at $\sqrt{s_{NN}} = 7.7, 11.5, 19.6, 27$ and $39\,GeV$ that are compared to previous result from AGS, SPS, RHIC and LHC. Taken from [24].

3.3.3 Quenching of the high p_T particles

High p_T particles traverse through the dense hot medium that was formed in collisions. In this medium particles lose their energy via strong interactions. The energy loss should be proportional to the initial gluon density and the lifetime of the system. Therefore, one can expect a suppression of high p_T hadrons in the final state. The suppression of the high p_T particles in A+A collisions compared to N_{coll} scaled p+p measurements is one of the best evidence for production of the QGP. Observing of this suppression can be done by the nuclear modification factor R_{AA} that is defined as [74]

$$R_{AA}(p_T) = \frac{(1/N_{AA})d^2N_{AA}/dp_Tdy}{\langle N_{coll}\rangle(1/N_{pp})d^2N_{pp}/dp_Tdy}. \tag{3.2}$$

However, if the particle yield from reference p+p collisions is not known one can use particle yield from the peripheral collisions and compare it with particle yield from the central collisions

$$R_{CP} = \frac{\langle N_{coll}\rangle_{peripheral}(1/N_{AA}^{central})d^2N_{AA}^{central}/dp_Tdy}{\langle N_{coll}\rangle_{central}(1/N_{AA}^{peripheral})d^2N_{AA}^{peripheral}/dp_Tdy}, \tag{3.3}$$

where N_{coll} is the average number of binary collisions within a centrality bin and can be estimated using a Glauber Monte Carlo.

Effects that increase the number of particles per binary collision in central heavy-ion collisions (or A+A collisions) relative to peripheral collisions (or p+p collisions) are collectively called enhancement effects and lead to $R_{CP} > 1$ ($R_{AA} > 1$) and opposite effects that decrease number of particles per binary collisions are collectively called suppression effects and lead to $R_{CP} < 1$ ($R_{AA} < 1$).

However, there are some effects that can lead to enhancement of hadron production in specific kinematic ranges, concealing the turn-off of the suppression. The effects that may cause such an enhancement are Cronin effect [21], radial flow and particle coalescence [50]. These enhancement effects are expected to compete with the suppression, which shifts high-p_T particles toward lower momenta. This means that measuring a nuclear modification factor to be greater than unity does not automatically lead us to conclude that a QGP is not formed. Disentangling these competing effects may be accomplished with complementary measurements, such as event plane dependent nuclear modification factors [31], or through other methods.

In (Fig.3.8) we can see R_{CP} dependence on the $\sqrt{s_{NN}}$ and p_T for data from $(0-5\%)$ and $60-80\%$ event centralities. The R_{CP} is found to be lowest at the highest beam energy studied, and increases progressively from a suppression regime at 62.4 GeV to a pronounced enhancement at the lowest beam energies. For more details see [26].

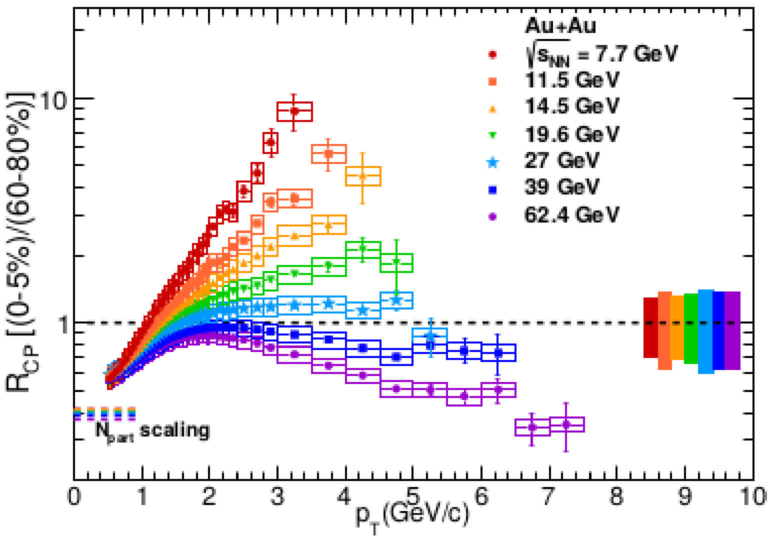

Figure 3.8: Charged hadron R_{CP} for RHIC BES energies. Taken from [26].

3.3.4 Elliptic flow

Another QGP signature which will be discussed is the elliptic flow. In the non-central collisions ($b \not\approx 0$) the overlapping region of two nuclei has a spatial anisotropy like an almond shape as is illustrated in (Fig.3.9, left). Thanks to this spatial anisotropy the pressure gradient is not azimuthally symmetric and establishes a correlation between momentum and position points [87]. The pressure gradient is bigger in the direction of the short X-axis than in the direction of the long Y-axis. Therefore more particles are emitted to the direction of the short axis. In other words, the initial spatial anisotropy makes an anisotropy in final momentum space as shown in (Fig.3.9, right).

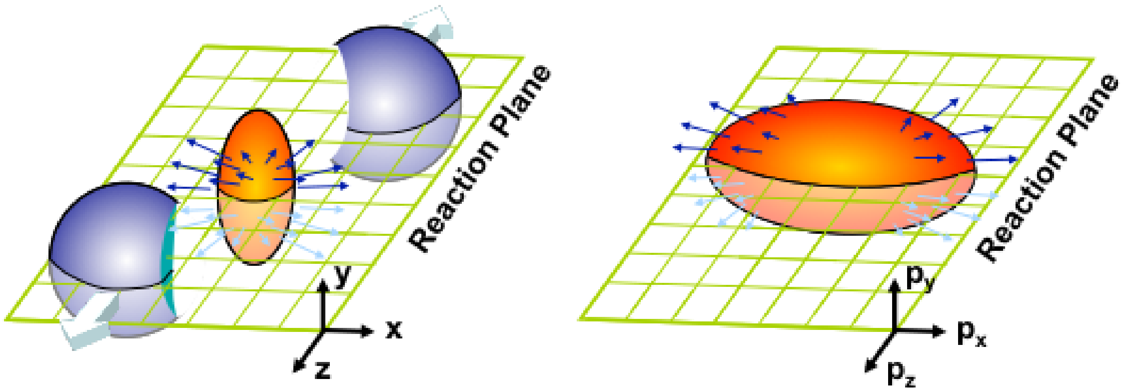

Figure 3.9: **Left** Overlapping region of two nuclei in non-central collisions in coordinate space. **Right** Anisotropy in momentum space due to spatial anisotropy.

Azimuthal distribution of emitted particles is represented in the form of Fourier expansion

$$\frac{Ed^3N}{dp^3} = \frac{d^3N}{2\pi p_T dp_T dy}[1 + 2v_1 \cos(\phi - \Phi_R) + 2v_2 \cos[2(\phi - \Phi_R)] + ...] \tag{3.4}$$

where p_T is the transverse momentum, y is the rapidity, ϕ the azimuthal angle of the outgoing particle, Φ_R is the azimuthal angle of the reaction plane in the laboratory frame. The Fourier coefficient v_2 represents the strength of the elliptic flow. The terms, $\sin[n(\phi - \Phi_R)]$, are not included in the Fourier expansion because they vanish due to the reflection symmetry with respect to the reaction plane, see (Fig.3.10). The reaction plane angle Φ_R, (Fig.3.10, right), is not known, and is estimated using the transverse distribution of particles in the final state. The estimated reaction plane is called the event plane [54].

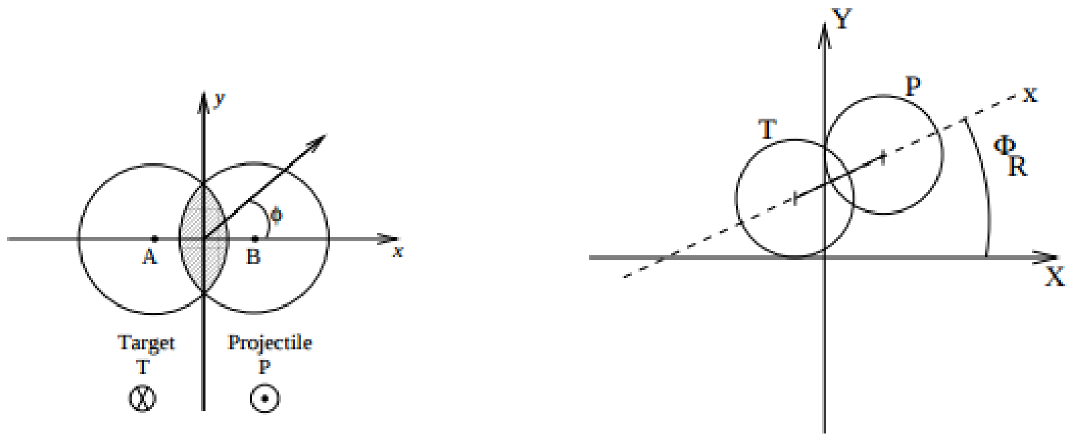

Figure 3.10: **Left** Geometry of the collision and ϕ, the azimuthal angle of one of the outgoing particles. **Right** Φ_R, the reaction plane angle. Taken from [54]

Fig.3.11 shows energy dependence of the v_2 of the particles π^+, K_s^0, proton and deuteron as a function of p_T for minimum bias $Au{+}Au$ collisions. Mass ordering of $v_2(p_T)$ for $p_T < 2.0\,GeV/c$ is clear where heavier species have a lower v_2 in this p_T range.

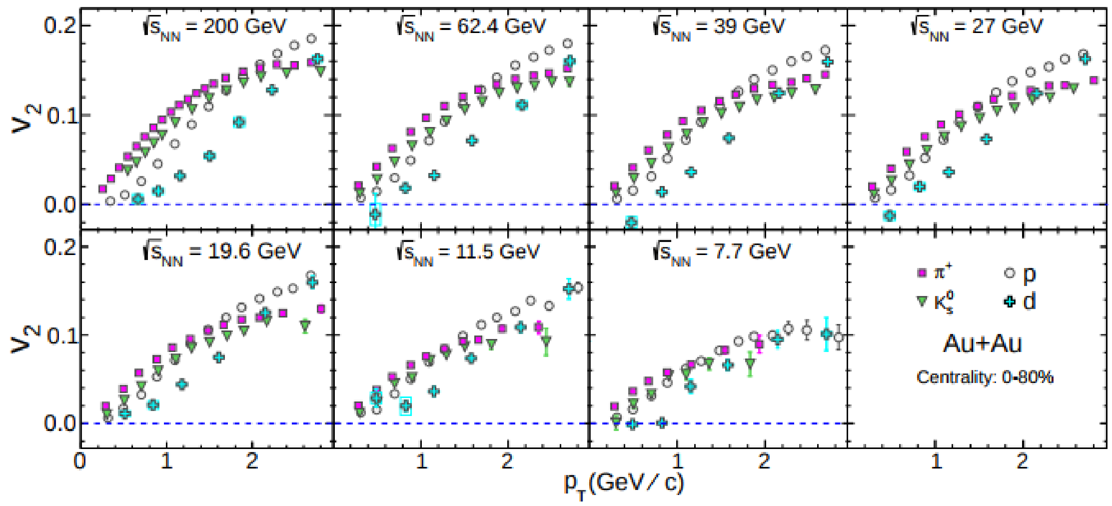

Figure 3.11: Mid-rapidity $v_2(p_T)$ for π^+, K_s^0, proton and deuteron for minimum bias $Au{+}Au$ collisions at $\sqrt{s_{NN}} = 200$, 62.4, 39.27, 19.6, 11.5 and $7.7\,GeV$. Taken from [23].

In the (Fig.3.12) we can see a comparison for measured D^0 v_2 for $10-40\%$ centrality bin with v_2 of K_s^0, Λ and Ξ^-. Panel (a) shows v_2 as a function of p_T where a clear mass ordering for $p_T < 2\,GeV/c$ is observed. For $p_T > 2\,GeV/c$, D^0 meson v_2 follows that of other light mesons indicating significant charm quark flow at RHIC [19] [22]. Panel (b) shows v_2/n_q as a function of scaled transverse kinetic energy, $(m_T - m_0)/n_q$, where n_q is the number of constituent quarks in the hadron, m_0 its mass and $m_T = \sqrt{p_T^2 + m_0^2}$.

We see that the D^0 v_2 falls onto the same universal trend as all other light hadrons, in particular for $(m_T - m_0)/n_q < 1\,GeV/c^2$. This suggests that charm quarks have qained significant flow through interactions with the QGP medium in $10-40\%$ $Au+Au$ collision at $\sqrt{s_{NN}} = 200\,GeV$, for more details see [25].

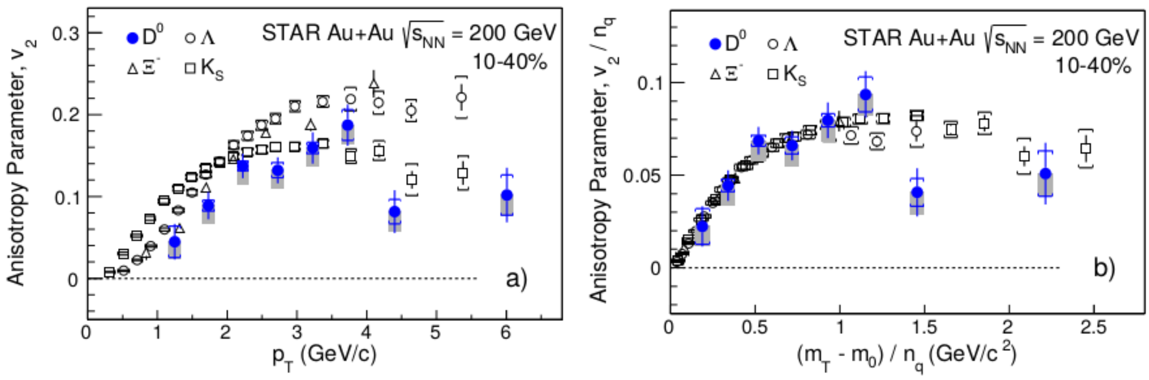

Figure 3.12: Figure (a): v_2 as a function of p_T. Figure (b): v_2/n_q as a function of $(m_T - m_0)/n_q$ for D^0 meson that is compared with K_s^0, Λ and Ξ^-. Taken from [25]

Chapter 4

STAR experiment

The Solenoid Tracker At the RHIC (STAR) is a detector designed to investigate the behavior of strongly interacting matter at high energy density and to search for signatures of quark-gluon plasma (QGP) formation. This experiment is part of the Relativistic Heavy Ion Collider (RHIC) in Brookhaven National Laboratory (BNL).

4.1 Relativistic heavy ion collider

BNL is a multipurpose research institution that is located on the center of Long Island in state New York, (Fig.4.1), with an area of about 5000 acres. One of many goals of BNL is a research in nuclear and particle physics to gain a deeper understanding of matter, energy, space and time. This type of research is enabled by RHIC.

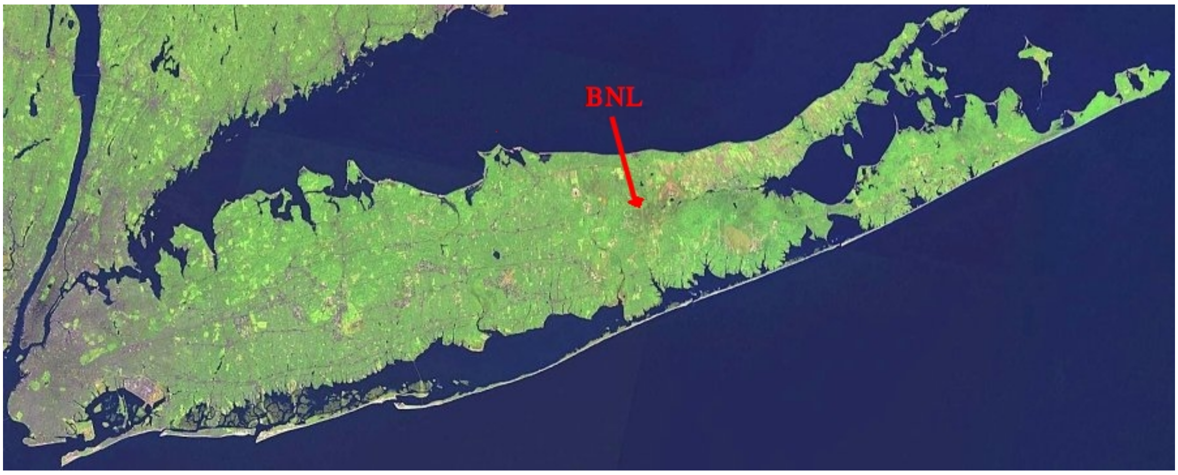

Figure 4.1: A satellite image of the position of BNL on the Long Island (USA). Taken from [11].

In present, RHIC is the second highest energy heavy-ion collider and the only machine capable of colliding beams of polarized protons. It consists of two, hexagonally shaped and 3834 m long circular independent rings in which can be accelerated various ions such as protons or gold nuclei in opposite direction. In this rings, stored particles are guided and focused by superconducting magnets. There are six interaction points where the two rings cross, allowing the particles to collide. Simple schematic drawing of the RHIC is shown in (Fig.4.2).

The types of particle combinations explored at RHIC to this day are $p+p$, $p+Al$, $p+Au$, $d+Au$, $h+Au$, $Cu+Cu$, $Cu+Au$, $Au+Au$, and $U+U$. For $Au+Au$ collisions, the range of center of mass energy is $7.7-200\,GeV$ per nucleon-pair. The speed of the projectiles is typically 99.995% of the speed of light. The designed luminosity is $2\times10^{26}\,cm^{-2}s^{-1}$ for gold ions and $1.4\times10^{31}\,cm^{-2}s^{-1}$ for protons, however current luminosity for gold ions is $87\times10^{26}\,cm^{-2}s^{-1}$ thanks to stochastic cooling upgrade.

Before particles reach the RHIC storage rings they have to pass through several stages of boosters. For protons whole process start in linear accelerator (LINAC), where protons obtain energy of $200\,MeV$. Subsequently, they are sent through the Booster into the Alternating Gradient Synchrotron (AGS) where they obtain more energy. When they have sufficient amount of energy, they are injected into the RHIC storage ring over the AGS-to-RHIC transfer line (AtR). For ions the scenario is a little bit different. The heavy-nuclei are first of all partially stripped of their electrons and then injected into Booster by the Electron Beam Ion Source (EBIS). In Booster, particles are more accelerated and stripped of another electrons, then they are injected into the AGS. Here in AGS, ions are stripped of all electrons and also accelerated to sufficient energy in order to be injected into the RHIC storage rings through AtR.

In present, only the STAR detector is running but in the past, there were also PHENIX, BRAMS, PHOBOS detectors but they completed their programmes in 2015, 2006 and 2005 respectively.

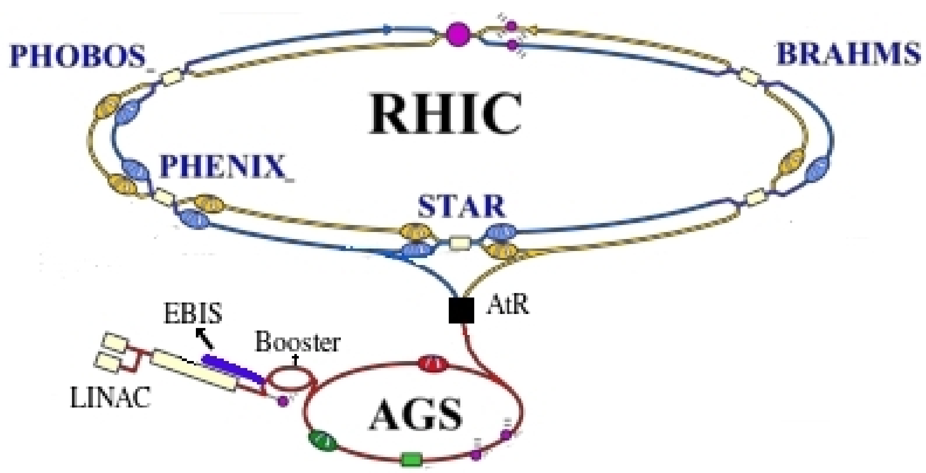

Figure 4.2: A schematic drawing of the RHIC accelerator complex. Taken from [13].

4.2 STAR detector

The STAR detector is a flexible detection system that can simultaneously measure many experimental observables. It was constructed to study the behavior of strongly interacting matter at high energy density and to search for signatures of QGP formation. Measurements of the momentum of particles are made at mid-rapidity over a pseudo-rapidity range $(-1 < \eta < 1)$ with full azimuthal coverage $(0 < \Phi < 2\pi)$.

The most important detectors and systems of the STAR experiment are the Time Projection Chamber (TPC), Barel Electromagnetic Calorimeter (BEMC), Time Of Flight (TOF), Heavy Flavor Tracker (HFT), solenoid magnet, electronics, data acquisition, and trigger system. The detection system consists of TPC and HFT inside a solenoid magnet to enable tracking, momentum analysis, particle identification via dE/dx and location of primary and secondary vertices. HFT detector was installed in 2014. It is the innermost detector of the system which consists of three detectors. The outermost part of HFT is a doubled-sided silicon strip detector (SSD), the intermediate silicon tracker (IST) is a silicon pad detector and the innermost detector is the pixel detector (PXL) which is composed of MAPS technology [3]. For extension of the tracking to the forward region, a radial-drift TPC (FTPC) was installed covering $(2.5 <| \eta |< 4)$ also with complete azimuthal coverage and symmetry. STAR magnet has an outer radius of 3.66 m and a length of 6.85 m and is capable to produce a uniform magnetic field of $0.25 - 0.5\,T$ along the beam axis [4].

There are also another forward detectors, such as the Beam-Beam Counter (BBC) and the Endcap Electromagnetic Calorimeter (EEMC). Around the STAR magnet is located the Moun Telescope Detector (MTD) which covers 45 % of azimuthal angle in range $(-0.5 < \eta < 0.5)$. The MTD, Vertex Position Detector (VPD) and the Zero Degree Calorimeter (ZDC) are located outside of the magnetic field. In the (Fig.4.3) one can see the sketch of the position of some detectors in the STAR experiment.

For our analysis the most important detectors of the STAR experiment are TPC and TOF. The trigger system used for event selection was based on the VPD, ZDC, BBC. Following subsections will describe these facilities.

4.2.1 TPC detector

TPC is a part of the STAR detector which records the tracks of particles, measures their momenta and identifies the particles by measuring their ionization energy loss. Its pseudo-rapidity range covers $(-1.8 < \eta < 1.8)$ with full azimuthal coverage $(0 < \Phi < 2\pi)$ and over the full range of multiplicities. Particles are identified over a momentum range from $100\,MeV/c$ to greater than $1\,GeV/c$ and momenta are measured over a range of $100\,MeV/c$ to $30\,GeV/c$ [62].

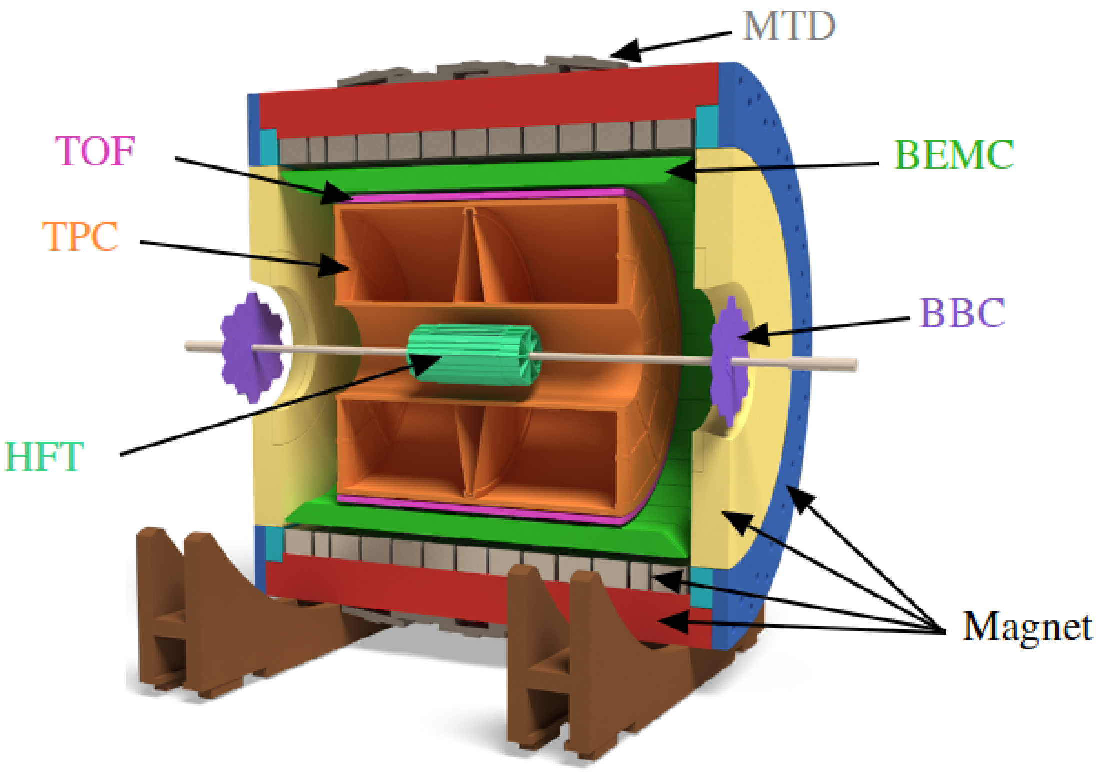

Figure 4.3: The sketch of the STAR detector system. Taken from [12]

The TPC is situated in a large solenoid magnet that operates at $0.5\,T$. It surrounds the beam-beam interaction region and its drift volume is limited by 2 concentric field cage cylinders, of radii $50\,cm$ and $200\,cm$ with the length $4.2\,m$. The STAR TPC is shown schematically in (Fig.4.4). The paths of primary ionizing particles, passing through the gas volume, are reconstructed with high precision from the released secondary electrons which drift to the readout end-caps at the ends of the chamber. The uniform electric field which is required to drift the electrons is defined by a thin conductive Central Membrane (CM) at the center of the TPC, concentric field-cage cylinders and the readout end caps.

The TPC is filled with P10 gas (10% methane, 90% argon) regulated at $2\,mbar$ above atmospheric pressure and the gas circulates with rate of $36,000\,l/h$ (full volume of the TPC is $50,000\,l$). The main property of this gas is a fast drift velocity which peaks at a low electric field. There is a central membrane held at $28\,kV$ that, together with the equipotential rings along the inner and outer field cage, create a uniform drift field of $135\,V/cm$ from the central membrane to the ground end-caps where the readout chambers are located.

The readout system is based on Multi-Wire Proportional Chambers (MWPC) and consists of 12 sectors. Each sector is divided into the inner and outer subsector with 13 and 32 pad rows, respectively. While the outer subsection has complete pad coverage

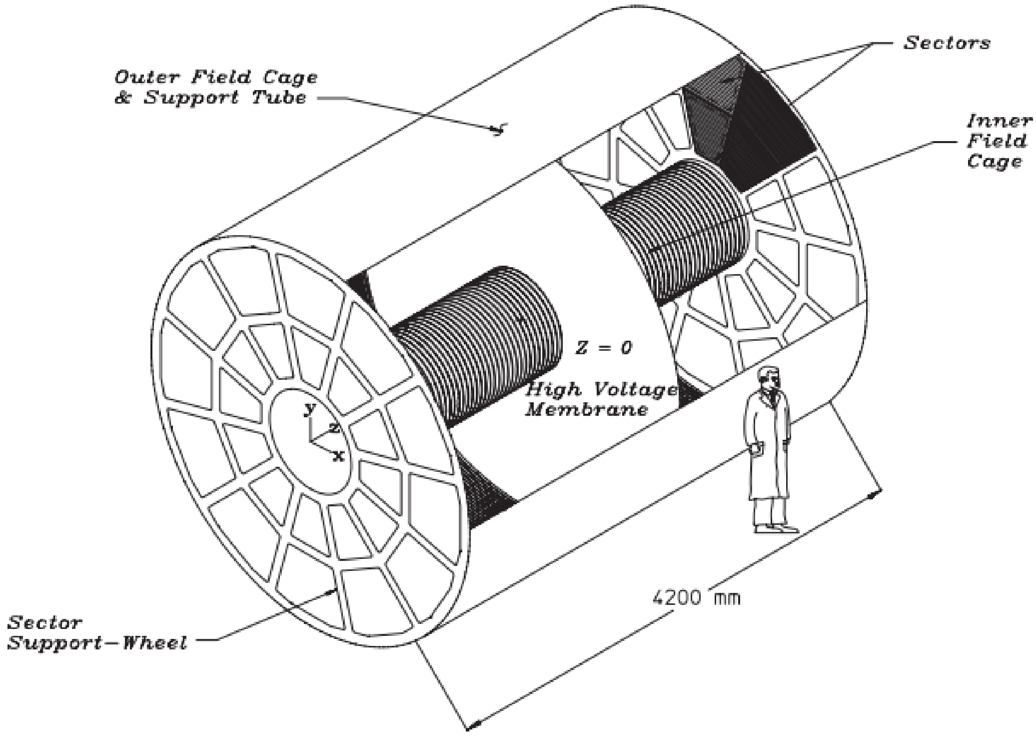

Figure 4.4: STAR TPC overview. Taken from [62]

for better dE/dx resolution and contains in total of 3942 pads with dimensions $6.2 \times 19.5\,mm$, the inner subsection is designed for precise tracking and consists of 1750 pads with size of $2.85 \times 11.50\,mm$. The inner subsection has small pads arranged in widely spaced rows, since each pad in row 1 through 8 and in row 8 through 13, respectively is separated by the $48\,mm$ and $52\,mm$ space. The detailed schema can be found in (Fig.4.5).

The ionization electrons drift towards the end-caps at a constant velocity of $\sim 5.45 cm/\mu s$ and hence maximum drift time in the TPC is $\sim 40\mu s$, that is limit of read-out. The drifting electrons avalanche in the high fields at the $20\,\mu m$ anode wires providing an amplification of 1000 to 3000. The induced charges from the avalanche are then collected by the several read-out pads.

Performance of the TPC

The track of an infinite-momentum particle passing through the TPC at mid-rapidity is sampled by 45 pad rows, but a finite momentum track may not cross all 45 rows. It depends on the radius of curvature of the track, the track pseudo-rapidity, fiducial cuts near sector boundaries, and other details about the particle's trajectory. While the wire chambers are sensitive to almost 100% of the secondary electrons arriving at the end-cap, the overall tracking efficiency is lower $(80-90\%)$ due to the fiducial cuts,

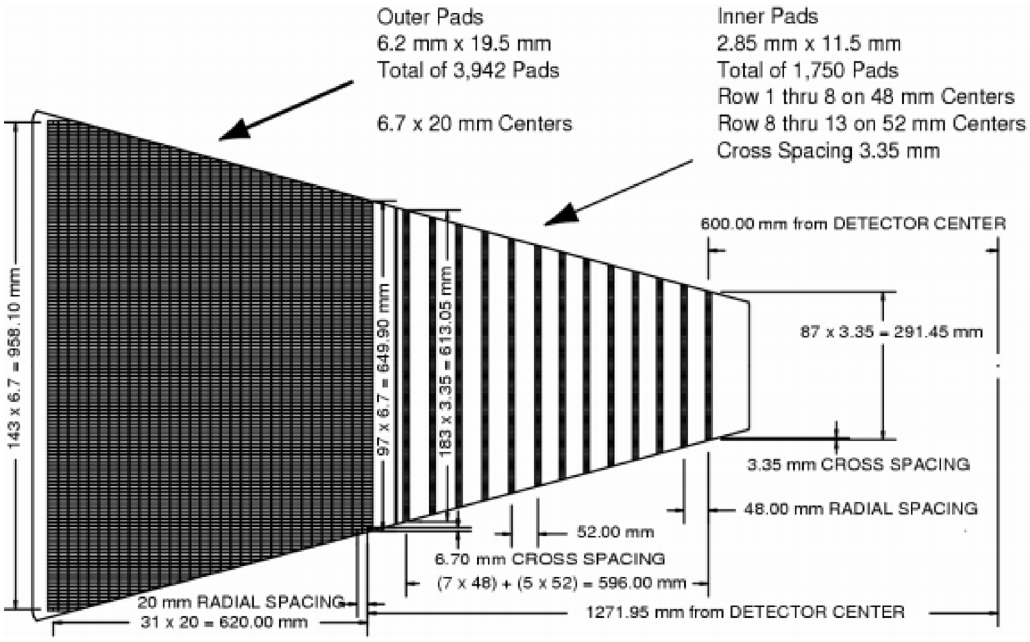

Figure 4.5: The anode pad plane with one full sector shown. The inner sub-sector is on the right and it has small pads arranged in widely spaced rows. The outer sub-sector is on the left and it is densely packed with larger pads. Taken from [62]

track merging, and to lesser extent bad pads and dead channels. There are at most a few percent dead channels in any one run cycle [62].

The track of a primary particle passing through the TPC is reconstructed by finding ionization clusters along the track. The clusters are found separately in x, y and in z space. The local x axis is along the direction of the pad-row, the local y axis extends from beam-line outward through the middle of an perpendicular to the pad-rows, the local z axis lies along the beam axis.

Particle identification by TPC

Energy loss in the TPC gas is a valuable tool for identifying particle species. It works especially well for low momentum particles but as the particle energy rises, the energy loss becomes less mass-dependent and it is hard to separate particles with velocities $v > 0.7c$. STAR is able to separate pions, kaons and protons with a very good accuracy up to $1.2\,GeV/c$. This requires a relative dE/dx resolution of 7% [62].

Energy loss of charged particles by ionization, mentioned above, can be calculated using the Bethe-Bloch formula [38]

$$-\left\langle \frac{dE}{dx} \right\rangle = 2\pi N_A r_e^2 mc^2 \rho \frac{Z}{A}\frac{z^2}{\beta^2}[ln(\frac{2mc^2\beta^2 W_{Max}}{I^2}) - \beta^2 - \frac{\delta^2}{2}] \tag{4.1}$$

where N_A is Avogadro's number, r_e is classical electron radius, m is mass of particle, c is speed of light in vacuum, ρ is density of the material, Z and A are atomic number and weight of material, W_{Max} is maximum energy transfer in a single collision, I is mean excitation energy and δ is density correction.

(Fig.4.6) shows the energy loss for particles in the TPC as a function of the particle momentum. As can be seen, the energy loss for particles is mass ordered which means that heavier particles lose more energy in comparison to the lighter for the same momentum.

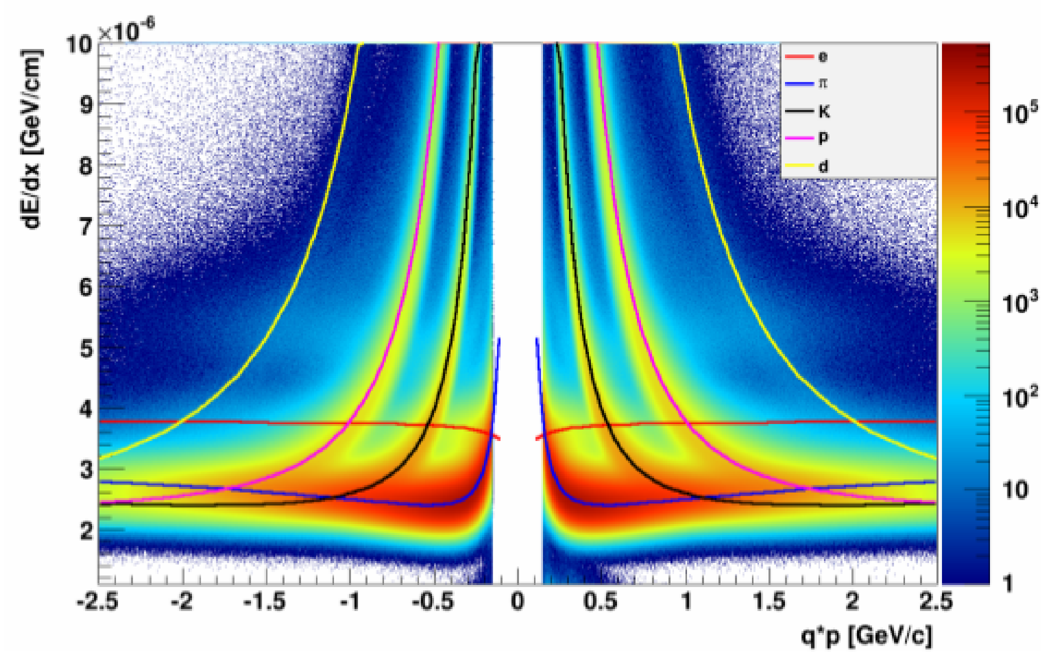

Figure 4.6: The energy loss distribution for particles in the STAR TPC as a function of the momentum of the particle (p) and charge (q). The colored lines represents the expected value for various particle species. Taken from [58]

4.2.2 TOF

In the STAR experiment, the particle identification is done by TPC thanks to its wide and azimuthally complete acceptance about the collision zone. However, it has a problem to identify the charged hadrons such as pions, kaons and protons if their momentum is above $\sim 0.6\,GeV/c$ because energy bands start to mix with each other, see (Fig.4.6). Therefore, the Time Of Flight (TOF) detector, with a total timing resolution of $100\,ps$ in the STAR geometry, was developed to improve the particle identification ability of the STAR experiment for the particles with momenta in range $0.6-3\,GeV/c$. The system was fully installed in 2010. It is based on Multi-gap Resistive Plate Chamber (MRPC) technology. Each tray, with dimension $95 \times 8.5 \times 3.5$ inches, contains 32 MRPC modules and cover 6 degrees in the azimuthal angle and one unit in pseudo-rapidity. In total, TOF detector consists of 120 trays and covers full azimuthal angle at $-1 < \eta < 1$. The TOF sits inside the STAR magnet behind the TPC.

Particle identification by TOF

Based on the information from the TOF relative particle speed β is calculated as

$$\frac{1}{\beta} = \frac{c\tau}{L} \tag{4.2}$$

where c is speed of light, L is the track length from the primary vertex position to the matched TOF channel and τ is the time of flight. From the relativistic particle momentum we obtain (in natural units)

$$p = m\beta\gamma \Rightarrow p^2 = \beta^2(m^2 + p^2) \tag{4.3}$$

where m is particle mass, one can derive the relation between β and p where the only one unknown parameter is the mass of the particle

$$\frac{1}{\beta} = \sqrt{(\frac{m^2}{p^2} + 1)} \tag{4.4}$$

(Fig.4.7) shows behavior of $1/\beta$ as a function of momentum. Solid black lines are predictions from (Eq.4.4) for π, K and p.

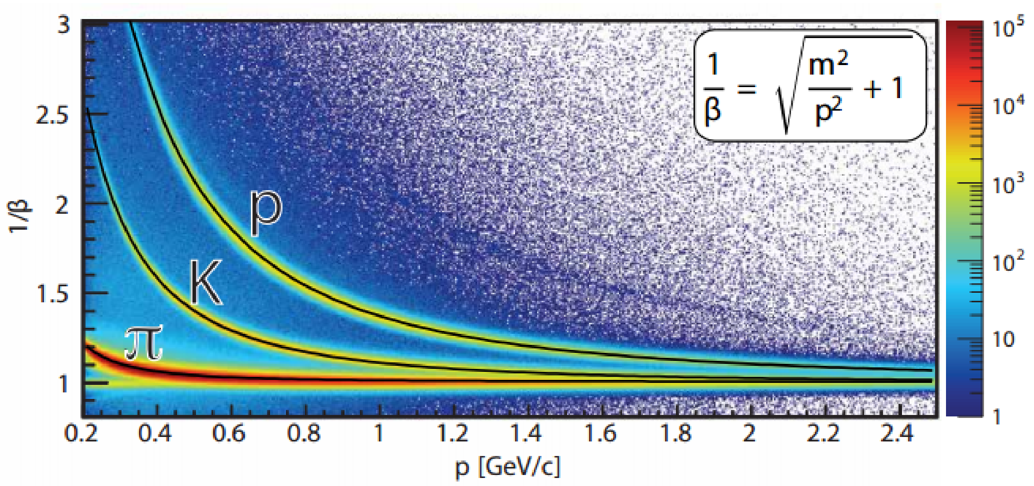

Figure 4.7: Particle Identification by STAR TOF. Taken from [76]

4.2.3 Trigger system

As was mentioned above, the main STAR detectors are relatively slow. However, the trigger system must look at every RHIC crossing and decide whether or not to accept that event and initiate recording the data. This system is a pipelined system which is based on the input from the fast detectors to control the event selection for slower tracker detectors. Trigger detectors is a group of fast detectors that make decision whether or not to accept event. Into this groups of detectors belong Zero-Degree Calorimeter (ZDC), Beam-Beam Counter (BBC), Barrel Electromagnetic Calorimeter (BEMC), Vertex Position Detector (VPD), Endcap Electromagnetic Calorimeter (EEMC) or Forward Pion Detector (FPD). This trigger system is functionally divided into four different layer levels. Interactions that pass selection criteria in these successive trigger levels are sent to storage [39].

Level 0

Level 0 is the fastest and analyzes raw data to determine whether a requested type of interaction occurred in crossing. Data that are used in this level are mostly from the ZDC, BBC and VPD. These detectors are described in next section of this chapter. When the data pass through Level 0 they reach another levels.

Level 1, Level 2

Level 1 and 2 operate in the time period of several milliseconds during which these data are analyzed in more detail in order to determine whether the event meets more finer grained criteria. If it does not, then the digitization process is aborted and the detectors are free for a new trigger.

Level 3

Level 3 makes the final decision. If the data pass through this level so they will be sent to storage. It also includes an on-line display so that individual events can be visually inspected in real time.

ZDC

ZDC detectors are hadron calorimeters that are installed on both the east and west side of STAR detector. Location of these calorimeters in STAR is $18\,m$ away from the interaction point along the beam line, see (Fig.4.8). In front of the ZDC detectors dipole magnets are located. The goal of these magnets is to bend charged particles and leave the neutrons hit the ZDC modules and therefore from these devices one can obtain the number of spectator neutrons, for use as a minimum bias trigger. Subsequently, from these measurements one can calculate the multiplicity that is used to measure the reaction centrality in mutual beam interactions [84]. Each calorimeter is split into 3 modules, and each module consists of tungsten plates, scintillator fibers going to a PMT and ADCs, see (Fig.4.9).

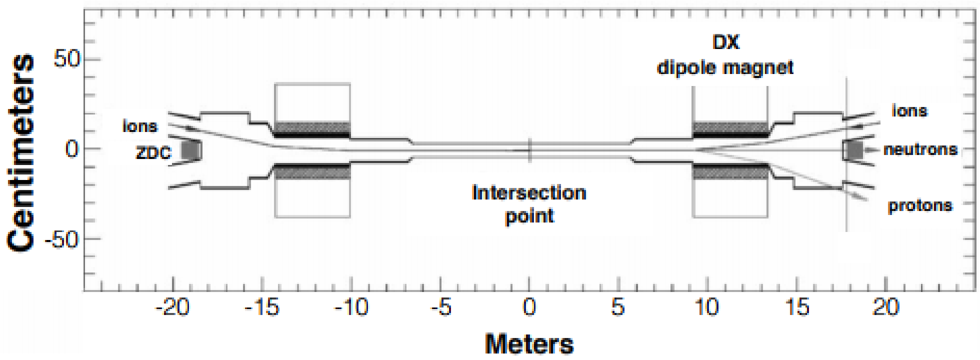

Figure 4.8: Plane view of intersection region, dipole magnets and ZDCs installed. Taken from [84]

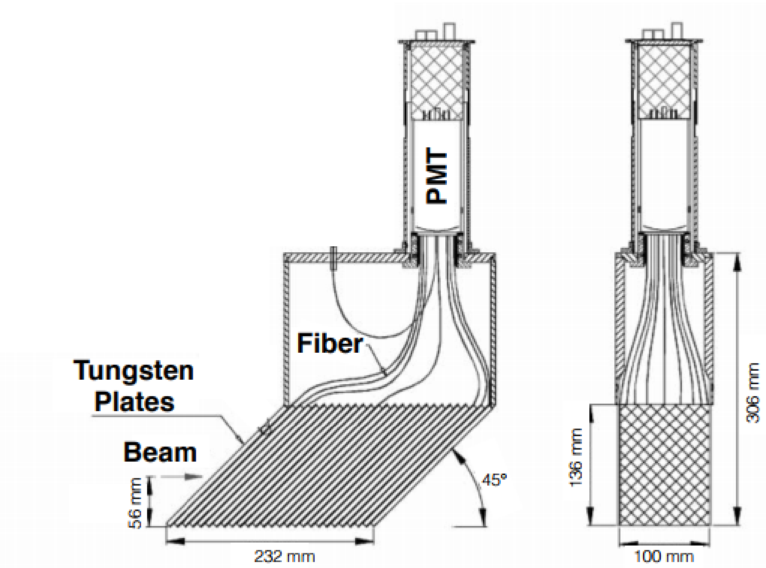

Figure 4.9: ZDC structure. Taken from [84]

VPD

The VPD [60] is situated at a distance of ±5.7 from the center of the STAR detector and consists of two detector that are fully integrated into the STAR trigger system. Each VPD detector uses 19 subdetectors composed of the Pb converter with the fast plastic scintillator followed by the read out photomultiplier, see (Fig.4.10).

The main task of the VPD detectors is a detection of photons from the π^0 decays, which travel very close to the beam pipe, from the primary vertex position at the speed of light. The difference in arrival times are used to determined the $z-$components of the primary vertex position via the equation

$$V_z = \frac{(t_{east} - t_{west})c}{2}, \tag{4.5}$$

where c is the speed of light and t_{west} and t_{east} are the times of the detection of photons in the East and West VPD detectors, respectively.

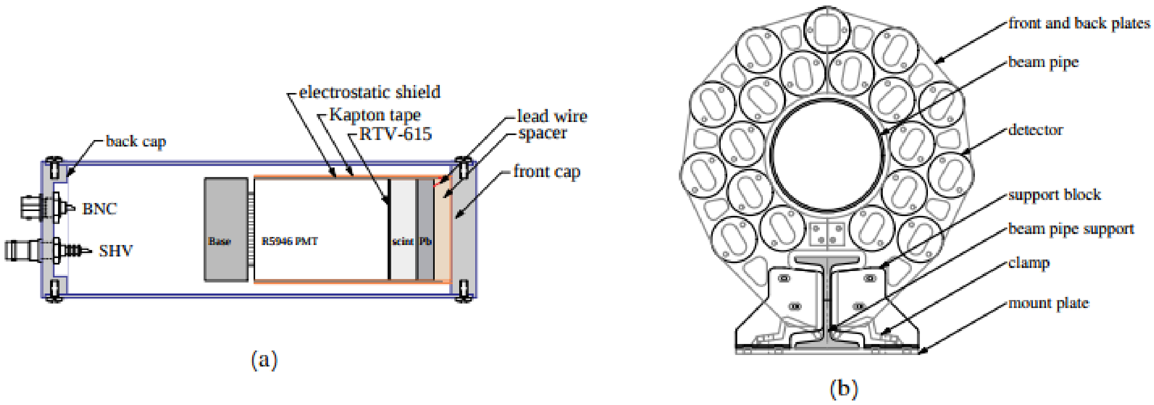

Figure 4.10: On the left figure is a schematic side view of the VPD detector and on the right figure is a schematic front view of the VPD assemble. Taken from [60]

In the particle identification the VPD detectors have a important position because they provide a event start time, t_{start}, for the TOF or MTD detectors. This time can be given via the relation

$$t_{start} = \frac{(t_{east} + t_{west})}{2} - \frac{L}{c}, \tag{4.6}$$

where, L is the distance from either assembly to the center of the STAR detector. Subsequently, the time of flight measured particle is given by

$$\tau = t_{stop} - t_{start}, \tag{4.7}$$

where t_{stop} is measured by TOF or MTD detector. In (Fig.4.11) a real photo of the VPD that is situated around the beam pipe can be seen.

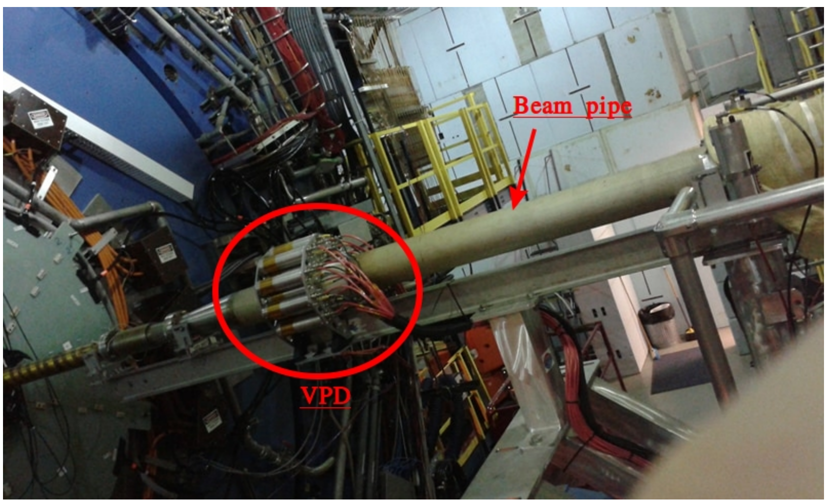

Figure 4.11: Real photo of the VPD detector.

BBC

This detector is a set of scintillators that are installed around the beam pipe on the east and west outer side of the STAR magnet. These BBC detectors are $3.75\,m$ from the interaction point, see (Fig.4.12). Each detector consists of two rings of large and small hexagonal scintillator tiles. An outer ring consists of large tiles and an inner ring consists small tiles. However, each ring can be divided into two sub-rings where the inner sub-ring has six tiles while the outer sub-ring has twelve tiles. These hexagonal scintillator tiles are $1\,cm$ thick, for a clear image, see (Fig.4.13). Signal from the scintillators are transmitted by four optical fibers, that are embedded in each tile, to an individual photomultiplier. The timing difference between the two counters will locate the primary vertex position [80]. The trigger system also contains EEMC, BEMC detectors however they are not too important for our analysis so we will not describe them. For some information about them see [17].

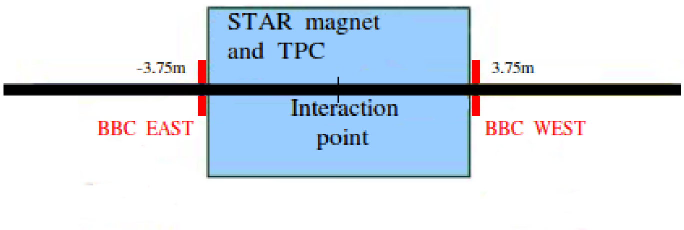

Figure 4.12: Schematic side view of BBC positions.

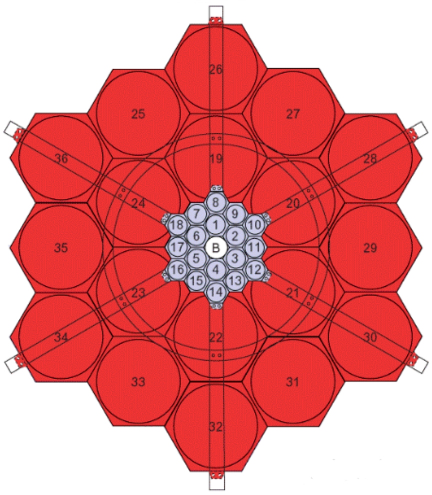

Figure 4.13: STAR BBC schematic front view. Taken from [17].

Chapter 5

Femtoscopy

In this chapter we will describe the basic concept of two particle correlation femtoscopy, also known as Hambury-Brown and Twiss (HBT) interferometry, that is based on quantum interferometry of two identical particles. In the first section we will mention the brief history, where we will write about the first use of this method in radio-astronomy and subsequently about its application in the particle physics. Then, in the second and third section a theoretical background of identical and non-identical femtoscopy will be presented, respectively. In the last section of this chapter we will simply describe non-femtoscopy correlation effects which are significant for low-multiplicity systems and results from the other experiments.

5.1 Brief history of femtoscopy

In 1956 Robert Hambury-Brown and Richard Q. Twiss introduced a novel method based on photon intensity interferometry, which was an alternative way to Michelson interferometry how to measure sizes of the stellar objects from the surface of the Earth.

In their experiment two photo-detectors are placed in the far field zone of a chaotic radiation source and a correlation between the signals from the two detectors is measured. Hambury and Twiss found that photons emitted by thermal source are not independent and that they tended to arrive in pairs at the two detectors, as a consequence of Bose-Einstein statistics. This effect is pure quantum-mechanical phenomenon and can not be described by classical physics.

Photo-detectors in their experiment consist of two paraboloidal telescopes that are used in radio-astronomy. Inner part of the telescopes was covered by mirrors with diameter of $156\,cm$. These mirrors focused light from the star into the cathode of the photomultipliers. The output signals from both photomultipliers were processed and afterwards the correlation function between the intensity of the photons, which were received by the mirrors, could be obtained. Photo-detectors and scheme of the

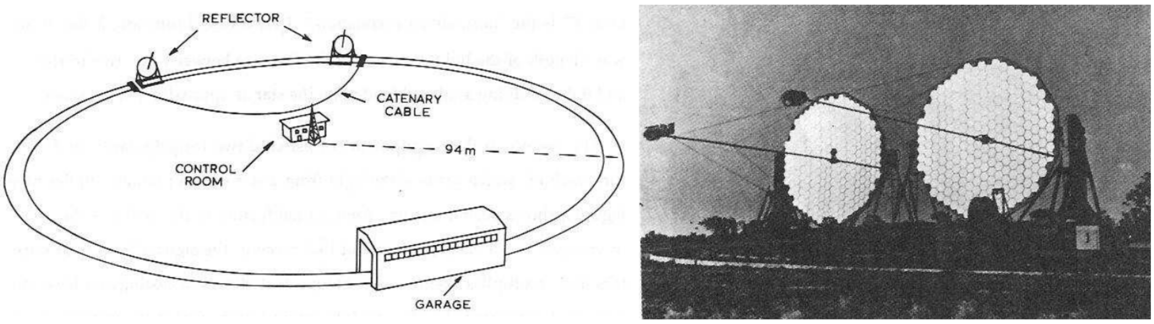

(a) (b)

Figure 5.1: Left figure: A scheme of the Hambury-Brown and Twiss experiment is depicted. Right figure: Two paraboloidal telescopes which are covered by mirrors

experiment are shown in (Fig.5.1).

In particle physics, an observation of the correlation between two identical particles was a serendipity [1], as for example a discovery of penicillin. This observation was made by Gerson Goldhaber, Sulamith Goldhaber, Wonyong Lee and Abraham Pais in the beginning of 1960s when they performed an experiment aiming at the discovery of the ρ^0 resonance. In their experiment they considered collisions between proton and anti-proton and searched for the the resonance by means of the decay $\rho^0 \to \pi^- \pi^+$, by measuring the unlike pair mass-distribution. However, due to poor statistics they could not establish the existence of the ρ^0. On the other hand, in these collisions they observed an angular correlation between identical pions and using the symmetrized wave function for identical pions they reproduced the angular distribution. They concluded that this effect originated from the quantum statistical effect which is called Bose-Einstein correlation [64]. In 1970s G. I. Kopylov and M.I.Podgoretsky developed the theoretical background and mathematical formalism of two particle correlation. Because of typical space and time extents of order of tens fermi the term **"femtoscopy"** has been used.

5.2 Intensity interferometry of two identical particles

On the following few pages we will derive theoretical shape of the correlation function for two identical particles where we assume that there is no final state interaction between particles and then we will describe its application in heavy ion collisions.

Let us have a certain source which emits two identical particles from different points, x_1^μ and x_2^μ. This source is characterized by the emission function $S(x^\mu, p^\mu)$ which can be identified as a Wigner function which is viewed as the probability that particle with four-momentum p^μ is emitted from the space-time point x^μ in the collision region, so if

[1] Serendipity means an unplanned, fortuitous discovery.

we want to calculate probability that source emits one particle with momentum $\vec{p}$ we have to integrate over the whole source

$$P(\vec{p}) = \int d^4 x_\mu S(x^\mu, p^\mu)|_{p_0=E_p}, \tag{5.1}$$

where emission function is evaluated on-shell i.e. $p_0 = E_p = \sqrt{m^2 + \vec{p}^2}$. These emitted particles are observed by two detectors that are located at $x_1'^\mu$ and $x_2'^\mu$. In (Fig.5.2) we can see that there are two possible routes, shown as solid and dashed lines, how particles can reach detectors. In a case of identical particles there is no way how to distinguish between them in quantum mechanics, therefore we have to symmetrize the wave function for the case of bosons or antisymmetrize for the case of fermions.

$$\Psi_{12}(x_1, x_2) = \frac{1}{\sqrt{2}}[\Psi_1(x_1)\Psi_2(x_2) \pm \Psi_1(x_2)\Psi_2(x_1)],$$
$$\Psi_{12}(x_1, x_2) = \frac{1}{\sqrt{2}}[A_1 A_2 e^{-ip_1^\mu ({x_1}' - x_1)_\mu} e^{-ip_2^\nu ({x_2}' - x_2)_\nu} \pm A_1 A_2 e^{-ip_1^\mu ({x_1}' - x_2)_\mu} e^{-ip_2^\nu ({x_2}' - x_1)_\nu}], \tag{5.2}$$

where $\Psi_i(x_i)$ is a wave function for a single particle emitted from point x_i^μ with a momentum p_i^μ and A_i is an amplitude. The signs ($\pm$) correspond to symmetrized Bose-Einstein or anti-symmetrized Fermi-Dirac statistics. The positive sign is for symmetrized function (bosons) while the negative sign is for anti-symmetrized function (fermions).

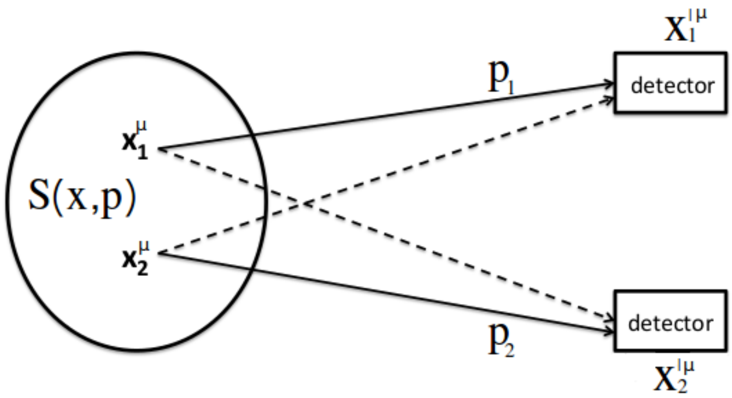

Figure 5.2: Diagram of quantum interference between two identical particles.

Then the probability density is written as

$$|\Psi_{12}(x_1, x_2)|^2 = \frac{1}{2}|A_1|^2|A_2|^2[2 \pm (e^{i(x_1-x_2)^\mu (p_1-p_2)_\mu} + e^{-i(x_1-x_2)^\nu (p_1-p_2)_\nu})]. \tag{5.3}$$

Using Euler's formula for cosine we get

$$|\Psi_{12}(x_1, x_2)|^2 = |A_1|^2 \, |A_2|^2 \, [1 \pm cos((p_1 - p_2)^\mu (x_1 - x_2)_\mu)] \tag{5.4}$$

where the second term in (Eg. 5.4) represents the strength of the correlation in HBT effect. Therefore the correlation becomes strong when the relative difference $(x_1-x_2)^\mu$ or relative momentum $(p_1-p_2)^\mu$ are small. On the other hand, there is almost no correlation for large values of $(p_1-p_2)^\mu$ and $(x_1-x_2)^\mu$.

Now, it is helpful to define the correlation function C_F as

$$C_F(\vec{p_1},\vec{p_2}) = \frac{P(\vec{p_1},\vec{p_2})}{P(\vec{p_1})P(\vec{p_2})}, \tag{5.5}$$

where $P(\vec{p_1},\vec{p_2})$ is the probability of measuring two particles with momenta $\vec{p_1}$ and $\vec{p_2}$ that are emitted from the same source and $P(\vec{p_i})$ is the probability of measuring of a single particle with momentum $\vec{p_i}$. The probability $P(\vec{p_1},\vec{p_2})$ is defined as

$$P(\vec{p_1},\vec{p_2}) = \int d^4x_{1\mu}d^4x_{2\nu}S(x_1^\mu,p_1^\mu)S(x_2^\nu,p_2^\nu)\left|\Psi_{12}(x_1,x_2)\right|^2. \tag{5.6}$$

Using (Eq. 5.4) in (Eq. 5.6) we obtain

$$P(\vec{p_1},\vec{p_2}) = P(\vec{p_1})P(\vec{p_2}) \pm \int d^4x_{1\mu}d^4x_{2\nu}S(x_1^\mu,p_1^\mu)S(x_2^\nu,p_2^\nu)cos((p_1-p_2)^\sigma(x_1-x_2)_\sigma), \tag{5.7}$$

where we have neglected amplitudes A_1 and A_2 because in the final result they will not contribute to the correlation function.

In this point, it is good to define relative and average four-momentum and space-time coordinates as

$$q^\mu = (p_1-p_2)^\mu \qquad k^\mu = \frac{1}{2}(p_1+p_2)^\mu, \tag{5.8}$$

$$x^\mu = (x_1-x_2)^\mu \qquad X^\mu = \frac{1}{2}(x_1+x_2)^\mu. \tag{5.9}$$

If we assume that the emission function has a smooth momentum dependence we can write

$$S(x_1^\mu,p_1^\mu)S(x_2^\nu,p_2^\nu) = S(X^\mu+\frac{x^\mu}{2},k^\mu+\frac{q^\mu}{2})S(X^\nu-\frac{x^\nu}{2},k^\nu-\frac{q^\nu}{2}) \approx S(X^\mu+\frac{x^\mu}{2},k^\mu)S(X^\nu-\frac{x^\nu}{2},k^\nu) \tag{5.10}$$

Neglecting of the relative momentum is valid only for sufficiently small relative momenta. This approximation in particle physics is denoted as **smoothness approximation**.

Using the mentioned smoothness approximation, relative and average variables we can rewrite (Eq. 5.7) as

$$P(\vec{p_1},\vec{p_2}) = P(\vec{p_1})P(\vec{p_2}) \pm \int d^4x_\mu\, cos(x^\sigma q_\sigma) \int d^4X_\nu\, S(X^\mu+\frac{x^\mu}{2},k^\mu)S(X^\nu-\frac{x^\nu}{2},k^\nu), \tag{5.11}$$

where the term $\int d^4X_\nu\, S(X^\mu+\frac{x^\mu}{2},k^\mu)S(X^\nu-\frac{x^\nu}{2},k^\nu) = D(x^\mu,k^\mu)$ is called the **relative distance distribution** which gives us information about the source.

Then, the two-particle correlation function (Eq. 5.5) can be written as

$$C_F(\vec{q},\vec{k}) = 1 \pm \frac{\int cos(x^\sigma q_\sigma) D(x^\mu, k^\mu) d^4x_\mu}{\int d^4x_\mu d^4X_\nu S(X^\mu + \frac{x^\mu}{2}, k^\mu) S(X^\nu - \frac{x^\nu}{2}, k^\nu)} = 1 \pm \frac{\int cos(x^\sigma q_\sigma) D(x^\mu, k^\mu) d^4x_\mu}{\int D(x^\mu, k^\mu) d^4x_\mu} \tag{5.12}$$

where term $\frac{D(x^\mu,k^\mu)}{\int D(x^\mu,k^\mu)d^4x_\mu} = d(x^\mu, k^\mu)$ is a **normalized relative distance distribution**. Using term $d(x^\mu, k^\mu)$ in (Eq. 5.12) we obtain

$$C_F(\vec{q},\vec{k}) = 1 \pm \int cos(x^\sigma q_\sigma) d(x^\mu, k^\mu) d^4x_\mu. \tag{5.13}$$

The equation (Eq.5.13) suggest that there is a one to one relation between the emission and correlation function, in which the correlation function is 4-dimensional Fourier transform of the emission function. However, to get information about emission function from correlation function is quite a difficult issue, because the measured particles are on-shell, $p^0_{1,2} = E_{1,2} = \sqrt{(m^2_{1,2} + \vec{p}^2_{1,2})}$, while the four-momenta q^μ and k^μ are off-shell and satisfy the relation

$$k^\mu q_\mu = \frac{1}{2}(m_1^2 - m_2^2). \tag{5.14}$$

Therefore, we introduce **on-shell approximation** which is used in many application and has a form

$$k^0 \approx E_k = \sqrt{m^2 + k^2}. \tag{5.15}$$

Using the On-shell approximation and asking for the (Eq. 5.14) to be equal to zero we get that only three of the four relative momentum components are kinematically independent. Hence, the q^μ-dependence of $C(\vec{q},\vec{k})$ allows to test only three of four independent x^μ-directions of the emission function [82].

Using so-called **mass-shell constraint** ($q_\mu k^\mu = 0$), we obtain a condition for the fourth variable of the four-momentum q^μ in the form

$$q^0 = \frac{\vec{k}}{k^0} \cdot \vec{q} = \vec{\beta} \cdot \vec{q}. \tag{5.16}$$

With the mass-shell constraint, equation 5.13 can be written as

$$C(\vec{q},\vec{k}) = 1 \pm \int cos(\vec{q} \cdot \vec{r}) \int d(\vec{r} + \vec{\beta}t, t, k) dt d\vec{r} = 1 \pm \int cos(\vec{q} \cdot \vec{r}) S_{\vec{k}}(\vec{r}) d\vec{r}, \tag{5.17}$$

where function $S_{\vec{k}}(\vec{r})$ is defined as the **relative source function** and $\vec{r} = \vec{x} + \vec{\beta}t$. Appendix A describes how to pass from equation 5.13 to equation 5.17. From the definition of relative source function one can see that this function does not describe whole source but it describes just smaller region of the source from where particles fly out. This region is called homogeneity region and we will discuss it later in this chapter.

In a case when the system is in the rest frame of the particle pair where $\beta = 0$, the relative source function is a simple integral over the time argument of the relative distance distribution $d(\vec{x}, t, k_0, \vec{k})$ [82]. Here the correlation function is Fourier transformation of the relative source function into which the time dependence is convoluted. The deconvolution of the time (t) and space ($\vec{x}$) variables must be done through models that describes four-dimensional particle emission.

So, if we know this relative source function we are able to calculate the correlation function. However, it is the correlation function that is measured and we would like to extract information about the source that is coded in the emission function $S(x^\mu, p^\mu)$. There could be suggestion to invert the equation 5.12 to obtain the emission function but due to the relative distance distribution, that is product of two identical functions, we do not have an access to the phase of the Fourier transform. However, it turns out that many reasonable source distribution, when folded with itself as in $D(x^\mu, k^\mu)$, result in a distribution that is close to Gaussian [78]. Therefore, correlation function can be parametrized by a Gaussian

$$C(\vec{q}, \vec{k}) = 1 \pm e^{-q^\mu q^\nu B_{\mu\nu}}, \tag{5.18}$$

where $B_{\mu\nu}$ carries widths parameters of this Gaussian parametrization. In Appendix B we show that this $B_{\mu\nu} = \langle \tilde{x}_\mu \tilde{x}_\nu \rangle$, where

$$\begin{aligned} \tilde{x}_\mu &= x_\mu - \langle x_\mu \rangle \\ \langle f(x) \rangle &= \frac{\int d^4x_\mu f(x^\mu) S(x^\mu, k^\mu)}{\int d^4x_\mu S(x^\mu, k^\mu)}. \end{aligned} \tag{5.19}$$

So, using $B_{\mu\nu} = \langle \tilde{x}_\mu \tilde{x}_\nu \rangle$ we can write

$$C(\vec{q}, \vec{k}) = 1 \pm e^{-q^\mu q^\nu \langle \tilde{x}_\mu \tilde{x}_\nu \rangle}. \tag{5.20}$$

Later in this chapter we will show what $\langle \tilde{x}_\mu \tilde{x}_\nu \rangle$ corresponds to the second moments of the source distribution.

As the most simple and very good example of emission function is the Gaussian normal distribution because its Fourier transformation can be analytically calculated

$$S(x, p) = \frac{1}{\sqrt{2\pi R^2}} exp(-\frac{x^2}{2R^2}) \tag{5.21}$$

where R is the standard deviation (radius of emission region, not source size). Since the Fourier transform of Gaussian distribution is also Gaussian distribution, the correlation function can be expressed analytically as

$$C(\vec{q}, \vec{k}) = 1 \pm e^{-q^2 R^2(\vec{k})}. \tag{5.22}$$

In (Fig.5.3) one can see a typical plot of the correlation function for the case of bosons or fermions and for two different sizes of the source as a function of the relative momentum q and the standard deviation R. The standard deviation R is referred as **HBT radius**.

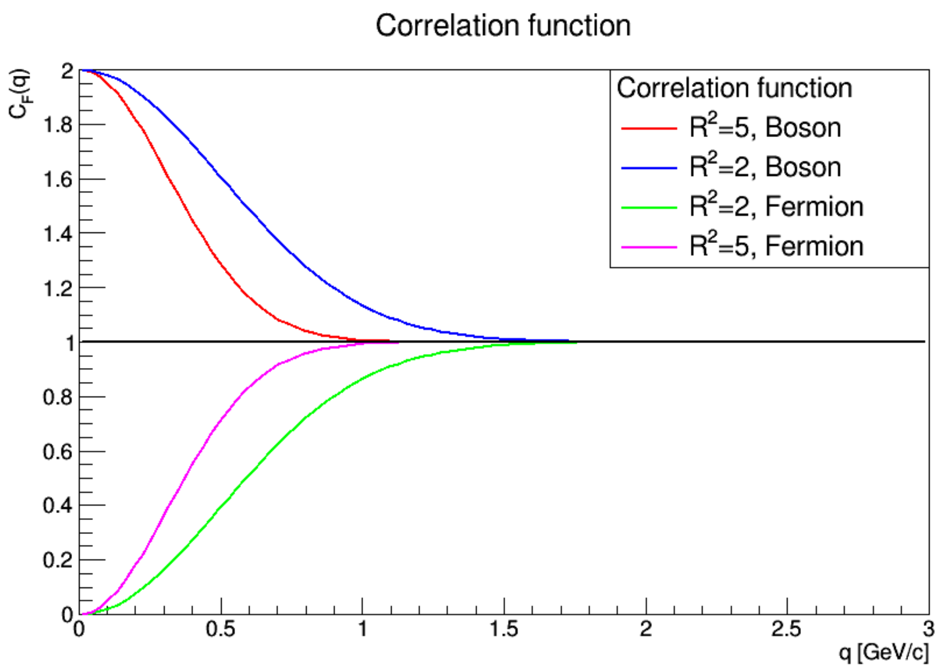

Figure 5.3: Correlation functions that are constructed according to (Eq. 5.22) for two different values of the size of the source and two different type of particles.

For one-dimensional analysis we use correlation function which is written as s function of a Lorentz-invariant relative momentum q_{inv}

$$C(\vec{q}, \vec{k}) = 1 \pm e^{-q_{inv}^2 R_{inv}^2(\vec{k})}, \tag{5.23}$$

where R_{inv} is a one-dimensional source size and q_{inv} is defined as

$$\begin{aligned} q_{inv}^2 &= q_x^2 + q_y^2 + q_z^2 - q_0^2 \\ q_0 &= E_1 - E_2, \end{aligned} \tag{5.24}$$

where q_i is the relative momentum in each direction of the coordinate space and q_0 is the energy difference between two particles, for which the energy is defined as $E = \sqrt{m^2 + p^2}$. This one-dimensional analysis is usually performed in case of limited statistics and all spacial and temporal information are convoluted into $R_{inv}(\vec{k})$.

5.2.1 Bertsch-Pratt parametrization

For extraction of spatial information about the particle emitting source, the standard Cartesian coordinate system is not the best choice. The most common coordinate system for femtoscopic measurements is the so-called Bertsch-Pratt coordinate system often known as the **out-side-long system** that is connected to the pair momentum k^{μ}. In this system, the relative momentum is decomposed into sideward (q_{side}), outward (q_{out}) and longitudinal (q_{long}) direction.

The longitudinal direction is parallel to the beam direction which is typically in z-direction, outward direction is parallel to the pair transverse momentum $\vec{k}_T = (\vec{p}_{T1} + \vec{p}_{T2})/2$ and sideward direction is perpendicular to both longitudinal and outward directions. Such a decomposition can be seen in (Fig.5.4). The Bertsch-Pratt coordinate system is hence unique for each pair of particles.

Each vector $\vec{V}$ can be decomposed into the Bertsch-Pratt coordinate system as follow

$$\begin{aligned} V_{long} &= V_z \\ V_{out} &= \frac{(P_x V_x + P_y V_y)}{P_T} \\ V_{side} &= \frac{(P_x V_x - P_y V_y)}{P_T} \end{aligned} \tag{5.25}$$

where $P = (P_0, P_x, P_y, P_z)$ is pair momentum and $P_T^2 = (P_x^2 + P_y^2)$.

The correlation femtoscopy of identical particles is usually constructed in the Longitudinal Center of Mass System (LCMS) of the emitted pair where $p_{z1} + p_{z2} = 0$, the component of pair momentum in long direction vanishes, therefore q_0 can be rewritten as

$$q_0 = E_1 - E_2 = \frac{\vec{p_1} + \vec{p_2}}{E_1 + E_2} \cdot (\vec{p_1} - \vec{p_2}) = \vec{\beta} \cdot \vec{q} \overset{\text{LCMS}}{\approx} \beta_T q_{out}, \tag{5.26}$$

where $\vec{\beta} = (\beta_T, 0, \beta_l)$ and $\vec{q} = (q_{out}, q_{side}, q_{long})$. In LCMS the term $\beta_l = 0$. Thus the LCMS frame can be obtained by the boost from the laboratory frame along the longitudinal axis. Additional boost of the LCMS frame in the out direction provides the Pair Rest Frame (PRF). The correlation of non-identical particles are studied in the PRF. In the PRF, both particles have the same momentum $\vec{k}^* = \vec{k}_1 = -\vec{k}_2$ and hence the relative pair momentum is $q = 2\vec{k}^*$.

In the Bertsch-Pratt parametrization, the most general form of correlation function of two identical particles for a Gaussian source is expressed as

$$C(\vec{q}, \vec{k}) = 1 \pm e^{-q^\mu q^\nu R^2_{\mu\nu}}, \tag{5.27}$$

where μ and ν takes *out*, *side* and *long*. $R^2_{\mu\nu}$ denotes the six HBT radii parameters that can be derive from the equation 5.20. In Appendix C is shown derivation of these radii. After derivation we obtain a general form of the HBT radii

$$R_o^2 = \langle(\tilde{x}_o - \beta_o \tilde{t})^2\rangle \tag{5.28}$$

$$R_s^2 = \langle\tilde{x}_s^2\rangle \tag{5.29}$$

$$R_l^2 = \langle(\tilde{x}_l - \beta_l \tilde{t})^2\rangle \tag{5.30}$$

$$R_{os}^2 = 2\langle(\tilde{x}_o - \beta_o \tilde{t})\tilde{x}_s\rangle \tag{5.31}$$

$$R_{ol}^2 = 2\langle(\tilde{x}_o - \beta_o \tilde{t})(\tilde{x}_l - \beta_l \tilde{t})\rangle \tag{5.32}$$

$$R_{sl}^2 = 2\langle(\tilde{x}_l - \beta_l \tilde{t})\tilde{x}_s\rangle. \tag{5.33}$$

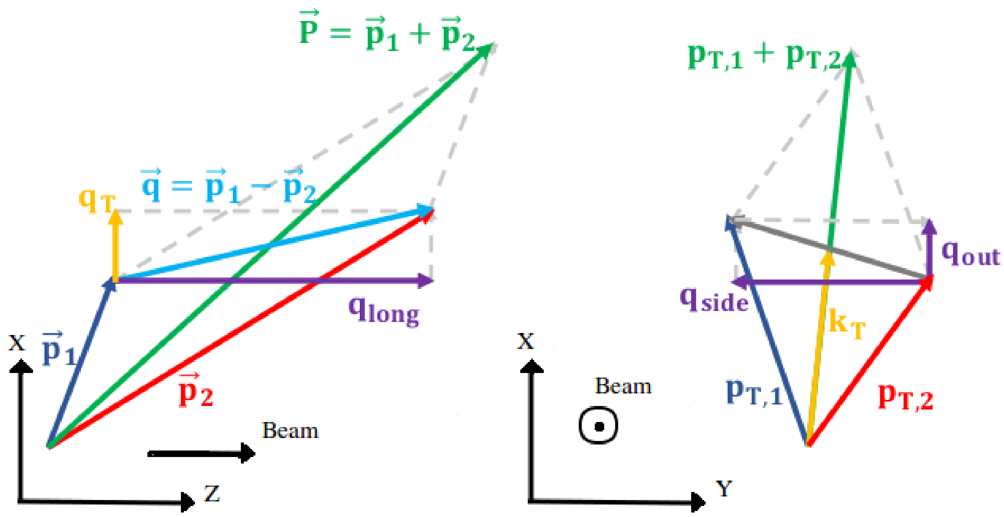

Figure 5.4: The decomposition of $\vec{q}$ in Bertsch-Pratt coordinates.

where $\tilde{x}_\mu = \Delta x_\mu = (x_\mu - \langle x_\mu \rangle)$, β_l, β_o are the components of the pair velocity and $\langle ... \rangle$ denotes an average with the emission function

$$\langle f \rangle (k) = \frac{\int d^4 x_\mu \, f(x^\mu) S(x^\mu, k^\mu)}{\int d^4 x_\mu \, S(x^\mu, k^\mu)} \tag{5.34}$$

For an azimuthally integrated analysis, the emission function has a reflection symmetry $\tilde{y} \to -\tilde{y}$. This symmetry translates to a $q_s \to -q_s$ symmetry of the two-particle correlation function. This means that the cross-terms $R^2_{out,side} = R^2_{side,long} = 0$. If we choose as the reference frame the LCMS frame of the pair, where $\tilde{z} \to -\tilde{z}$, then $R^2_{out,long} = 0$. Afterwards, the correlation function is in the form

$$C(\vec{q}, \vec{k}) = 1 \pm \lambda(\vec{k}) exp(-q^2_{out} R^2_{out}(\vec{k}) - q^2_{side} R^2_{side}(\vec{k}) - q^2_{long} R^2_{long}(\vec{k})), \tag{5.35}$$

where HBT radii measure the spatial and temporal extend of the collision system at the freeze-out.

Here, we also define phenomenologically parameter $\lambda(\vec{k})$ which is related to the degree of source coherence. The value of this parameter is between $0 - 1$. The name of this parameter from historically reason is **chaoticity parameter**. For a fully chaotic source value of this parameter is unity and becomes smaller than unity for a source with partially coherent particles emission. However it does not describe only degree of source coherence, it also accounts for particles misidentification, long-lived resonance decays or long-range tails in the separation distribution.

5.2.2 Final state interaction

During the derivation of the correlation function in the previous subsection we assumed that there is only Bose-Einstein or Fermi-Dirac interference effect and no other final state interaction between the emitted particles. However, most of the HBT measurements in heavy ion collisions are performed with charged particles ($\pi^{\pm}, K^{\pm}, proton..,$) therefore these particles feel long range Coulomb interaction effects on the way from the source to the detector. Moreover, particles can also feel the total electric charge of the source from which they are emitted. Another kind of interaction which plays an important role between outgoing particles is the strong interaction. This interaction is very important in proton-proton correlation. Therefore, if we want to have more correct description of the size of source, from witch the particles are emitted, the interactions must be taken into account. In this analysis only the Coulomb interaction between outgoing particles plays an important role. Another interaction such as Strong interaction or interaction between the source and emitted particles can be neglected for $\pi^{\pm} - \pi^{\pm}$ correlations.

Coulomb interaction

AS mentioned above, in the case of charged particles the Coulomb interaction between particles can not be neglected. This interaction causes a suppression for like-sign particles while for unlike-sign it causes an enhancement of the measured correlation function at low $\vec{q}$.

To calculate the strength of the Coulomb interaction, we consider Schrödinger equation [61] which contains the Coulomb potential

$$\Big[\frac{\hbar^2\nabla^2}{2\mu} + \frac{Z_1 Z_2 e^2}{r}\Big]\Psi_c(\vec{q},\vec{r}) = E\Psi_c(\vec{q},\vec{r}), \tag{5.36}$$

where μ is the reduced mass and r is the relative distance between the two particles, Z_1 and Z_2 are protons numbers of particles, e is the elementary charge and E is the energy in the center of mass frame.

The solutions of the (Eq. 5.36) are written in terms of the confluent hyper-geometric function F as follow

$$\begin{aligned} \Psi_c(\vec{q},\vec{r}) &= \Gamma(1+i\eta_{\pm})e^{-\frac{1}{2}\vec{q}\cdot\vec{r}}F(-i\eta;1,z_{\pm}), \\ z_{\pm} &= \frac{1}{2}qr(1 \pm cos(\theta)). \end{aligned} \tag{5.37}$$

where θ is the angle between $\vec{q}$ and $\vec{r}$, $\eta_{\pm}$ is the Sommerfield parameter which depends on the particle mass and charge as

$$\eta_{\pm} = \pm\frac{me^2}{4\pi q}, \tag{5.38}$$

where minus (plus) sign is for unlike-sign (like-sign) particles. Then the symmetrized Coulomb wave function is

$$\Psi_r(\vec{q},\vec{r})\frac{1}{\sqrt{2}}(\Psi_c(\vec{q},\vec{r}) + \Psi_c(\vec{q},-\vec{r})). \tag{5.39}$$

When we put this wave function to the (Eq. 5.6), then the contribution from the Coulomb interaction to the correlation function can be calculated as

$$P_c(\vec{q},\vec{r}) = \frac{1}{2}\int d\vec{r}d(\vec{r}) \mid \Psi_r(\vec{q},\vec{r}) \mid^2, \tag{5.40}$$

where $d(\vec{r})$ is the distribution of the average distance between the particles in each pair as they are emitted [61] and

$$|\Psi_r(\vec{q},\vec{r})|^2 = A_c(\eta)|F(-i\eta,1,z_\pm)|^2, \tag{5.41}$$

where $A_c(\eta)$ is the Gamov factor and

$$|F(-i\eta,1,z_\pm)|^2 = 1 + 2r^*\frac{1+cos\theta^*}{a_c} + ..., \tag{5.42}$$

where variables with asterix (*) are in the pair rest frame and a_c is Bohr radius. In the (Fig.5.5) we can see how Bose-Einstein, Coulomb and Strong interactions contribute into the proton-proton correlation function.

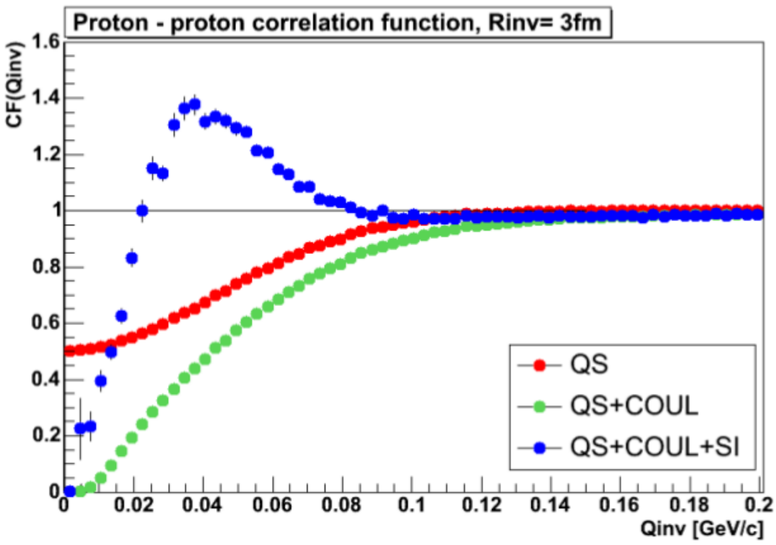

Figure 5.5: Proton-proton correlation functions for the source size of 3 fm with interactions. Taken from [87].

5.3 Femtoscopy and dynamical system

Up until now in our analysis, we have considered a case in which source was static. In this case the size of static source measured by femtoscopy is the same as the whole source size because particles are emitted towards random direction with their thermal momenta from the source thus there is no correlation between the spatial and momentum distributions. However, in case of the heavy-ion collisions, femtoscopy does not measure the whole source size but it measures the so-called **homogeneity region**, which is defined as an area that emits particles with small $\vec{q}$, for illustration see (Fiq.5.6).

The reason that these homogeneity regions do not correspond to the whole size of the source is that in heavy ion-collisions one can watch that lengths of these regions (HBT radii) depend on the quantities such as pair momentum, size of the whole source and reaction plane.

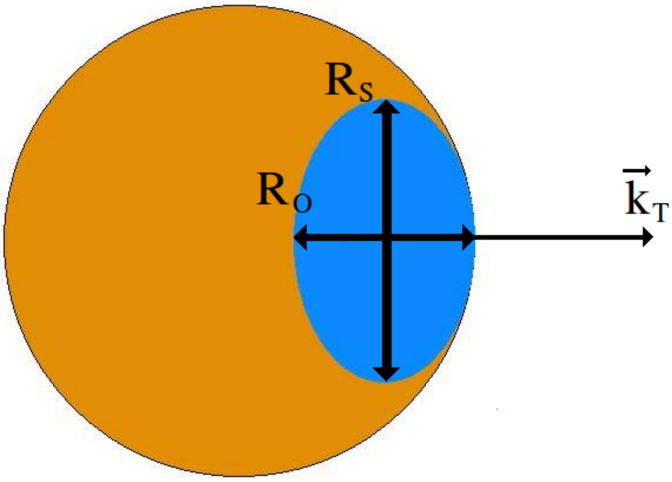

Figure 5.6: Whole source (yellow) with homogeneity region (blue) for pair momentum.

Pair momentum

Here we assume that system is in LCMS frame and that the particles are emitted to radial direction from the center of the source with velocity $\vec{\beta}_T(\vec{r})$. It is also assumed that the transverse velocity of particles is proportional to the distance from the center of the source to their particle positions. Therefore the particles around the surface of the source get larger momentum and thus the emission region measured as the HBT radius would correspond to a smaller region around the surface for higher k_T, and a larger region for lower k_T, see (Fig. 5.7). In the limit of $k_T \to 0$ the HBT radii become closer to the whole size of the source [64]. Within a simple model with a Gaussian source approximation based on the hydrodynamics, the HBT radii can be explicitly extracted as a function of k_T (m_T) as [83]

$$R_s^2(m_T) = \frac{R_{geom}^2}{1 + m_T \eta_f^2 / T}, \tag{5.43}$$

$$R_o^2(m_T) = R_s^2(m_T) + \frac{1}{2}(\frac{T}{m_T})^2 \beta_T^2 \tau_0^2, \tag{5.44}$$

$$R_l^2(m_T) = \tau_0^2 \frac{T}{m_T} \frac{K_2(m_T/T)}{K_1(m_T/T)}, \tag{5.45}$$

where R_{geom} is the actual source size, η_f is the flow rapidity, T is the temperature, β_T is the transverse pair velocity, τ_0 is the freeze-out time and K_n is the n-th modified Bessel function. The presence of the k_T (m_T) dependence of the HBT radii indicates the dynamical expansion of the source.

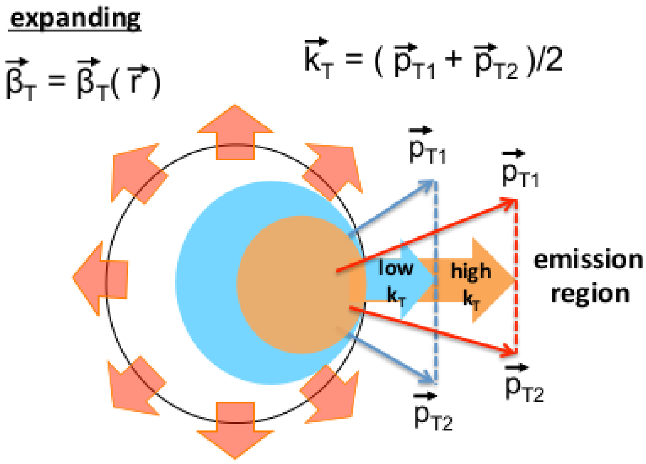

Figure 5.7: Expanding source with two different homogeneity regions. Taken from [64].

Size of the system

In the case of hadron-hadron correlation, one can show that the extracted HBT radii should depend on the quantity which represents the system size, such as centrality or multiplicity.

In the (Fig.5.8) the centrality dependence of pion source parameters are shown as a function of $m_T = \sqrt{m_\pi^2 + k_T^2}$ for six different centralities. We can see that for more central collisions the HBT radii are bigger which is consistent with initial source size because for more central collisions the overlap of two nuclei is greater. Here we can also see that with increasing of m_T the HBT radii are decreasing that is consistent with pair momentum dependence which was mentioned before.

In the (Fig. 5.9) we can see that HBT radii are scale linearly well with the 1/3 power of the number of participants N^{part} calculated by Glauber model. Here the value N_{part} corresponds to the volume of the source and hence $N_{part}^{1/3}$ corresponds to the radius of the system [64].

Reaction plane

In the subsection Flow (2.3.3), we wrote down that for non-central collisions the source shape is expected to be of an elliptical shape, see in (Fig. 2.6). The initial spatial anisotropy creates the momentum anisotropy in the final state which is called elliptic flow and the expansion of the source is preferred into the in-plane direction. In that

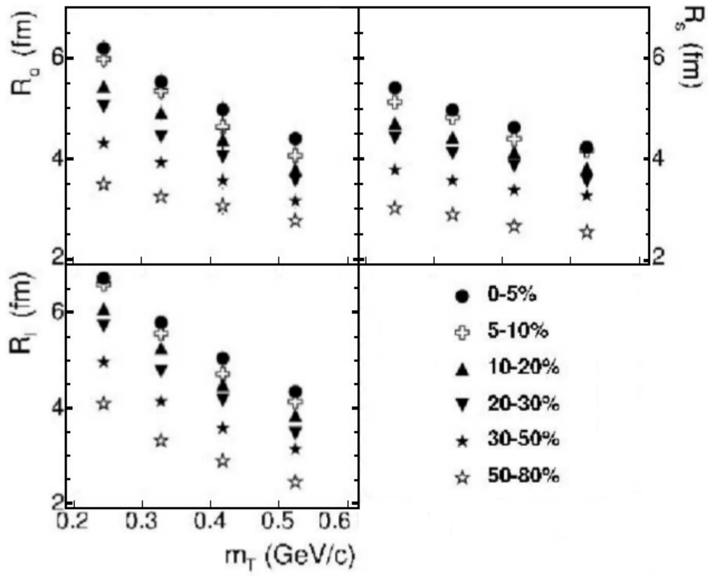

Figure 5.8: HBT parameters vs m_T for different 6 centralities. Data from Au+Au collisions at $\sqrt{s_{NN}} = 200\,Gev$. Taken from [61].

case one can measure the shape of the source at freeze-out by studying oscillation of the HBT radii with respect to the reaction plane. In the (Fig. 5.10) we can see that lengths of the HBT radii R_s and R_o are different with respect to the reaction plane.

In general, the Φ dependence of the HBT radii is described by

$$R^2_\mu(k_T,\Phi) = R^2_{\mu,0}(k_T) + 2\sum_{n=2,4,6...} R^2_{\mu,n}(k_T)cos(n\Phi) \qquad \mu = o,s,l,ol \tag{5.46}$$

$$R^2_\mu(k_T,\Phi) = R^2_{\mu,0}(k_T) + 2\sum_{n=2,4,6...} R^2_{\mu,n}(k_T)sin(n\Phi) \qquad \mu = os \tag{5.47}$$

where $R^2_{\mu,n}$ are the n^{th} order Fourier coefficients for radius term μ. These coefficient can be computed as

$$R^2_{\mu,n}(k_T) = \langle R^2_\mu(k_T,\Phi)cos(n\Phi)\rangle \qquad \mu = o,s,l,ol \tag{5.48}$$

$$R^2_{\mu,n}(k_T) = \langle R^2_\mu(k_T,\Phi)sin(n\Phi)\rangle \qquad \mu = os \tag{5.49}$$

The 0^{th} order Fourier coefficients are expected to be nearly identical to radii extracted in an azimuthally integrated analysis. For more detail you can see [36]. In the (Fig. 5.11) we can see measurements of dependence of squared HBT radii on the reaction plane angle with respect to 2^{th} order for three centrality classes from STAR experiment.

HBT puzzle

For describing the transverse momentum distribution and elliptic flow at low $p_T < 2\,GeV/c$ a relativistic hydrodynamics could be used. Therefore it is natural to expect

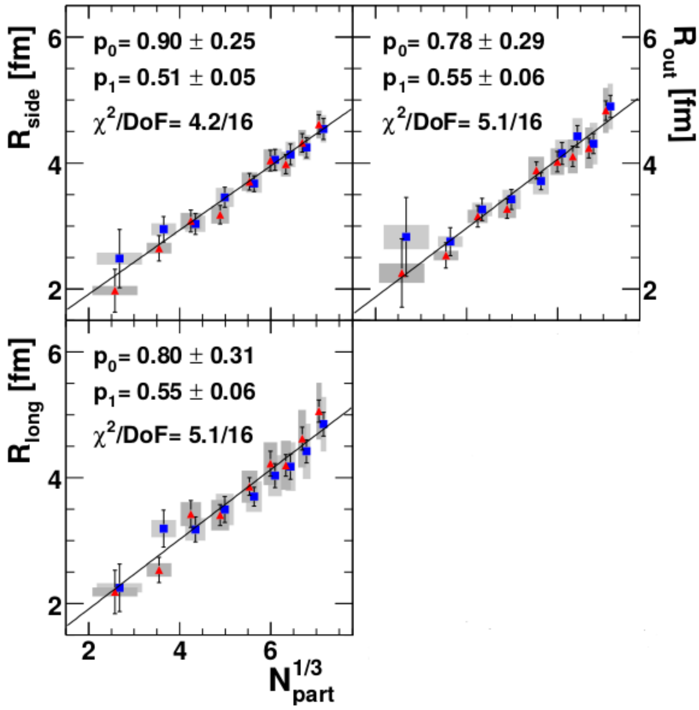

Figure 5.9: The HBT radii for positive (blue square) and negative (red triangle) pairs of identical pions as a function of $N_{part}^{1/3}$ in Au+Au collisions at $\sqrt{s_{NN}} = 200\,GeV$ measured by PHENIX experiment. Taken from [45].

that this hydrodynamical calculation could reproduce the observables of HBT interferometry dominated by two particles with low momentum. In spite of the fact that variety of hydrodynamic models have been calculated, none of them was able to describe the HBT radii from experiments. In the (Fig. 5.12) we can see some models which are inconsistent with the data from Au+Au collisions at $\sqrt{s_{NN}} = 200\,GeV$ measured at RHIC. One of the problems is that according to calculations the ratio R_o/R_s, which is sensitive to the emission duration, should be much larger value than unity but the experimental data shows almost unity. It is clear that models significantly overpredict this ratio. Models also either underestimate or overestimate values of R_o, R_l and R_s. This failure of hydrodynamic models in describing the HBT results from heavy ion collisions has been called the **HBT Puzzle**. This problem was not solved for a decades. However, it was eventually realized [68], [69] that it is an interplay of multiple effects. The hydrodynamic models in order to explain this puzzle need to include such things as the buildup of collective flow in the first instants of the collision before thermalization, use a stiffer equation of state and also include viscosity.

Blast-wave model

As we mentioned above hydrodynamic calculations were not able to describe momentum distribution, elliptic flow and observables of the HBT interferometry at the

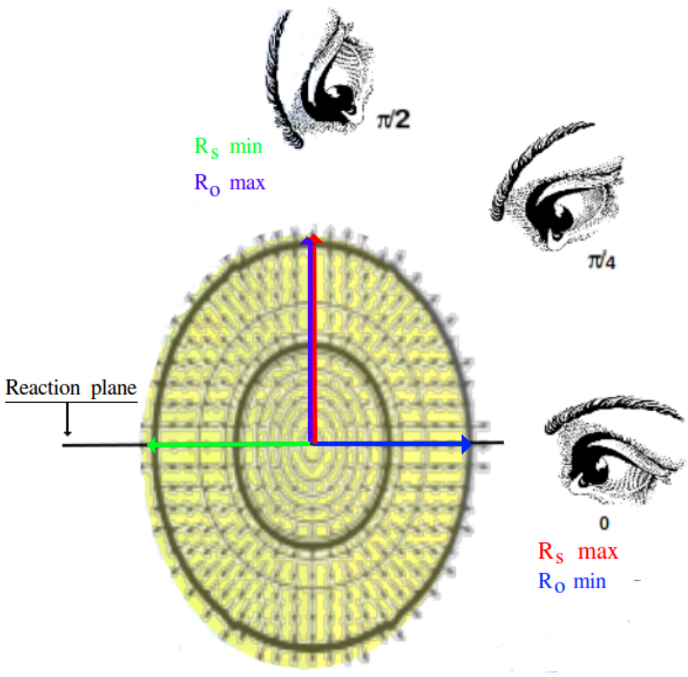

Figure 5.10: A view on the HBT radii from different angle respect to the reaction plane.

same time. One of the many ways how make hydrodynamical effect accessible without time consuming computing is Blast-wave model which is based on the hydrodynamic calculations aiming to describe the system at the freeze-out with a minimal set of parameters.

Here we will use parametrization which was developed in [71]. This parameterization contains eight parameters T, ρ_0, ρ_2, R_y, R_x, a_s, τ_0 and $\Delta\tau$. The physical meaning of these parameters is given below.

The source is parametrized in the Cartesian coordinated system. The reaction plane is the (x-z) plane. In the beam (z) direction the freeze-out distribution is infinite and elliptical in the transverse (x-y) plane where the shape is controlled by the radii R_x and R_y. The spatial weighting of source elements is given by

$$\Omega(r, \phi_s) = \Omega(\tilde{r}) = \frac{1}{1 + e^{(\tilde{r}-1)/a_s}}, \tag{5.50}$$

where ϕ_s is the azimuthal angle of the source element and a fixed value of the normalized elliptical radius

$$\tilde{r}(r, \phi_s) = \sqrt{\frac{(r\, cos(\phi_s))^2}{R_x^2} + \frac{(r\, sin(\phi_s))^2}{R_y^2}}, \tag{5.51}$$

corresponds to a given elliptical sub-shell within the solid volume of the freeze-out distribution. The parameter a_s corresponds to a surface diffuseness of the emission source. When $a_s = 0$, there is a hard edge, while $a_s \approx 0.3$ the profile is a Gaussian shape. This parameter is usually set to 0 for simplicity, see (Fig. 5.13).

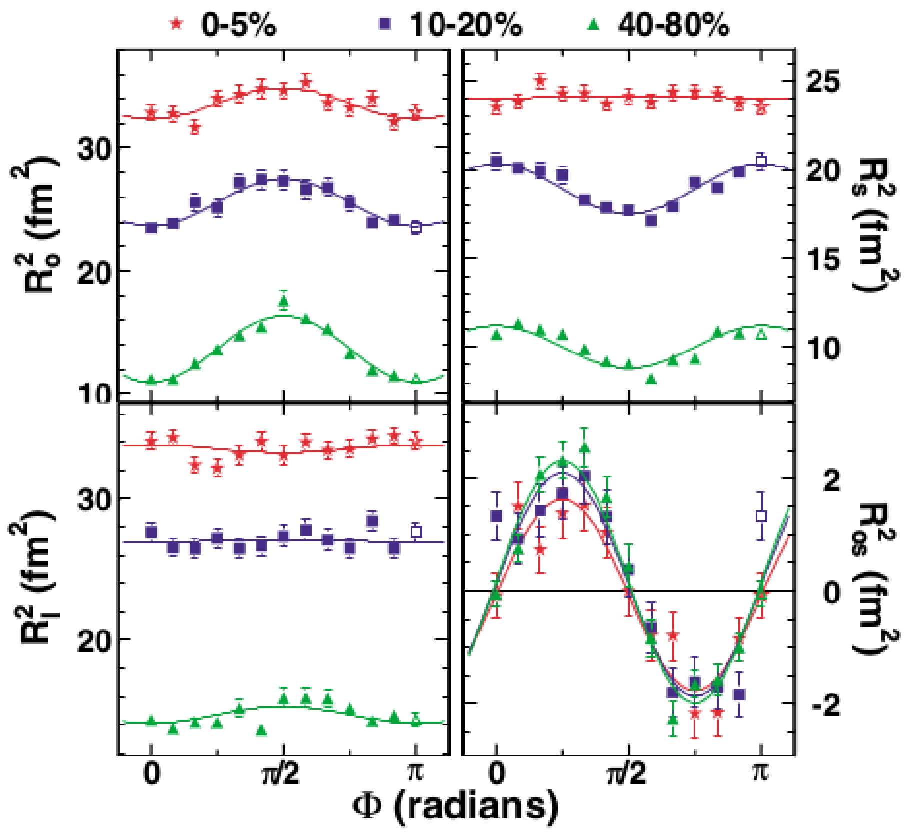

Figure 5.11: Squared HBT radii relative to the reaction plane angle for three different centrality classes from Au+Au collisions at $\sqrt{s_{NN}} = 200\,GeV$. Taken from [28].

A global temperature T is used to describe the spectrum of particles emitted from source element at rest at each point $(x,\ y,\ z)$. This element is also boosted by a transverse rapidity $\rho(x,y)$. This boost is perpendicular to the elliptical sub-shell of the source element profile, see (Fig. 5.14). Thus one can show that

$$\tan(\phi_s) = (\frac{R_y}{R_x})^2 \tan(\phi_b) \tag{5.52}$$

where ϕ_b is the azimuthal angle of the source velocity.

For central collisions the flow rapidity boost strength depends linearly on the normalized elliptical radius $\tilde{r}$. Thus, in absence of an azimuthal dependence of the flow all source elements on the outer edge of the source are boosted with the same transverse rapidity ρ_0 in an outward direction. For non-central collisions, the flow rapidity is given by an additional parameter ρ_2 which characterizes the strength to the second order. Hence the flow rapidity is given as

$$\rho(\tilde{r}, \phi_s) = \tilde{r}(\rho_0 + \rho_2 cos(2\phi_b)). \tag{5.53}$$

The source anisotropy enters into our parametrization in two independent ways and each affects elliptic flow. The first, setting $\rho_2 > 0$ means the boost is stronger in-plane

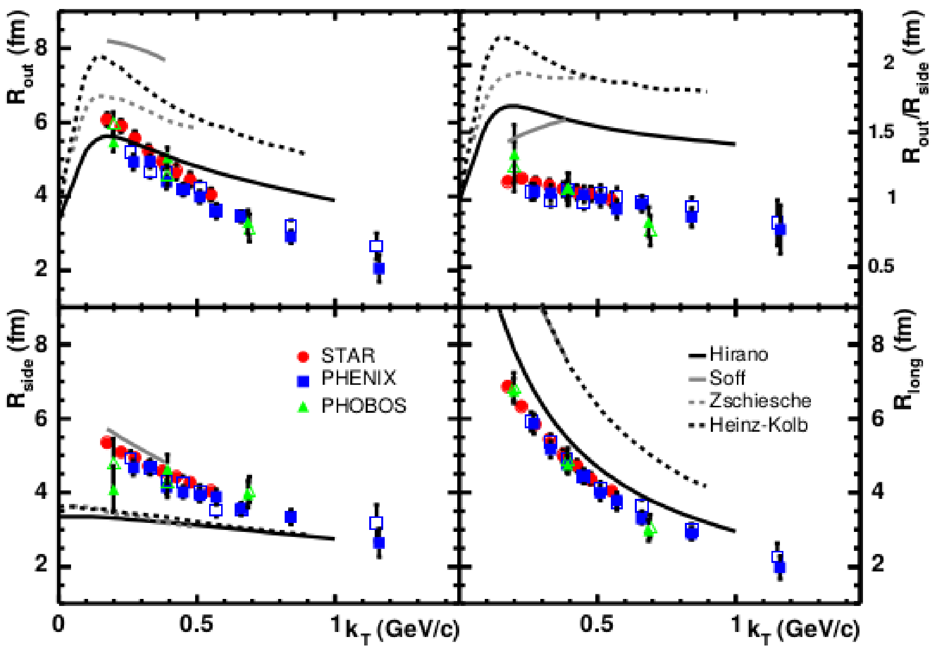

Figure 5.12: Hydrodynamic and hybrid hydrodynamic/cascade models calculations in comparison to RHIC data from Au+Au collisions at $\sqrt{s_{NN}} = 200\,GeV$. Open symbols represent data from π^- π^- correlations and closed symbols for π^+ π^+ correlations. Taken from [59].

than out-plane. The second way is to set $R_y > R_x$ for $\rho_0 \neq 0$ but $\rho_2 = 0$. This case also generates positive elliptic flow because there are more sources emitting in-plane than out-plane.

There is an assumption that this model is longitudinally boost-invariant. The assumption means that the freeze-out occurs with a distribution in a longitudinal proper time $\tau = \sqrt{t^2 - z^2}$. The model assumes a Gaussian distribution peaked at τ_0 with the width $\Delta\tau$

$$\frac{dN}{d\tau} \sim exp(-\frac{(\tau - \tau_0)^2}{2\Delta\tau^2}). \tag{5.54}$$

We assume that, although the source emits particles over a finite duration in proper time τ, none of the source parameters changes with τ. The calculation of the time dependence of these parameters requires a true dynamical model which is too complicated.

The emission function of this model has a follow form

$$S(x, K) = m_T cosh(\eta - Y)\Omega(r, \phi_s) e^{\frac{-(\tau-\tau_0)^2}{2\Delta\tau^2}} \sum_{n=1}^{\infty} (\pm)^{n+1} e^{-nK\cdot u/T}, \tag{5.55}$$

where upper (lower) sign is for bosons (fermions). The reduction of the sum to the first term will transform the model to Boltzmann thermal distribution. After some steps

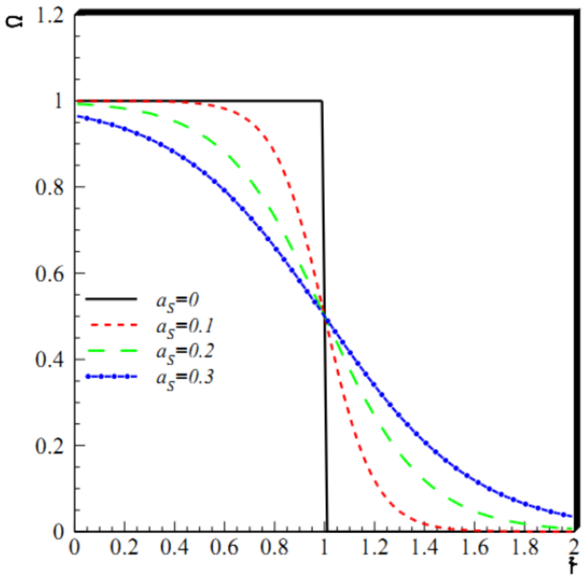

Figure 5.13: The source weighting function Ω versus normalized elliptical radius $\tilde{r}$. The surface diffuseness parameter is changed for several values. Taken from [71].

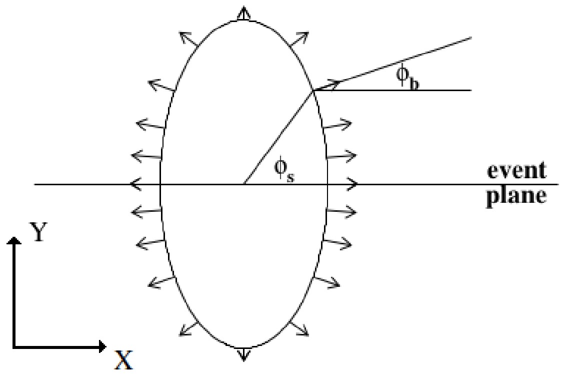

Figure 5.14: Schematic illustration of an elliptical sub-shell of the source. Here the source is extended out of the reaction plane $R_x < R_y$. Taken from [71].

which can be wieved in [71] the emission function can be rewritten as

$$S(x,K) = m_T cosh(\eta - Y)\Omega(r,\phi_s)e^{\frac{-(\tau-\tau_0)^2}{2\Delta\tau^2}\sum_{n=1}^{\infty}(\pm)^{n+1}e^{n\alpha cos(\phi_b-\phi_p)}e^{-n\beta cosh(\eta-Y)}}, \tag{5.56}$$

where we define

$$\begin{aligned} \alpha &= \frac{p_T}{T} sinh[\rho(r,\phi_s)] \\ \beta &= \frac{m_T}{T} cosh[\rho(r,\phi_s)]. \end{aligned} \tag{5.57}$$

One can simplify the equation by setting $Y = 0$. Also, we introduce a function

$$\left\{B'\right\}(K) = \sum_{n=1}^{\infty}\left\{(\pm)^{n+1}\int_0^{2\pi} d\phi_s \int_0^{\infty} rdr[2K_1(n\beta)B'(x,K)e^{n\alpha cos(\phi_b-\phi_p)}\Omega(r,\phi_s)]\right\}. \tag{5.58}$$

Then, p_T spectrum can be calculated as

$$\frac{dN}{p_T dp_T} = \int d\phi_p \int d^4x\, S(x,K) \propto m_T \int d\phi_p \{1\}(K) \tag{5.59}$$

and v_2 is calculated as

$$v_2(p_T, m) = \frac{\int_0^{2\pi} d\phi_p \{cos(2\phi_p)\}(K)}{\int_0^{2\pi} d\phi_p \{1\}(K)}. \tag{5.60}$$

For us the most important conclusion from the work [71] are the HBT radii and their dependence on the parameterization of the source. Using this parameterization one can obtain that R_l^2 carries information about the lifetime of the source and can be parametrized as

$$R_l^2(m_T) = \tau_0^2 \frac{T}{m_T} \frac{K_2(m_T/T)}{K_1(m_T/T)}. \tag{5.61}$$

and that this equation coincides with equation 5.45 from work [83]. It is possible to show that the R_s^2 contains only spacial information and the R_o^2 is sensitive to the temporal extents of the source. The dynamical properties of the measured system than can be described by the ratio of R_o^2 and R_s^2 as well as the difference of R_o^2 and R_s^2. For more detailed analysis we recommend to read [71].

5.4 Particle correlation of non-identical particles

Up to now we have considered only emission of identical particles for which the average value of the projection of the separation vector in the PRF on any direction is equal to zero due to symmetry. However, there are also cases when the emitted particles are non-identical. For these situations one can study space-time asymmetries in the emission. These asymmetries will lead to the non-zero average value of the projection of the separation vector. Before we start, we emphasize that each vector and variable with sign $(*)$ is considered in the PRF where the low relative momentum in the pair rest frame corresponds to close velocities, but not momenta, in the laboratory frame.

As in the case of identical particles, we assume that Coulomb interaction dominates. Under these circumstances the correlation function takes the form [57]

$$C(\vec{p}_1, \vec{p}_2) = A_c(\eta)[1 + 2\frac{\langle r^*(1 + cos(\theta^*))\rangle}{a_c}], \tag{5.62}$$

where θ^* is an angle between relative momentum $\vec{k}^*$ and relative position $\vec{r}^*$ vectors and $\langle ... \rangle$ denotes averaging which is defined by the equation 5.34. One can notice very important feature of the equation (5.62), namely that it is asymmetric with respect to the sign of $cos(\theta^*)$. So for negative $cos(\theta^*)$, $\vec{k}^*$ and $\vec{r}^*$ are anti-aligned, which means that particles will fly towards each other and then they fly away. In that case they spend more time close to each other and thus one expects a larger correlation. If vectors $\vec{k}^*$ and $\vec{r}^*$ are aligned, ($cos(\theta^*) > 0$), then particles fly away from each other immediately and time of the correlation will be smaller than in previous case so correlation will be weaker. For imaging see (Fig.5.15)

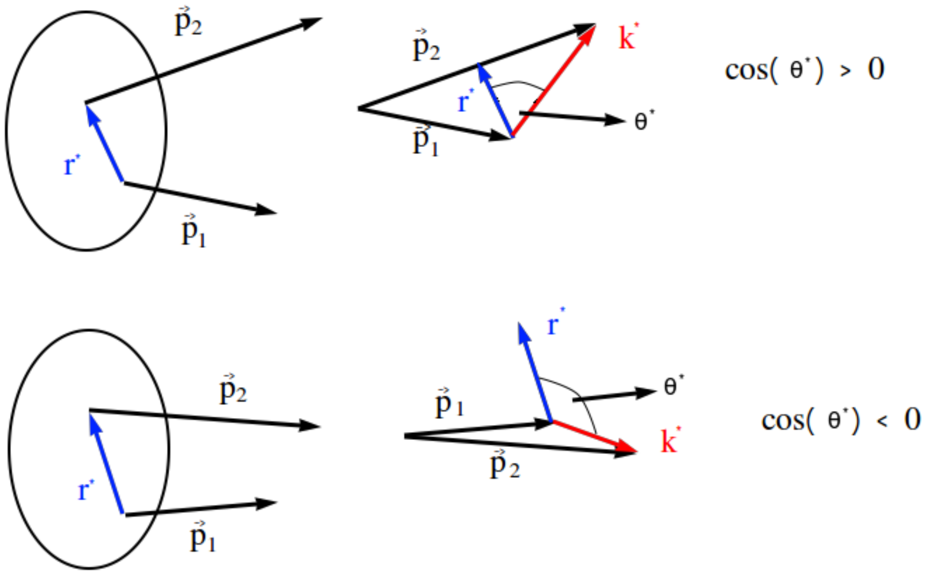

Figure 5.15: Sketch of relationship between vector k^* and r^* for positive and negative value of cosine.

In order to measure that correlation one problem must be solved, namely the angle θ^* is not experimentally measurable. Therefore we have to find another way. However, we have one more angle which we can select. It is the angle Ψ between total pair momentum $\vec{P}$ (or velocity) and pair relative momentum k^*. If one considers restriction to the transverse plane then the pairs of correlated particles can be divided into two groups:

1. $\vec{k^*}$ and $\vec{P}$ are aligned $\rightarrow cos(\Psi) > 0 \equiv k^*_{out} > 0$
2. $\vec{k^*}$ and $\vec{P}$ are anti-aligned $\rightarrow cos(\Psi) < 0 \equiv k^*_{out} < 0$

where k^*_{out} is the component of the relative momentum of the first particle projected into the out-direction. In general, there are also possible projections, into the side or long direction but for our case out-direction is sufficient. The main idea is sketched in (Fig.5.16).

Here we define two functions. The first one is with pairs having $cos(\Psi) > 0$ and we will denote it as C^+. The second function is for pairs with $cos(\Psi) < 0$ which is denoted with C^-. One can show that these functions are identical if the average emission points of the two particle species are the same. However, for non-zero difference between average emission points of particles species in the given out-direction, the function will

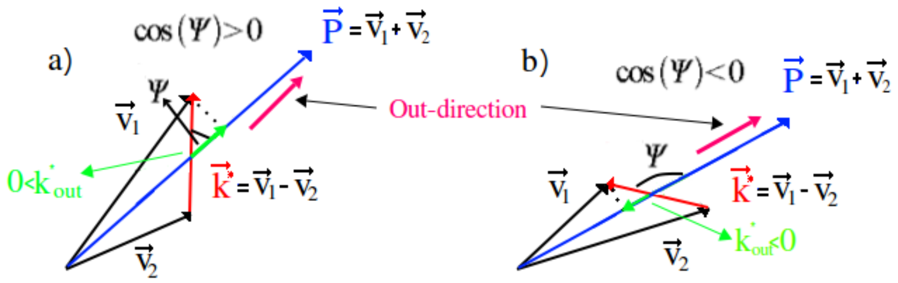

Figure 5.16: Asymmetry in space-time emission seen by non-identical particle correlations.

be different. What one can observed in the "double ratio" C^+/C^-. One can show that thanks to symmetry $\langle r_{side}\rangle = 0$ and in the system with a symmetric rapidity coverage $\langle r_{long}\rangle = 0$. Then for $\langle r_{out}\rangle$ we can write down

$$\langle \Delta r_{out}\rangle = \langle \gamma(\langle \Delta r^*_{out}\rangle - \beta\langle \Delta t\rangle)\rangle. \tag{5.63}$$

From this equation we can conclude that observed asymmetry comes from space and time components [56].

To imaging our conclusion, let us suppose that we have any source that can emit particles, for this case let us have one pion and kaon. In the first asymmetry case, we will have particles that are emitted from different points (spatial asymmetry) of the source at the same time. We assume that the pion will be emitted from the point that is closer to the center. Two cases are possible. The first one is that the pion is faster than kaon, then the pion catches up the kaon, $k^*_{out} > 0$. The second case is that the pion is slower than the kaon, afterwards the kaon moves away from the pion, $k^*_{out} < 0$. In the second asymmetry (time asymmetry), we suppose that particles are emitted from the same space-point but in different time. The kaon is considered as emitted before pion. Thus pion catches up kaon. In both cases when the pion catches up the kaon the duration of interaction is longer than correlation effect is stronger. In case when the kaon moves away from the pion time of the interaction is shorter and thus the correlation effect will be small.

By convention, k^*_{out} is calculated for lighter particles. Thus $k^*_{out} > 0$ means that the lighter particle transverse velocity is larger and vice-versa what corresponds with (Fig.5.16). From experiment, see (Fig.5.17), we can conclude for $\pi - K$ and $\pi - p$ systems that C^+ is larger than C^-. This indicates that pions are emitted at a different average space-time point than kaons and protons. Theoretically this effect can be described by model with collective expansion that suggests that pions are emitted closer to the center of the source than kaons or protons.

Another possible way how to obtain information about shift in average emission points between two non-identical particles is decomposition of correlation function into

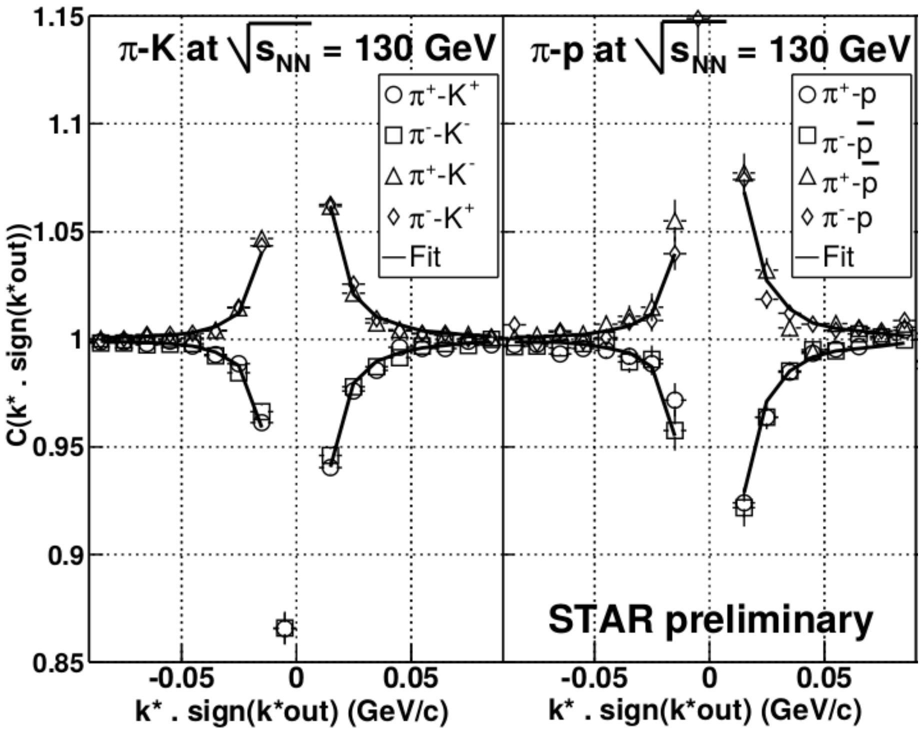

Figure 5.17: Correlation function for $\pi - K$ and $\pi - p$. Taken from [70].

spherical harmonics[41] [73]

$$A_{lm}(k^*) = \frac{\Delta_{cos\theta}\Delta_\varphi}{\sqrt{4\pi}} \sum_{i}^{bins} Y_{lm}(\theta_i, \varphi_i])C(k^*, \cos\theta_i, \varphi_i), \tag{5.64}$$

where θ, φ and k^* are spherical coordinates and $\Delta_{\cos\theta} = \frac{2}{N_{\cos\theta}}$, $\Delta_\varphi = \frac{2\pi}{N_\varphi}$ are bin sizes in $\cos\theta$ and φ, respectively. Coefficients (A_{lm}) appearing in the decomposition above represent different symmetries of the source. For azimuthally symmetric identical particle source at mid-rapidity, only A_{lm} with even values of l and m do not vanish. For non-identical particle correlations the coefficients with odd values of l and m are allowed.

The $A_{00}(k^*)$ coefficient represents angle-average correlation functions while $A_{11}(k^*)$ measures a shift of the average emission point in the R_{out} direction. In the (Fig.5.18) we can observed decomposition coefficients A_{00} and A_{11} for π and Ξ particles. As can be seen, A_{11} is non-zero that indicates that the average space-time emission points of these particles are not the same [73].

5.5 Non-femtoscopic correlation

So far, we have not considered the size of the collision system. We have worked with the correlations that describes system such as Au+Au or Pb+Pb. Here, Bose-Einstein

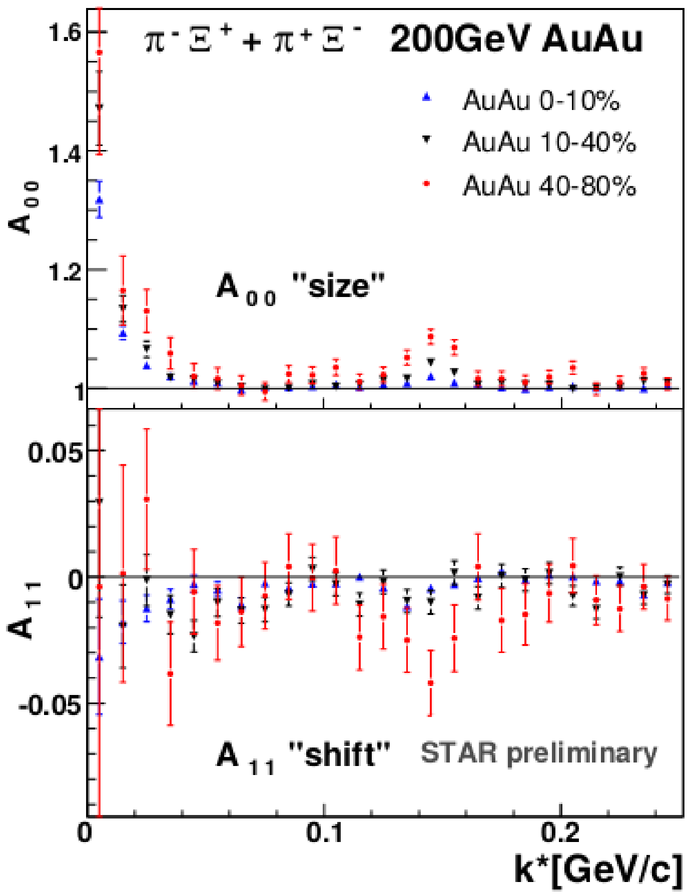

Figure 5.18: Comparison of $A_{00}(k^*)$ and $A_{11}(k^*)$ coefficients of spherical decomposition for combined sample of like-sign $\pi^\pm$ $\Xi^\pm$ and unlike-sign $\pi^\pm$ $\Xi^\mp$ pairs from 10% most central Au+Au collisions with the FSI model predictions. Taken from [73].

correlation and FSI, which are referred to as femtoscopic correlations, play important role. However, for smaller systems such as p+p, p+Au, d+Au the situation is more complicated and the method, which is described above, has to be modified for elementary particle collisions. For these small systems we have to include additional two-particle correlation effects that are referred to as non-femtoscopic correlations [32]. The well-known example of such additional correlations is the correlation induced by total energy and momentum conservation laws or jet/string fragmentation. These correlations are not directly related the spatio-temporal scales of the emitter but they have an influence on the interpretation of the momentum dependence of the interferometry radii in small system collisions [33].

Therefore, the general correlation function for small system collision has a form

$$C(\vec{q},\vec{k}) = C_F(\vec{q},\vec{k})C_{NF}(\vec{q},\vec{k}), \tag{5.65}$$

where C_F is normal correlation function for femtoscopic correlations that was derived in previous subsections and C_{NF} denotes non-femtoscopic correlations. The examples of analysis where non-correlation effects are not negligible are [86], [42]. An example of the correlation function where non-femtoscopic correlations can not be negligible is depicted in (Fig. 5.19). Here, we can see an approximate ranges where individual correlations take a part in.

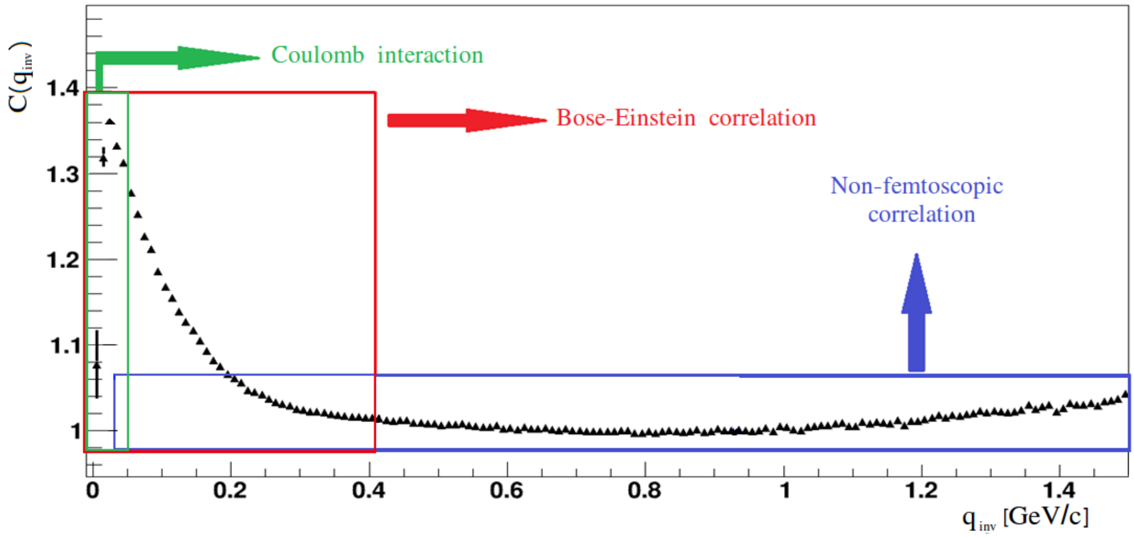

Figure 5.19: The correlation function from p+Au collisions and approximate ranges for individual correlations.

5.6 Femtoscopy of d(p)+Au collisions at RHIC

Before we start to present our femtoscopic measurement we introduce our motivation. In our analysis we would like to study typical features from collective behaviour such as multiplicity or k_T dependences of the correlation functions and HBT parameters. In this section we will describe some femtoscopic results for charged pions from other experiments that were measured at RHIC. We start with the results from large system created in Au+Au collisions. Than we compared results from Au+Au collisions with results from d+Au collisions and at the end of this section more precise analysis of d+Au collisions will be described.

Femtoscopy measurements in Au+Au collisions

Presented results for Au+Au collisions at $\sqrt{s_{NN}} = 200\,GeV$ were published in [27]. In the (Fig.5.20) we can see HBT parameters as a function of m_T and centrality.

On the right figure the HBT parameters R_{out}, R_{side}, R_{long} and λ are depicted for the $0-5\,\%$ most central events as a function of m_T for $\pi^+\pi^+$ and $\pi^-\pi^-$ correlation functions. We can observe an agreement between the parameters extracted from the positively and negatively charged pion analysis. The λ parameter increases with m_T while the HBT radii decrese with m_T.

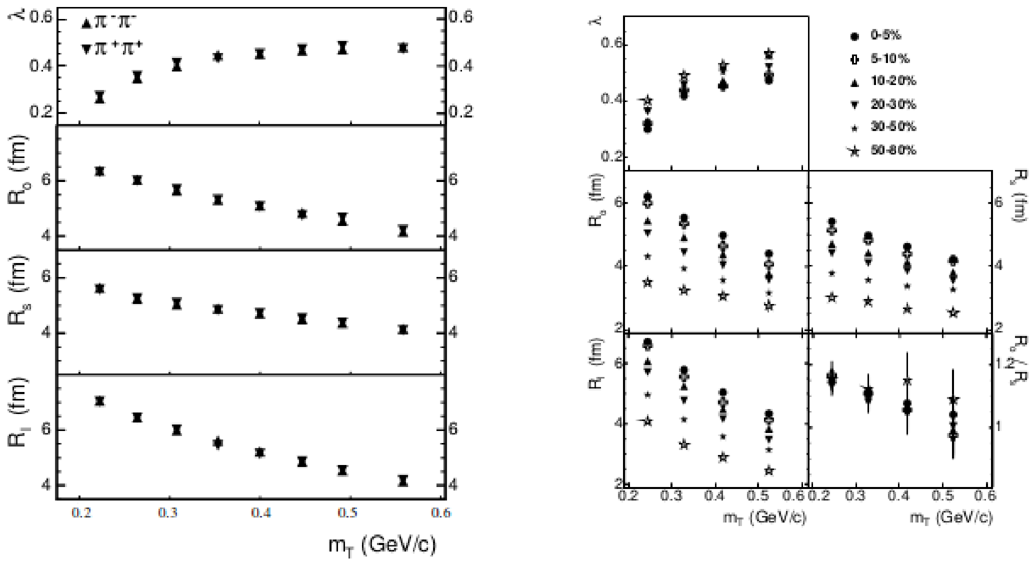

Figure 5.20: On the left figure the dependence of the HBT parameters for $0-5\,\%$ most central events for $\pi^+\pi^+$ and $\pi^-\pi^-$ correlation functions are shown. On the right figure the HBT parameters for 6 different centralities as a function of m_T are shown. Taken from [27]

On the right figure the bahaviour of HBT parameters is depicted as a function of m_T for 6 different centralities. The λ parameter slightly increases with decreasing centrality while the three radii increase with increasing centrality. This m_T dependence is typical for transversal expanding system.

Comparison of the femtoscopy results for Au+Au and d+Au collisions at RHIC

This part includes two charged pion interferometry results for d+Au and Au+Au collisions at $\sqrt{s_{NN}} = 200\,GeV$ [30]. The comparisons, which are performed as a function of collision centrality and the mean transverse momentum for pion pairs, indicate strikingly similar patterns for the d+Au and Au+Au systems. Additionally, results for d+Au collisions indicate a smaller freeze-out size of the system.

In the (Fig.5.21) we can see a comparison for these two collision systems. The left figure shows a comparison of a m_T dependence of R_{out}, R_{side} and R_{long} for $0-10\,\%$ central d+Au and $60-88\,\%$ central Au+Au collisions. The radii for d+Au and Au+Au show a decreasing trend with increasing values of m_T.

Subfigure (a) on the right side, shows m_T dependence of the ratio R_{out}/R_{side}. This ratio is flat or gently decreasing that means that the R_{out} radius is comparable to R_{side}

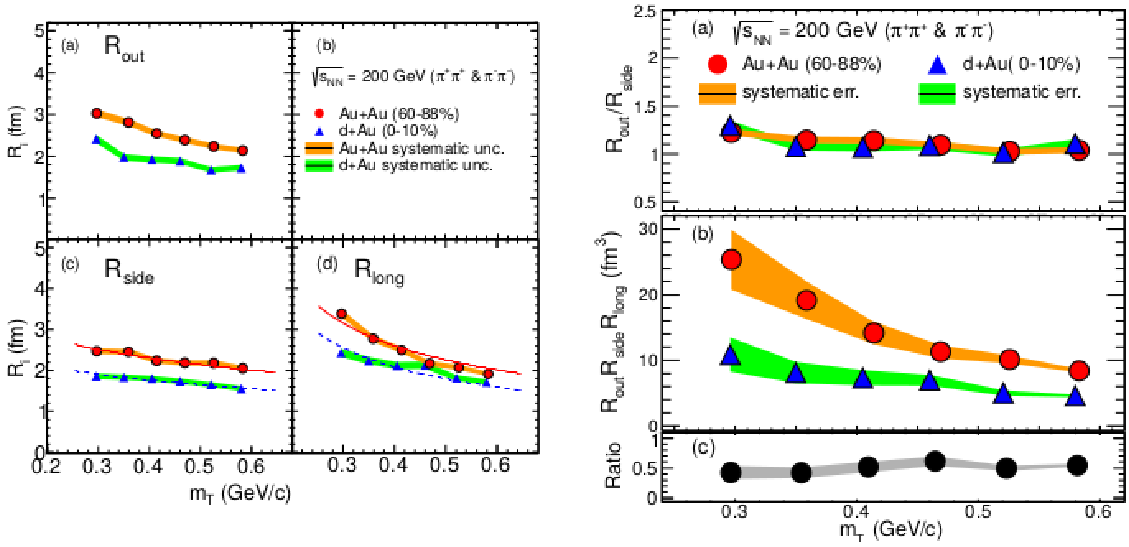

Figure 5.21: Left figure shows m_T dependence of the HBT radii for $0-10\,\%$ central $d{+}Au$ and $60-88\,\%$ central $Au{+}Au$ collisions. Right figure shows ratios of the radii and system volumes and magnitudes of the volumes for $d{+}Au$ and $Au{+}Au$ collisions. Taken from [30]

for both systems. Subfigure (b) illustrates the difference via the m_T dependence of the freeze-out volume that is evaluated as $(R_{out} \times R_{side} \times R_{long})$. The magnitudes of the freeze-out volumes for $Au{+}Au$ are larger. In the last subfigure (c) shows that within uncertainties, the fall-out with increasing m_T is comparable for $d{+}Au$ and $Au{+}Au$.

This excellent agreement between the patterns for the $d{+}Au$ and $Au{+}Au$ collisions suggests trends commonly associated with hydrodynamic-like expansion in $d{+}Au$ collisions.

Previously $p{+}Au$ collisions were not available at RHIC however, in [86] a signal for $p{+}Au$ was extracted from peripheral $d{+}Au$ collisions. In the (Fig.5.22), the centrality and m_T dependence of the HBT radii for $d{+}Au$ collisions is shown. On the left figure we can see results for four k_T bins and three centralities in which a parameterization of the femtoscopic correlations was made by the same model however, for a description of non-femtoscopic correlations three different models were used. From this figure one can see that non-femtoscopic correlation can not be neglected as they influence the HBT radii significantly.

On the right figure we can see comparisons of the HBT radii obtained from $p{+}Au$ collisions, which were separated from the most peripheral $d{+}Au$ collisions, with results from $d{+}Au$ and $p{+}p$ collisions. For description of femtoscopic correlations the same model was used for all type of collisions and the non-femtoscopic correlations were neglected. It is interesting to see that the obtained R_{out} and R_{side} from $p{+}Au$ collisions are smaller then the one from $d{+}Au$ collisions while there is not much difference in

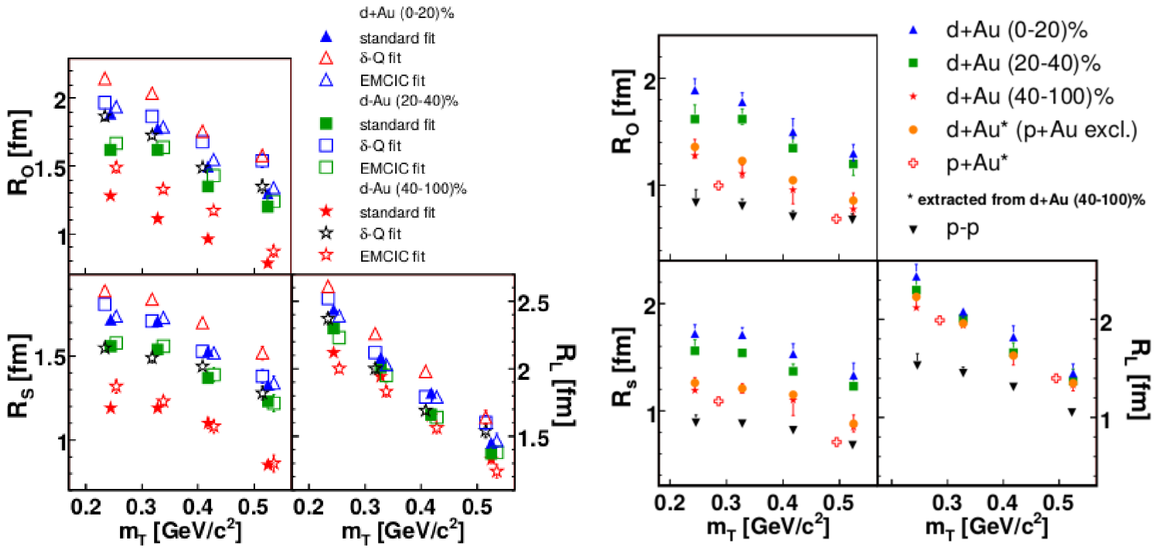

Figure 5.22: Left figure shows the m_T dependence of HBT radii for three centralities for $d+Au$ collisions in which various parametrization of non-femtoscopic correlation were used. Right figure shows the m_T dependence of HBT radii for three centralities from $d+Au$, $p+Au$ and $p+p$ collisions.

R_{long}. Additionally, the values of R_{out} and R_{side} are comparable to results from $p+p$ collisions. This fact suggests that the geometrical size of the homogeneity region is sensitive to the smaller nuclei participating in the collisions.

Chapter 6

Data analysis and results

In this thesis we present femtoscopic measurements for $p{+}Au$ collisions at $\sqrt{s_{NN}} = 200\,GeV$ from the STAR experiment. The following chapter is divided into two parts. In the first part, we describe the analysis procedure where the dataset, event selection, track selection and pion identification are explained. In the second part we present preliminary measurements of the femtoscopic correlation for positive and negative pions. Result fitting parameters will be extracted and discussed for 1-dimensional correlation functions while in 3-dimensional analysis we show multiplicity and average pair transverse momentum dependence (k_T) of the correlation functions.

6.1 Datasets

Our presented datasets originate from $p{+}Au$ collisions at $\sqrt{s_{NN}} = 200\,GeV$ that were measured at the STAR experiment in 2015, (Run 15) with a minimum bias trigger using the BBC and VPD detectors. The used datasets:

- Production: P16id
- Trigger: BBCMB, VPDMB-novtx, VPDMB-30
- Off-line Trigger ID: 500008, 500018, 500004, 500904
- Number of events with selected triggers: $\sim 130\,M$ (before event cuts)

At the end of the trigger selection we obtain $\sim 130\,M$ events. Subsequently, different kind of cuts are applied to these events to assure the good data quality. After these cuts, we have datasets that can be used for analysis. In the next three sections, we describe cuts that we have used here.

6.2 Event selection

For our analysis the selection of events in the center of the TPC is required therefore a cut on the position of the primary vertex along the beam direction (z-axis) was applied. Our requirement for this cut is $|V_z| < 30\,cm$, where V_z is the z-coordinate of the primary vertex position which is measured by the TPC. In (Fig.6.1) one can see the distribution of the z-coordinate of the primary vertex position. Tails of the histogram for primary vertex in z-direction do not contain enough counts and therefore they are not included in analysis. In the triggering, events are protected against badly detected events and pile-up (situation where a detector is affected by several events at the same time). One can use an additional cut to further suppress the effects of pile-up and bad event reconstruction. It is known that V_z can also be calculated by the VPD detectors. Therefore we require a difference between the vertex position measured by the TPC and VPD detectors in an absolute value to be less than $5\,cm$,

$$|V_z^{TPC} - V_z^{ZDC}| < 5\,cm. \tag{6.1}$$

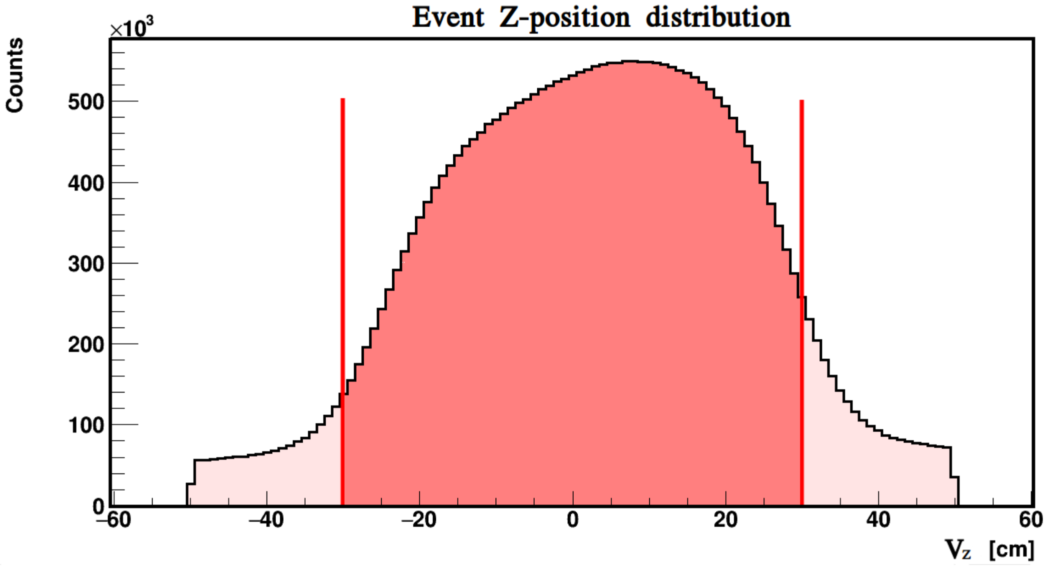

Figure 6.1: The distribution of the z-coordinate of the primary vertex position. Events between $|V_z| < 30\,cm$ were analyzed.

For comparison, in Au+Au collisions we can use just $3\,cm$ for this difference because in these collisions we have better resolution of the primary vertex position.

Event Multiplicity

In our analysis the reference multiplicity was used. Usually, using Glauber model we are able to calculate centrality bins for the corresponding multiplicity however, in the case of $p+Au$ collisions the calculations have not been available at the time of writing this thesis. Therefore we have divided reference multiplicity into the four equal intervals as can be seen in (Fig.6.2). For these multiplicity bins we will construct correlation functions that will be shown later in this chapter.

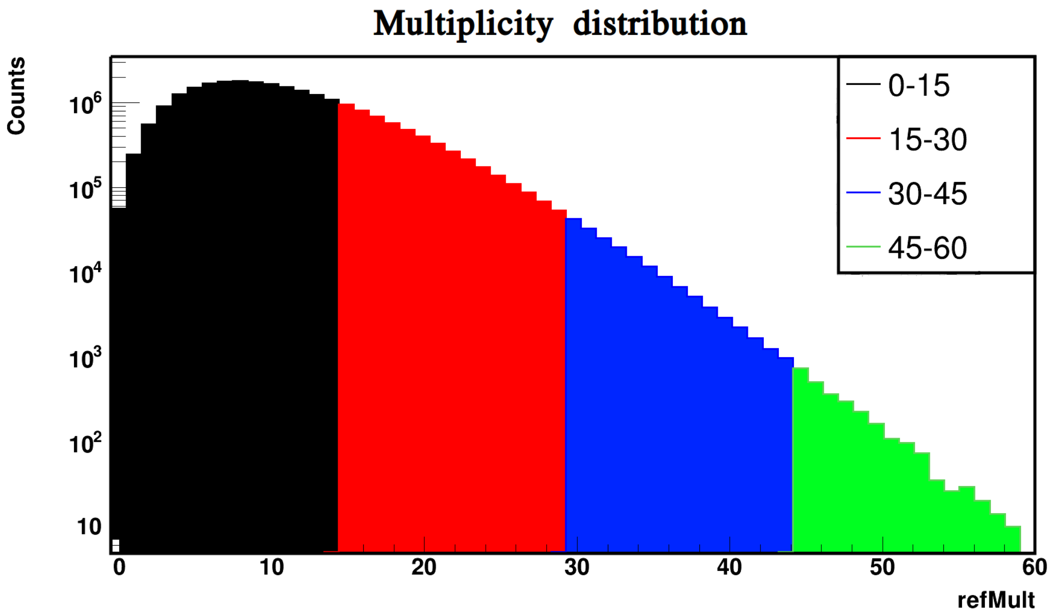

Figure 6.2: Distribution of the reference multiplicity for $p+Au$ collisions divided into the four equal bins.

6.3 Particle selection

In the next step, the tracks from events which passed through event cuts, will be treated by particle cuts, where one would like to choose cuts for obtaining pions. Particle identification was done by the TPC and TOF detectors.

In analysis presented here, there is specific p_T cut which was applied to single tracks because the TPC enables to detect particles with the transverse momentum larger than $0.15\,GeV/c$. Moreover, we also applied another cut for momentum of single particles due to limitations in the identification of pions at high momentum using dE/dx, see (Fig.6.3). Therefore, only tracks with

$$0.15 < p_T < 1.5GeV/c$$

were included into our analysis. In addition to make sure that emitted particles fall into the detector acceptance there is a requirement for primary tracks to be in a pseudo-rapidity range

$$-1 < \eta < 1.$$

In the TPC the particle identification is based on the energy losses of the particles, which travel through a gas inside the detector. These losses depend on the velocities at which particles travel in the TPC. It means that for a given momentum, three particles with different masses have different velocities and thus they have different dE/dx, as can be seen in (Fig.6.3). As was mentioned in Chapter 4 (4.2.1), energy losses of charged particles by ionization are calculated using the Bethe-Bloch formula, see (Eq.4.1). For us, the positive and negative charged pions are the most important.

Due to finite resolution of the TPC, one can expect deviation in the measured energy loss from the theoretically expected value. In a case that the measured distribution of the specific energy loss has a Gaussian distribution with the mean value determined by the theoretical value of dE/dx^{theory} and with the standard deviation σ_π, the normalized energy loss for pion can be defined as

$$n\sigma_\pi = \ln\Big(\frac{(dE/dx)^{measured}}{(dE/dx)^{theory}}\Big)/\sigma_{dE/dx}, \tag{6.2}$$

where $(dE/dx)^{measured}$ is the measured value of the energy loss. The normalized energy loss is scaled by the resolution $\sigma_{dE/dx}$. In our analysis we required to tracks to have

$$-2 \leq n\sigma_\pi \leq 2. \tag{6.3}$$

By applying this cut the hadron contamination can be significantly suppressed up to momentum $p <\sim 0.55 GeV/c$. However, for higher values of the momentum ($p >\sim 0.55\, GeV/c$), there is some contamination from other particles such as protons or kaons. In order to solve this problem with the contamination we had to apply a cut on mass squared of the particles by means of the TOF detector.

We have mentioned in section (4.2.2) that the TOF detector measures the time of flight τ. When this time information is combined with the measured momentum in the TPC detector, the particle mass squared, m^2, can be calculated by

$$m^2 = p^2\Big(\frac{1}{\beta^2} - 1\Big), \tag{6.4}$$

this formula is from (Eq.4.3). Thanks to this capability of the TOF detector we are able to separate charged pions from kaons and protons up to $p \sim 1.5\, GeV/c$. Since the mass of the charged pion is $m_{\pi^\pm} = 0.1395\, GeV/c^2$ therefore the last identification cut requires the tracks to have the mass squared in the range

$$0.005 < m_\pi^2 < 0.035.$$

In the (Fig.6.4) we can see mass squared distribution after applying the mass squared cut.

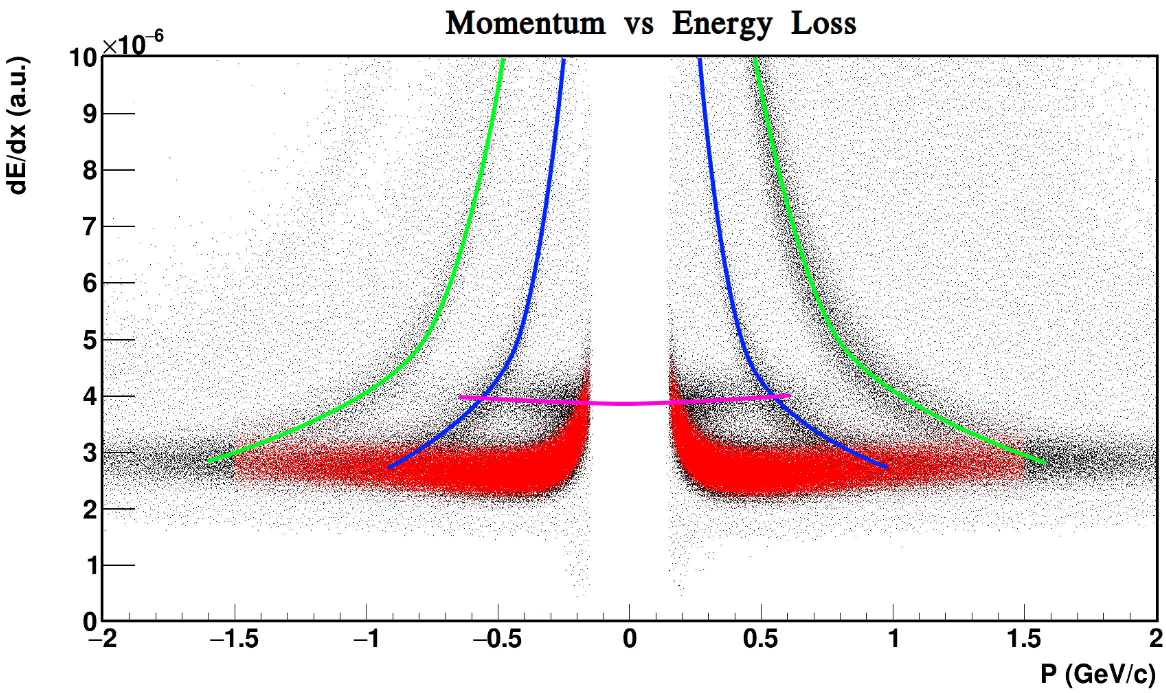

Figure 6.3: dE/dx vs. momentum of the particles for pions (red line), kaons (blue line), protons (green line) and elentrons (pink line).

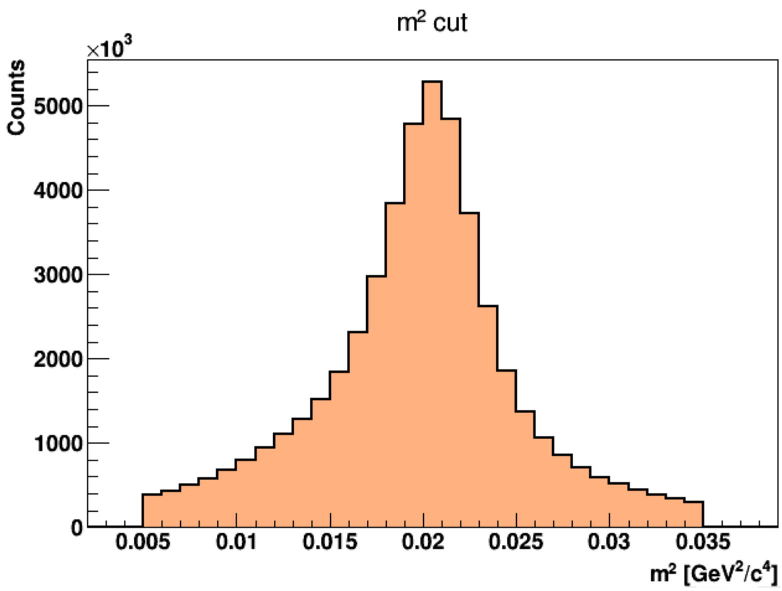

Figure 6.4: The distribution of the mass squared of positively charged pions which was determined by the TOF detector.

6.4 Pair cut

For the particle pairs only one cut was applied. It was cut on the average pair transverse momentum (k_T) that is defined as

$$\vec{k}_T = \left(\frac{\vec{p}_{1T} + \vec{p}_{2T}}{2}\right) \tag{6.5}$$

where $\vec{p}_{1T}$ and $\vec{p}_{2T}$ are the transverse momenta of the first and second particle of the pair, respectively. It has been already discussed that homogeneity regions are expected to depend on the pair transverse momentum. Therefore such k_T bins enable us to change the size of the measured volume at the constant multiplicity and temperature of the system. Our requirement for the transverse momenta is to have an average value between

$$0 < k_T < 1.5\, GeV/c.$$

This k_T range was divided into five bins:

$0.0–0.3\, GeV/c$, $0.3–0.6\, GeV/c$, $0.6–0.9\, GeV/c$, $0.9–1.2\, GeV/c$, $1.2–1.5\, GeV/c$.

In our analysis cuts that are intended to remove the effects of two track reconstruction defects that can have impact on the HBT measurements at low relative momentum were not considered. The mentioned effects are

- Splitted tracks: one single particle reconstructed as two tracks
- Marged tracks: two particles with similar momenta reconstructed as one track

These effects are expected to significantly suppressed since we require separate TOF matching for each particle.

6.5 Experimental approach of the correlation function

As it was mentioned above, correlation function is what we measure in experiment and in order to obtain the HBT radii from this function, we have to fit the measured correlation function. The experimental correlation function is defined as

$$C(\vec{q}, \vec{k}) = \frac{A(\vec{q})}{B(\vec{q})}, \tag{6.6}$$

where $A(q)$ is formed with particles from the same events and represents the distribution of the two particle probabilities for the relative pair momentum, (real pairs). $B(q)$ is formed by mixing particles in separate events and represents the single particle probabilities, (mixed pairs). Mixed pairs are made by event mixing technique. Here we select several different events with similar global variables and then particle pairs are made by choosing one particle from a event and choosing one particle from other event. Therefore the mixed pairs does not include the HBT effect, while the real pairs, from the same events, includes the HBT effect and interactions.

6.6 Results

Datasets for $p+Au$ collisions that were analyzed above will be now used for a construction of the correlation functions that will be analyzed in the following part of this work in detail. Our study of the experimental correlation functions will be performed for the positive and negative charged pions in **1-dimensional** case. In **3-dimensional** analysis we show k_T and multiplicity dependencies of the 3-dimensional correlation functions.

6.6.1 1D-correlation function

In (Fiq.6.5 and Fiq.6.6) is shown typical behaviour of the 1-dimensional correlation functions as the functions of multiplicity and k_T, respectively.

In the (Fig.6.5) the multiplicity dependence of these functions is plotted for positive and negative pions and for tree different k_T bins. As can be seen with increasing multiplicity the correlation function get weaker. This behaviour can be interpreted as follow: for higher multiplicity (more central collision) the created system is larger that indicates that homogeneity region will be also larger and as we know from (Eq. 5.23) with larger radius the correlation function is smaller.

In the (Fig.6.6) the k_T dependence for positive pions is shown for three different multiplicity bins. We can see that with increasing k_T the correlation functions also increase and that means that radii of homogeneity regions decrease. This is in a an agreement with prediction from section (5.3). For the negative pions we can observed the same behaviour, see in Appendix D.

The 1-dimensional fits of our experimental correlation functions were performed by two simple models that incorporate only Bose-Einstein correlation. These simple models are

$$C_{Gauss}(\vec{q},\vec{k}) = 1 + \lambda(\vec{k})e^{-(q_{inv}R_{inv}(\vec{k}))^2} \tag{6.7}$$

$$C_{Levy}(\vec{q},\vec{k}) = 1 + \lambda(\vec{k})e^{-|q_{inv}R_L(\vec{k})|^\alpha}. \tag{6.8}$$

The first equation is well known correlation function that is based on Gaussian distribution, here q_{inv} is the Lorentz invariant momentum defined in (Eq. 5.24), R_{inv} is the Lorentz invariant radius and λ is the chaoticity parameter. The second correlation function is based on the Levy distribution [44] [65], where R_L is the Levy scale parameter and α is the Levy index, also known as index of stability, which can be equal to the values $0 < \alpha \leq 2$. There are two specific case for α parameter:

- $\alpha = 2 \rightarrow$ - in this case the source function is normal Gaussian distribution function

$$S_{\vec{k}}(\vec{x}) = \frac{1}{\sqrt{2\pi R_G^2}} e^{-\frac{(x-x_0)^2}{2R_G^2}}, \tag{6.9}$$

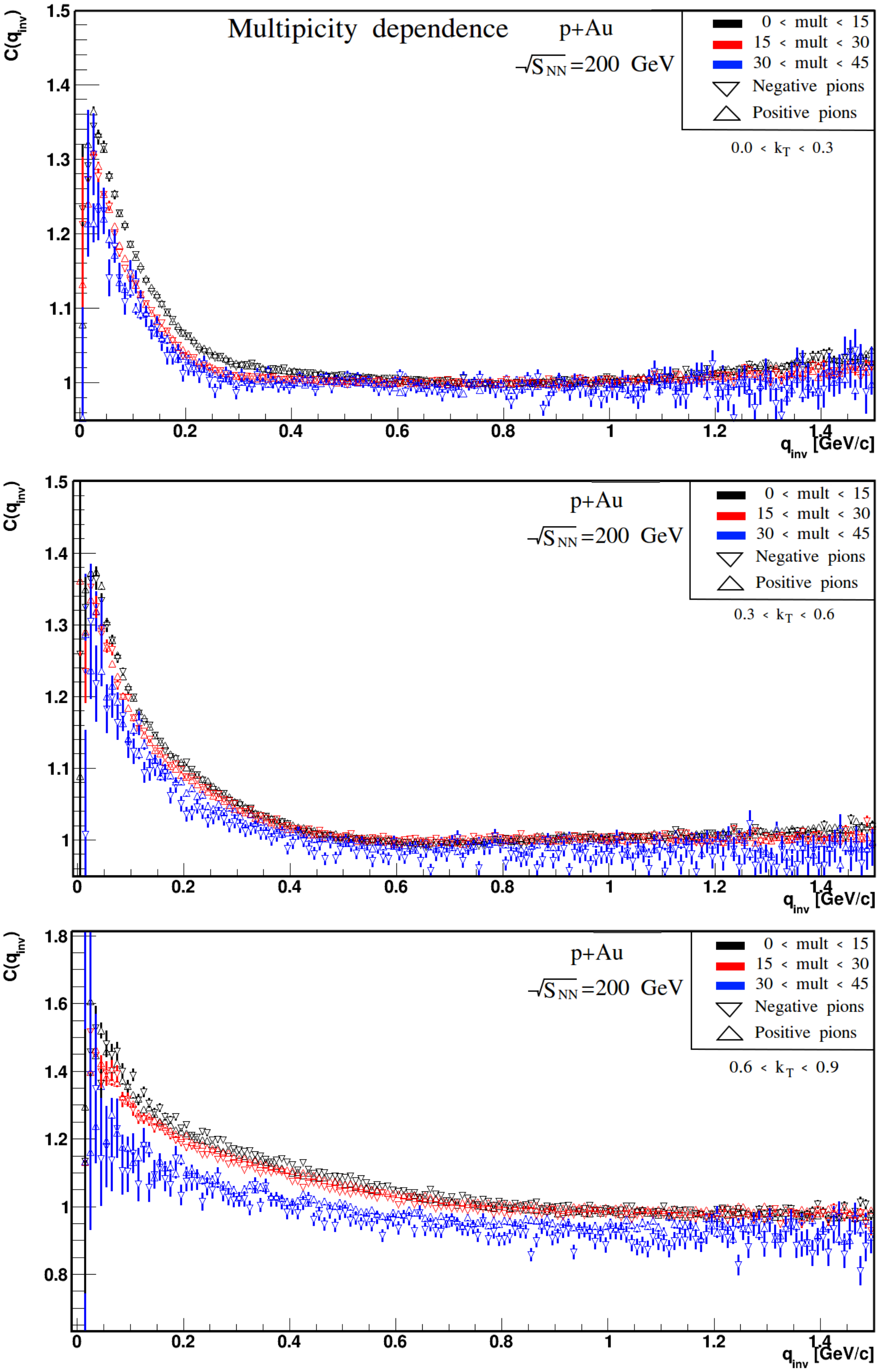

Figure 6.5: 1-dimensional correlation functions for the charged pions that are plotted for 3 multiplicity bins and 3 k_T bins.

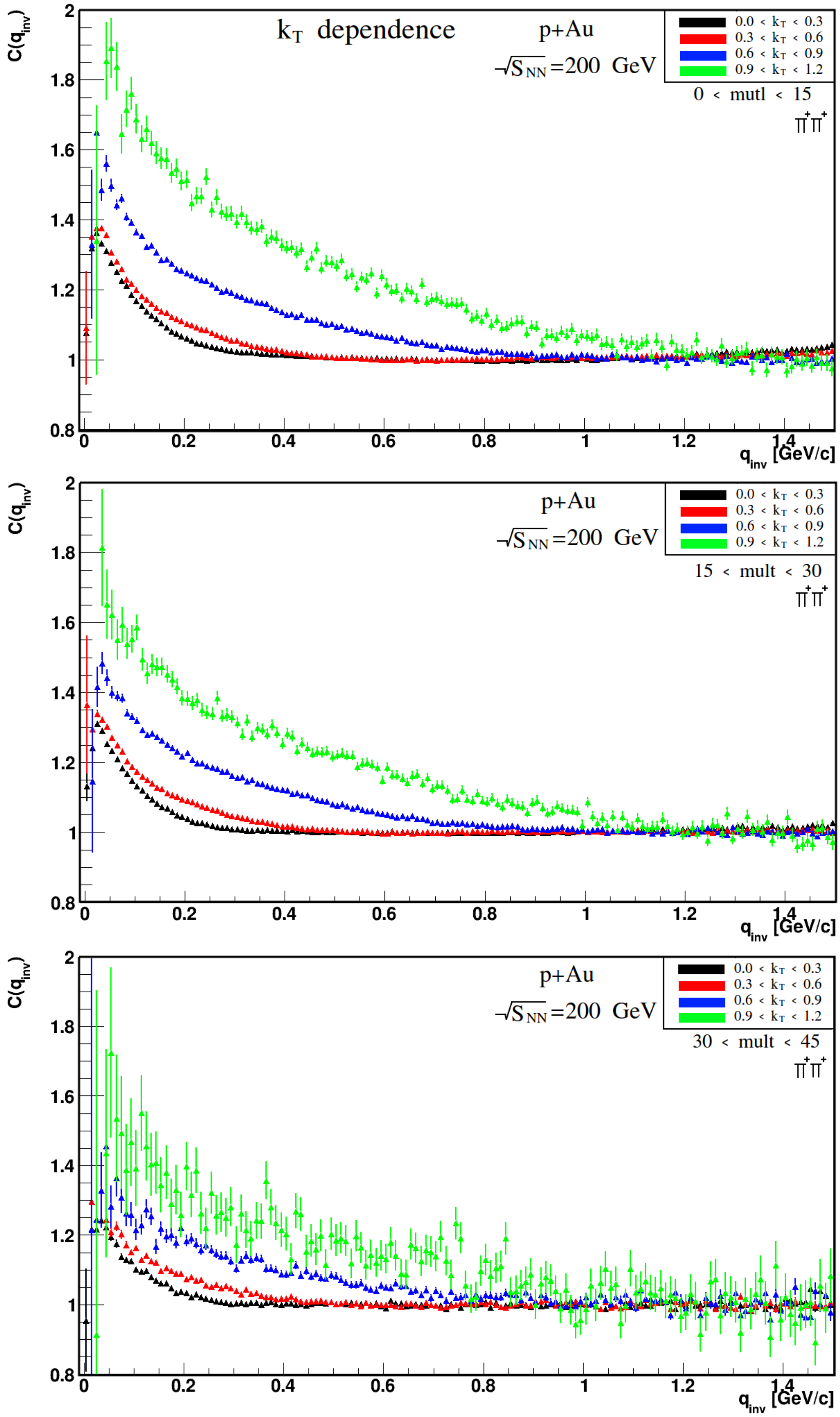

Figure 6.6: 1-dimensional correlation functions for the positive charge pions for 4 k_T bins and 3 multiplicity in bins.

where the Gaussian scale parameter, $R_G^2 = \langle x^2 \rangle - x_0^2$, is the standard deviation.

- $\alpha = 1 \rightarrow$ - in this case the source function corresponds to the Cauchy distribution function
$$S_{\vec{k}}(\vec{x}) = \frac{R_c}{\pi(R_c^2 + (x - x_0)^2)}, \tag{6.10}$$
with scale parameter R_c.

The reason why we use this Levy function is based on the observations of results from $d{+}Au$ collisions. In these collisions the distribution of the source had the non-Gaussian shape. Therefore one can expect that in $p{+}Au$ collisions the non-Gaussian source will be also present and since Levy distribution has more free parameters it is able to better describe non-Gaussian source [44][65].

In the (Fig.6.7) one can see the 1-dimensional correlation functions for the positive pions for multiplicity bin $0 - 15$. The fits were performed up to $q_{inv} = 1.5\,GeV/c$ for each multiplicity bin. Due to poor statistic was not possible to extract correlation functions for multiplicity bin $45 - 60$ and for $1.2 < k_T < 1.5$. Therefore k_T is divided only into the 4 bins for each multiplicity bin. The Coulomb interaction is not included here, it means that fits do not start from the $q_{inv} = 0\,GeV/c$ but start points are shifted to the values between $\sim 0.05 - 0.15\,GeV/c$. The correlation functions for multiplicity bins $15 - 30$, $30 - 45$ and for the negative pions have the same behaviour. Therefore, we show only parameter fit results of these functions and we will not depicted them here. However, they can be found in Appendix D.

As can be seen from the comparison of the fits, in all cases the fits are better described by the Levy fitting function than the Gaussian fitting function. This observation indicates that the source function is of non-Gaussian shape. In the (Fig.6.8) and (Fig.6.9) we can see R_{inv} and R_L scale parameters for positive and negative pions, respectively, as a function of the multiplicity and k_T. For these results the radii behaviour qualitatively agrees with the effect expected from a system undergoing a transverse expansion where pairs with the larger k_T are emitted from a smaller homogeneity region than the pairs with the smaller k_T. However, we do not observe strong multiplicity dependence in the extracted radii which is actually seen in the (Fig.6.5). One would expect that with higher multiplicity the radii of the homogeneity region increase however, it is hard to confirm this fact from these results. This may be caused by non-femtoscopic effects.

In the (Fig.6.10) and (Fig.6.11) can be observed the dependence of the λ and α parameter for positive and negative function, respectively, as a fucntion of k_T. The magnitude of α parameter lies in range $\sim 0.9 - 1.6$, this fact indicates the non-Gaussian source. The behaviour of the λ parameter is not monotonic. It slightly decreases up to $k_T \approx 0.5\,GeV/c$ but then it increases for both, positive and negative case of correlation functions.

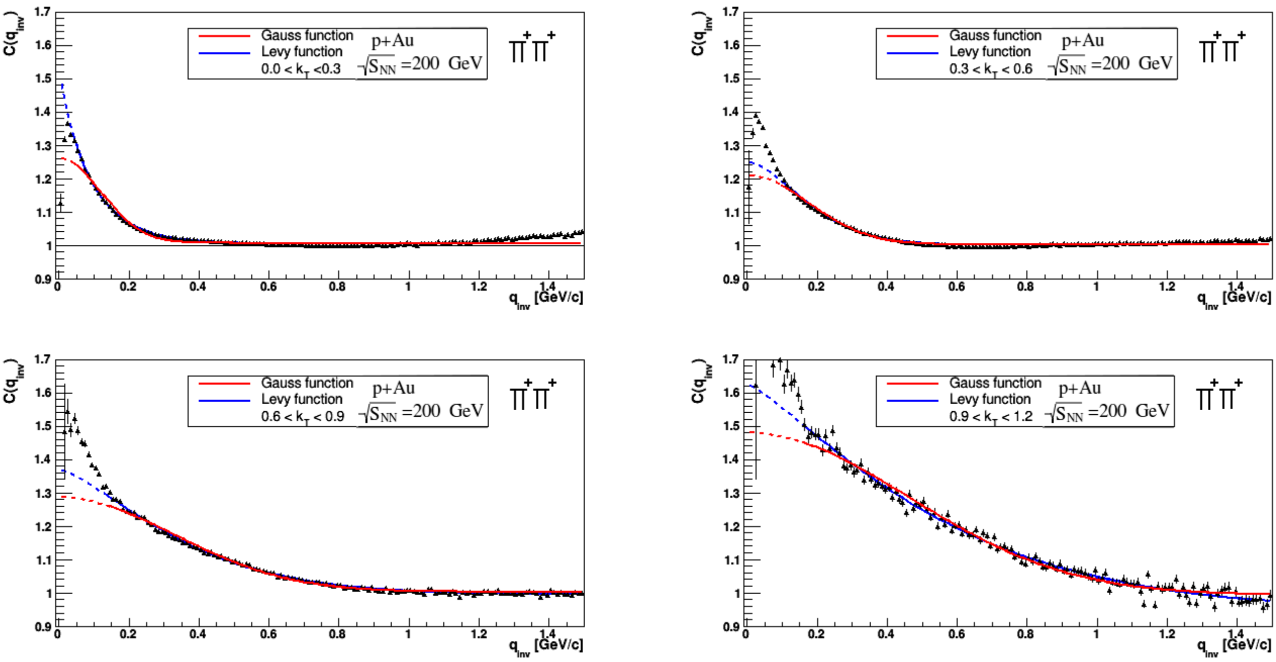

Figure 6.7: Correlation functions for the positive pion in multiplicity range $0-15$ for 4 different k_T bins.

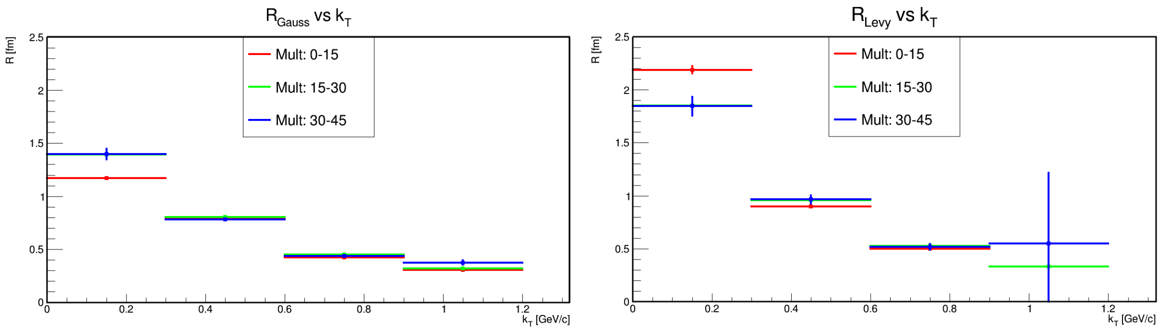

Figure 6.8: k_T dependence of R_{inv} and R_L scale parameters for positive pions for Gauss fit function (Eq.6.7) (left) and Levy fit function (Eq.6.8) (right).

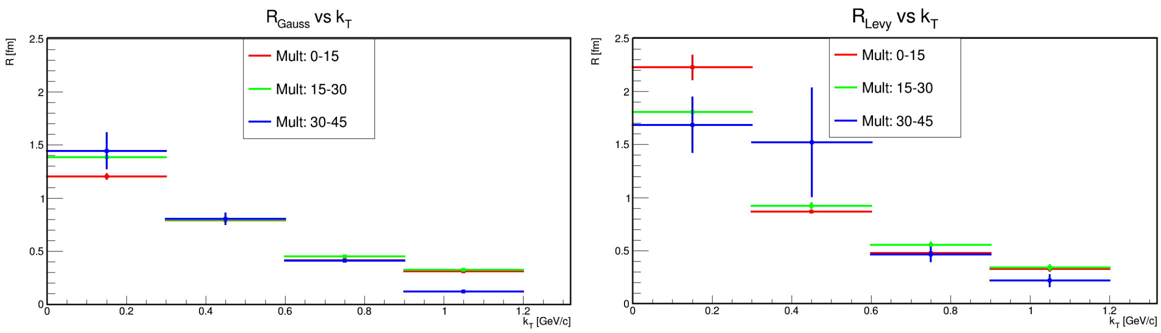

Figure 6.9: k_T dependence of R_{inv} and R_L scale parameters for negative pions for Gauss fit function (Eq.6.7) (left) and Levy fit function (Eq.6.8) (right).

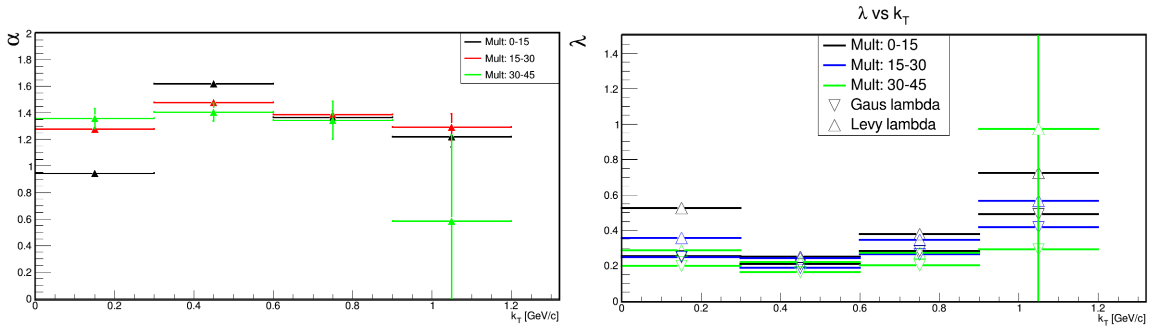

Figure 6.10: On the left figure is shown the dependence of Levy α parameter on k_T. On the right figure is shown the dependence of λ parameter on k_T. Both parameters are for positive pions.

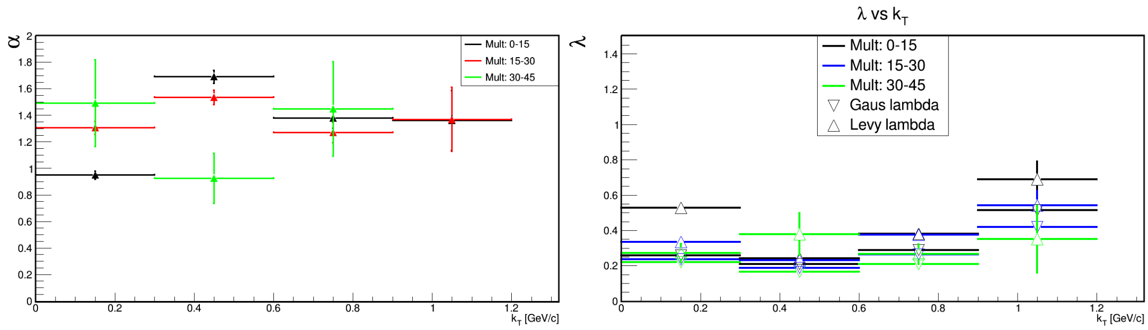

Figure 6.11: On the left figure is shown the dependence of Levy α parameter on k_T. On the right figure is shown the dependence of λ parameter on k_T. Both parameters are for negative pions.

In the next step of our analysis, the fits do not end in $q_{inv} = 1.5\,GeV/c$ but they are performed for the different fitting ranges for each multiplicity and k_T bin. Here we use the same fitting models as in previous case where the Coulomb interaction is not included. It is clear that this is not a systematic fitting technique but the reason why we do that is that the non-femtoscopic effects significantly influence our result parameters. By fitting of our functions on the certain ranges we could exclude some portion of this effects and study how parameter results are influenced by these effects.

In the (Fig.6.12) we can see an example of the correlation functions, in multiplicity range $0-15$, for different fitting ranges. Dashed lines represent fitting models on the whole k_T range while full lines represent used fitting range. Fitting funtions for the next multiplicity ranges can be found in Appendix D.

In the (6.13) and (Fig.6.14) are shown results for R_{inv} and R_L for positive and negative pions, respectively. These scale parameters still behave as in the previous section where the problem with the multiplicity dependence still persists. In the (Fig.6.15) and (Fig.6.16) the behaviour of the λ and α parameters for positive and negative pions is shown. λ has the same non-monotonic behaviour as in the previous case. However,

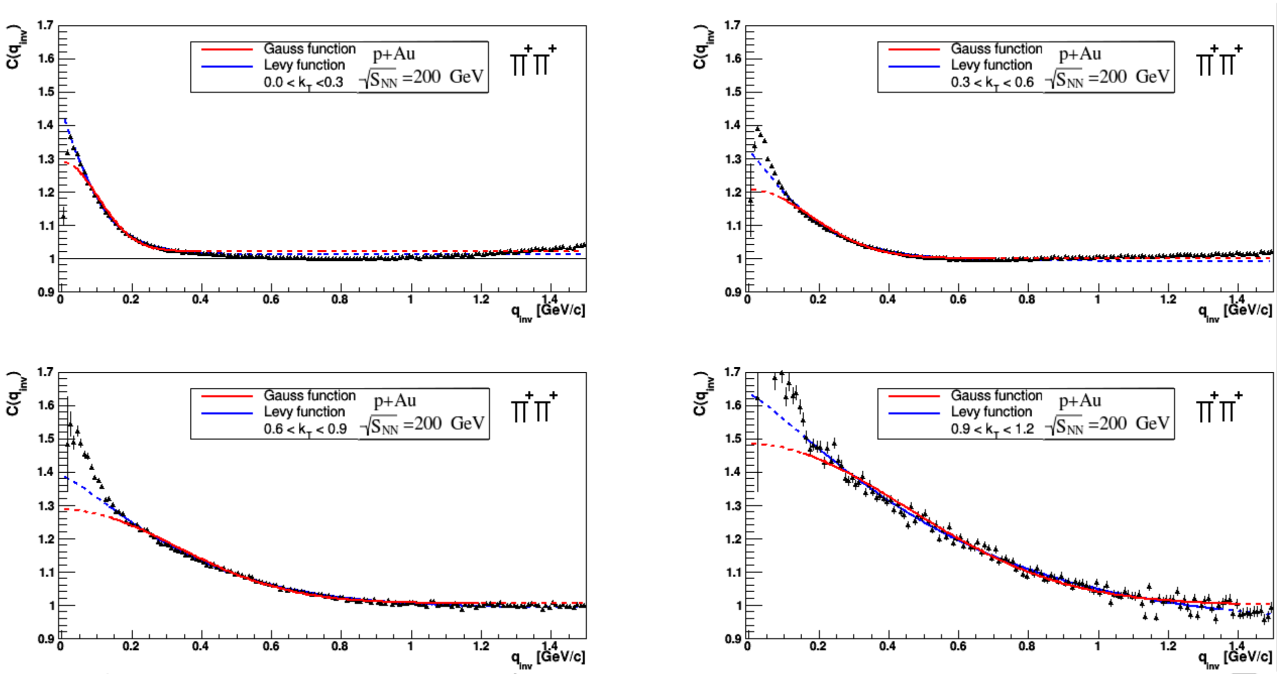

Figure 6.12: Correlation functions for the positive pion in multiplicity range $0-15$ for 4 different k_T bins.

an observed improvement can be seen in the behaviour of the α parameter because values of this parameter are almost constant in the range of $\sim 1.2-1.4$. Additionally, the multiplicity dependence can be observed for both, positive and negative pions.

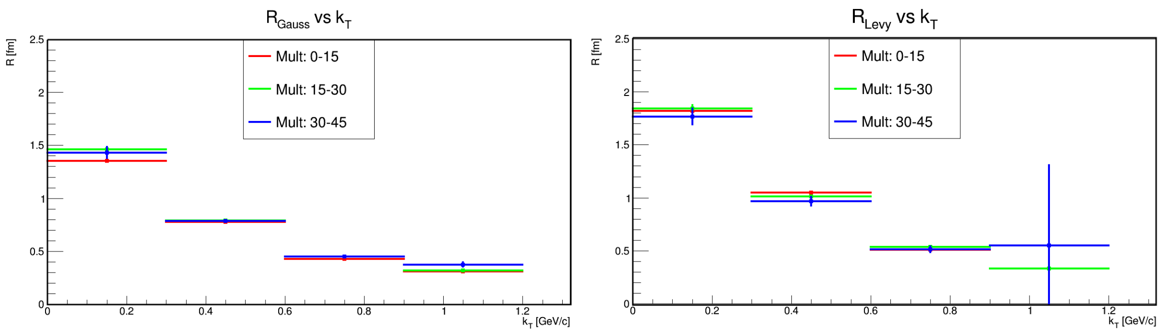

Figure 6.13: k_T dependence of R_{inv} and R_L scale parameters for positive pions for Gauss fit function (Eq.6.7) (left) and Levy fit function (Eq.6.8) (right).

So far, we have not included a part where the Coulomb interaction takes a part. However, we change it now because our fits will be performed in the ranges from $q_{inv} = 0\,GeV/c$ to $q_{inv} = 1.5\,GeV/c$. The fit function which includes Coulomb correction is in the form

$$C(q_{inv}) = (1-\lambda) + \lambda K(q_{inv})(1 + e^{-q_{inv}^2 2R_{inv}^2}), \tag{6.11}$$

where $K(q_{inv})$ is the Coulomb correction and the meaning of the other parameters stay the same as in the previous cases. In the (Fig.6.17) fitting functions for the pair of

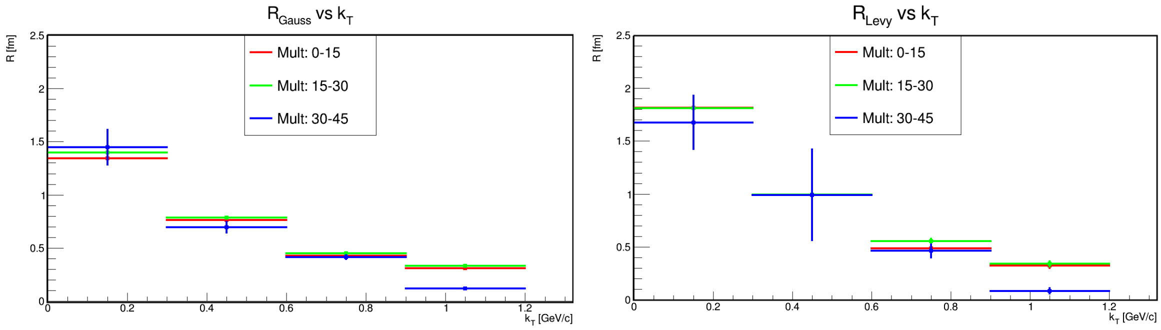

Figure 6.14: k_T dependence of R_{inv} and R_L scale parameters for negative pions for Gauss fit function (Eq.6.7) (left) and Levy fit function (Eq.6.8) (right).

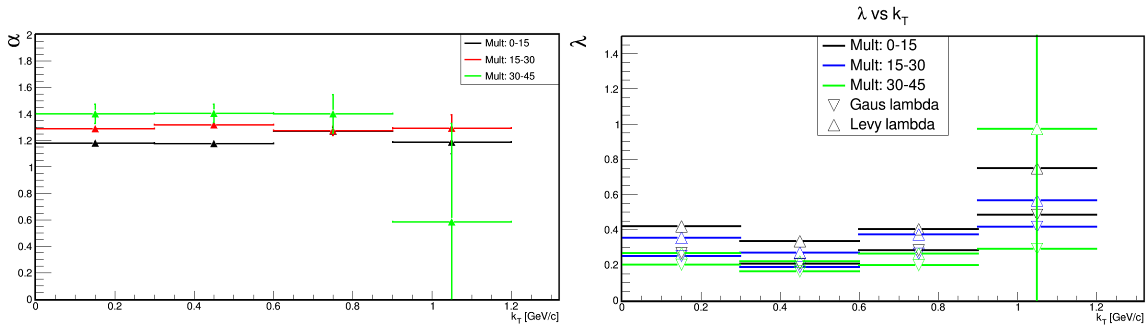

Figure 6.15: On the left figure is shown the dependence of Levy α parameter on k_T. On the right figure is shown the dependence of λ parameter on k_T. Both parameters are for positive pions.

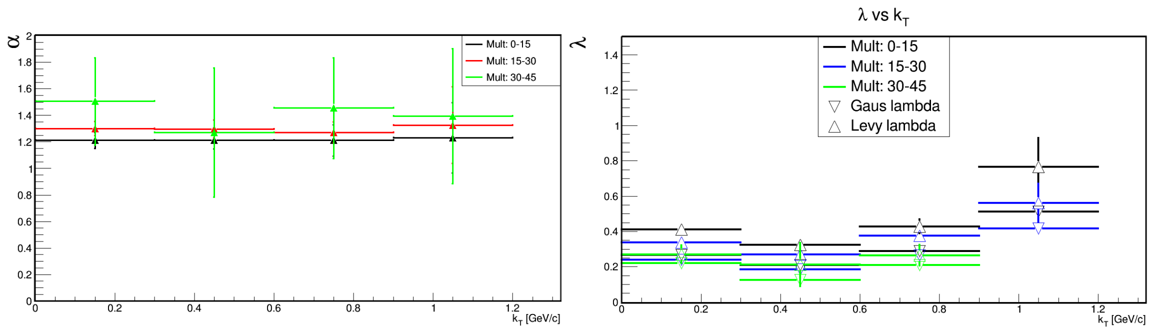

Figure 6.16: On the left figure is shown the dependence of Levy α parameter on k_T. On the right figure is shown the dependence of λ parameter on k_T. Both parameters are for negative pions.

positive pions for multiplicity range $0-15$ are shown. Here we can see that fit functions fail to describe the data, especially for the smaller sources at higher k_T. There are two possible effects that can modify out results. The first one is that the source of the our correlation functions is non-Gaussian. However, fitting function (Eq.6.11) is based on the Gaussian distribution. The second possible reason for that is that the non-correlation effects have enormous impact on the shape of the correlation functions and since the fit function, (Eq.6.11), does not contain any part that includes these effects it is not able to describe these non-correlation effects. Other plots of the fitting functions for positive and negative pions can be found in Appendix D.

In the (Fig.6.18) and (Fig6.19) one can see fitting result parameters for the pair of positive and negative pions, respectively. The λ parameter has the same non-monotonic behaviour as in the previous cases however, the R_{inv} dependence on the k_T is not clear for the last two k_T bins for both, positive and negative pions. The multiplicity dependence is still not observed.

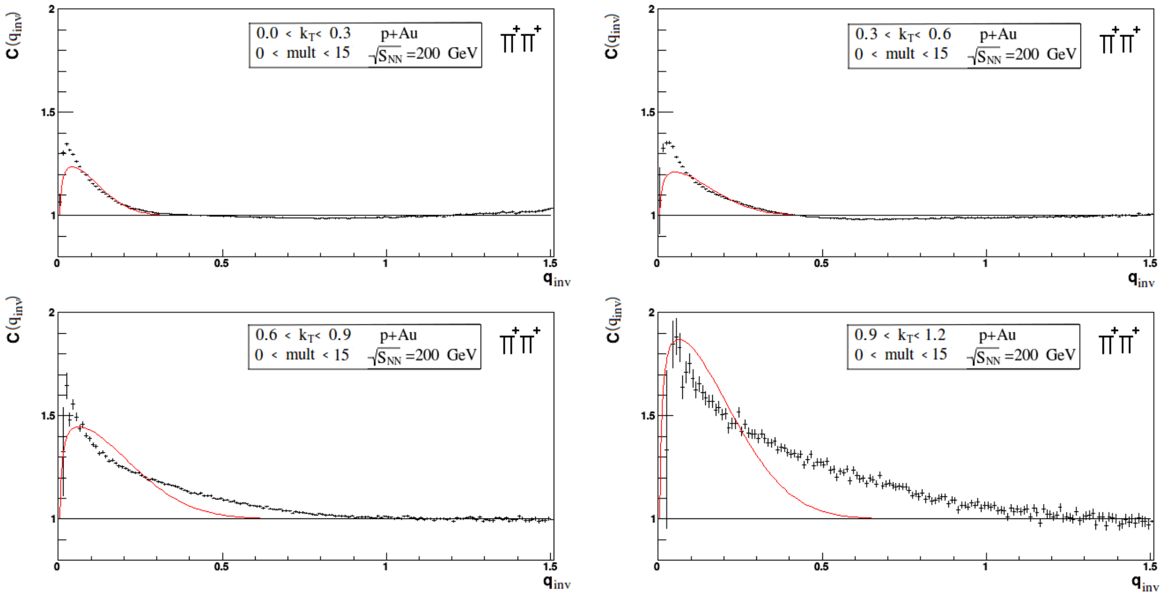

Figure 6.17: Correlation functions for the positive pion in multiplicity range $0-15$ for 4 different k_T bins. Here the Coulomb interaction is also included.

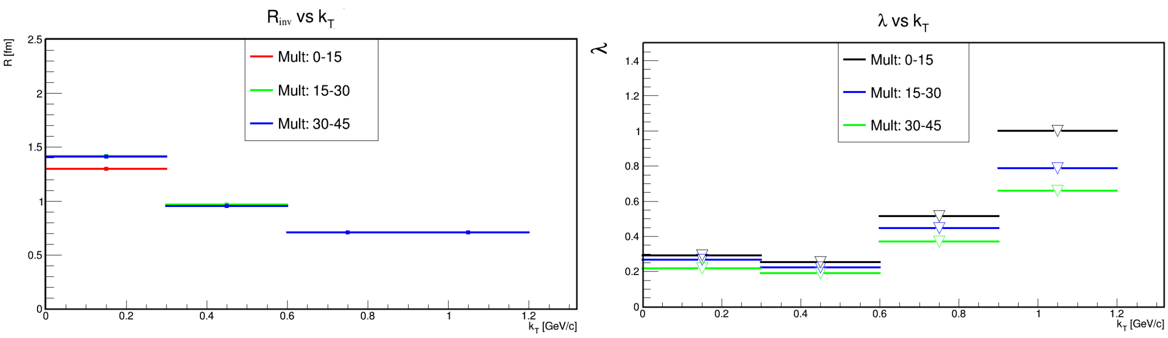

Figure 6.18: Dependence of the R_{inv} parameter as the function of the k_T is shown on the right figure. Dependence of λ parameter on k_T is shown on the right figure. Both parameters are for pair of positive pions.

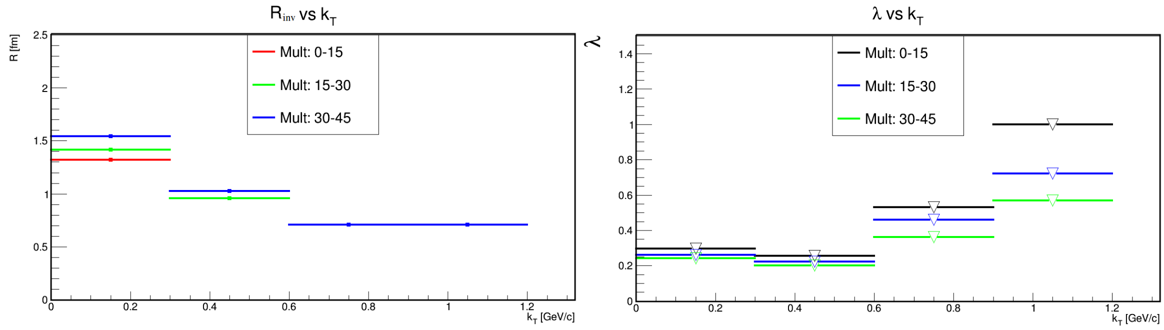

Figure 6.19: Dependence of the R_{inv} parameter as the function of the k_T is shown on the right figure. Dependence of λ parameter on k_T is shown on the right figure. Both parameters are for pair of negative pions.

6.6.2 3D-correlation function

In this section we present results on 3-dimensional correlation functions for the pair of positive pions in LCMS. Here, we want to study the multiplicity and k_T dependence of the correlation functions and mainly to have a better access to the non-femtoscopic correlations. Projection of the correlation functions to the out, side and long axis were done by using an integration range of $60\,MeV$ on the other two axis.

All 3-dimensional functions are normalized in range $0.4 - 0.6\,GeV/c$. From the figures (Fig.6.20), (Fig.6.21), (Fig.6.22) and (Fig.6.23) one can see that this is the best possible choice for normalization region because non-femtoscopic effects modify the shape of the correlation function in all three directions significantly.

In the (Fig.6.20) and (Fig.6.21) one can see k_T dependence of the correlation functions for multiplicity bins $0 - 15$ and $15 - 30$ respectively in all three axis, where with increasing k_T the correlation functions increase.

In the (Fig.6.22) and (Fig.6.23) one can see multiplicity dependence of the correlation functions for k_T ranges $0.0 - 0.3\,GeV/c$ and $0.3 - 0.6\,GeV/c$ respectively in all three axis, where with increasing multiplicity the correlation functions decrease.

The extraction of the HBT radii from these correlation functions is in progress however, due to strong non-femtoscopic effects the fitting of these 3-dimensional correlation functions will be complicated. The method that will be used for fitting is called spherical harmonics.

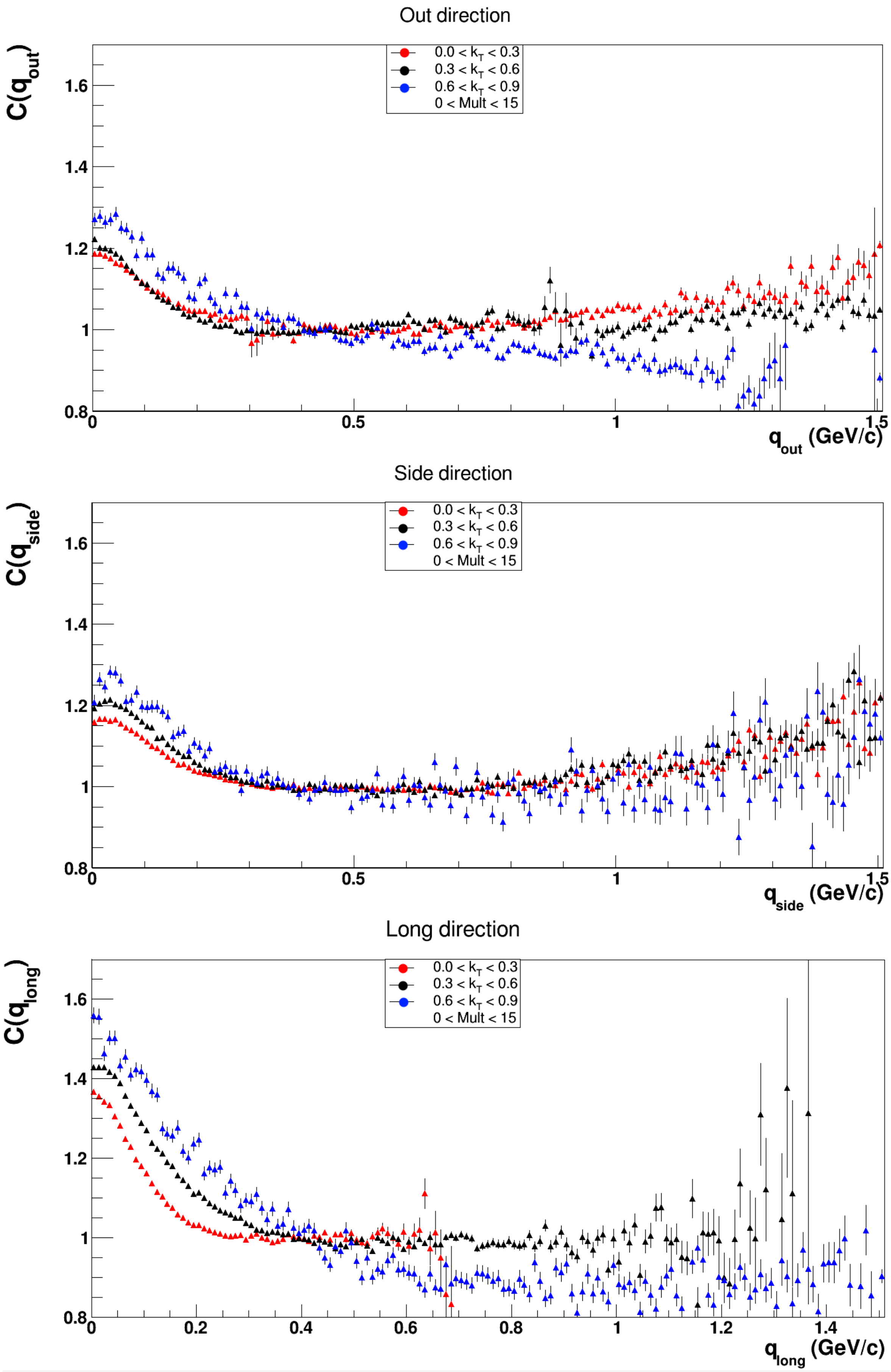

Figure 6.20: The k_T dependence of 3-dimensional correlation functions for the positive charged pions in multiplicity bin $0-15$.

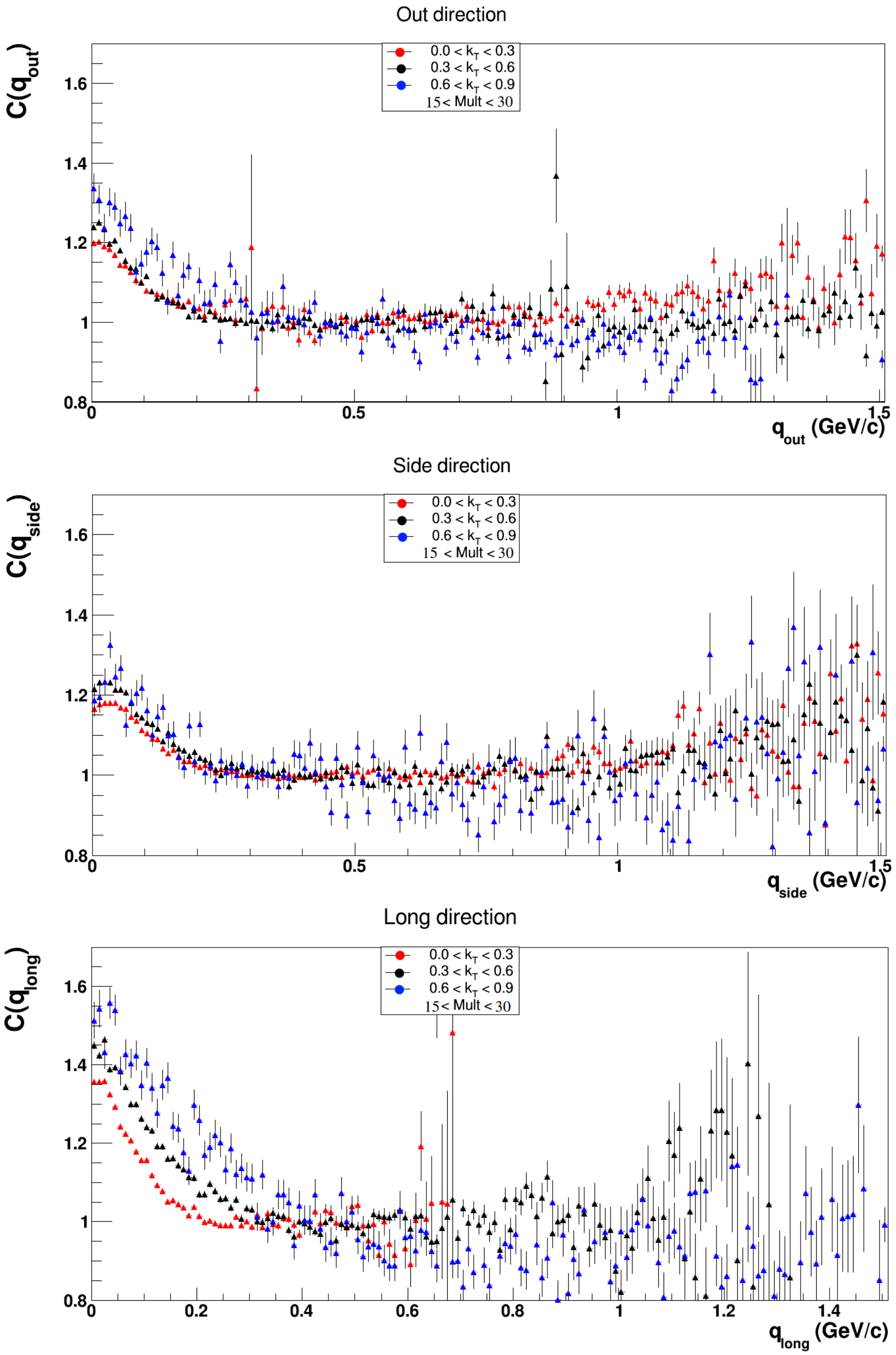

Figure 6.21: The k_T dependence of 3-dimensional correlation functions for the positive charged pions in multiplicity bin $15-30$.

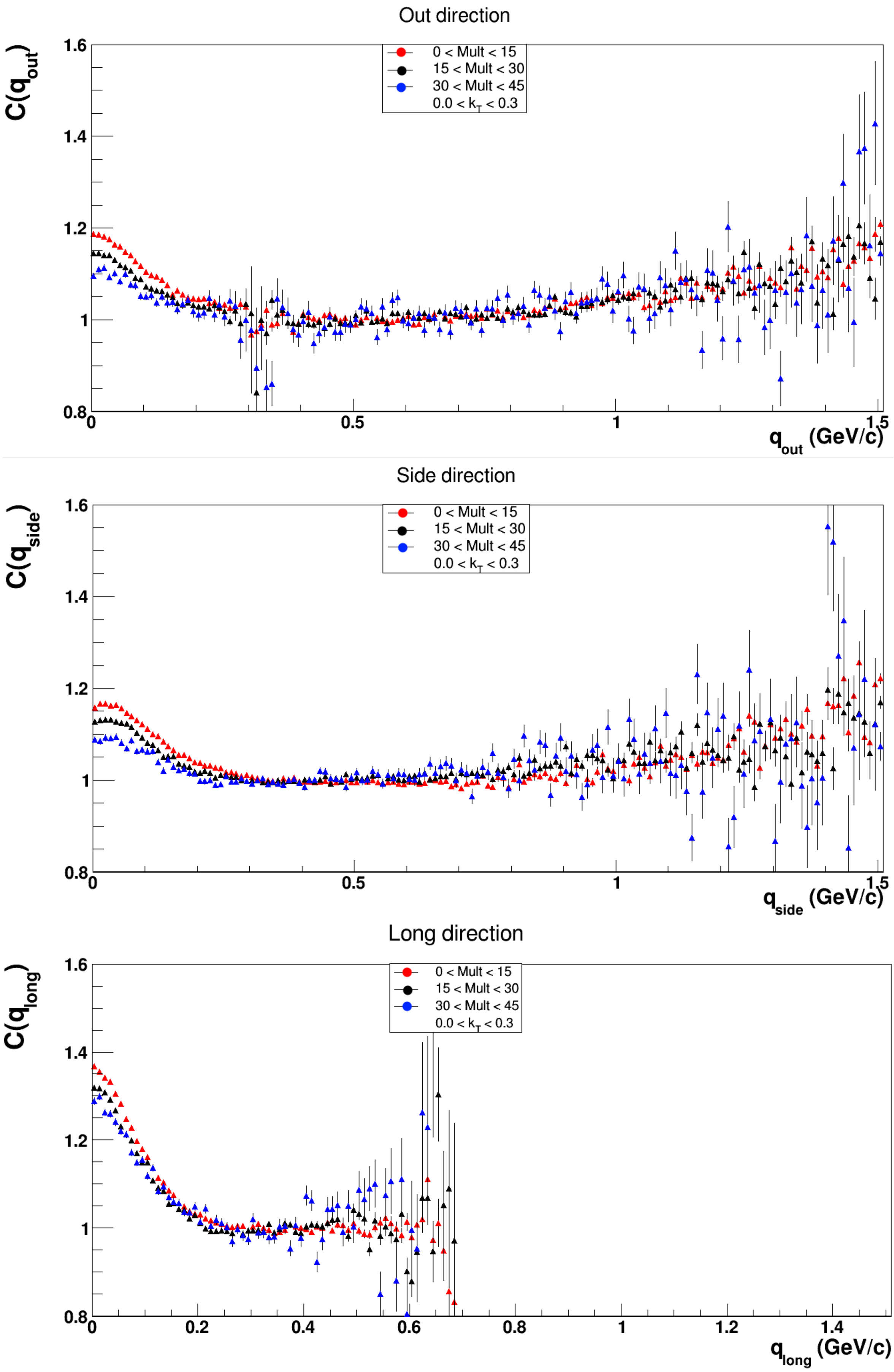

Figure 6.22: The multiplicity dependence of 3-dimensional correlation functions for the positive charged pions $0.0 < k_T < 0.3$.

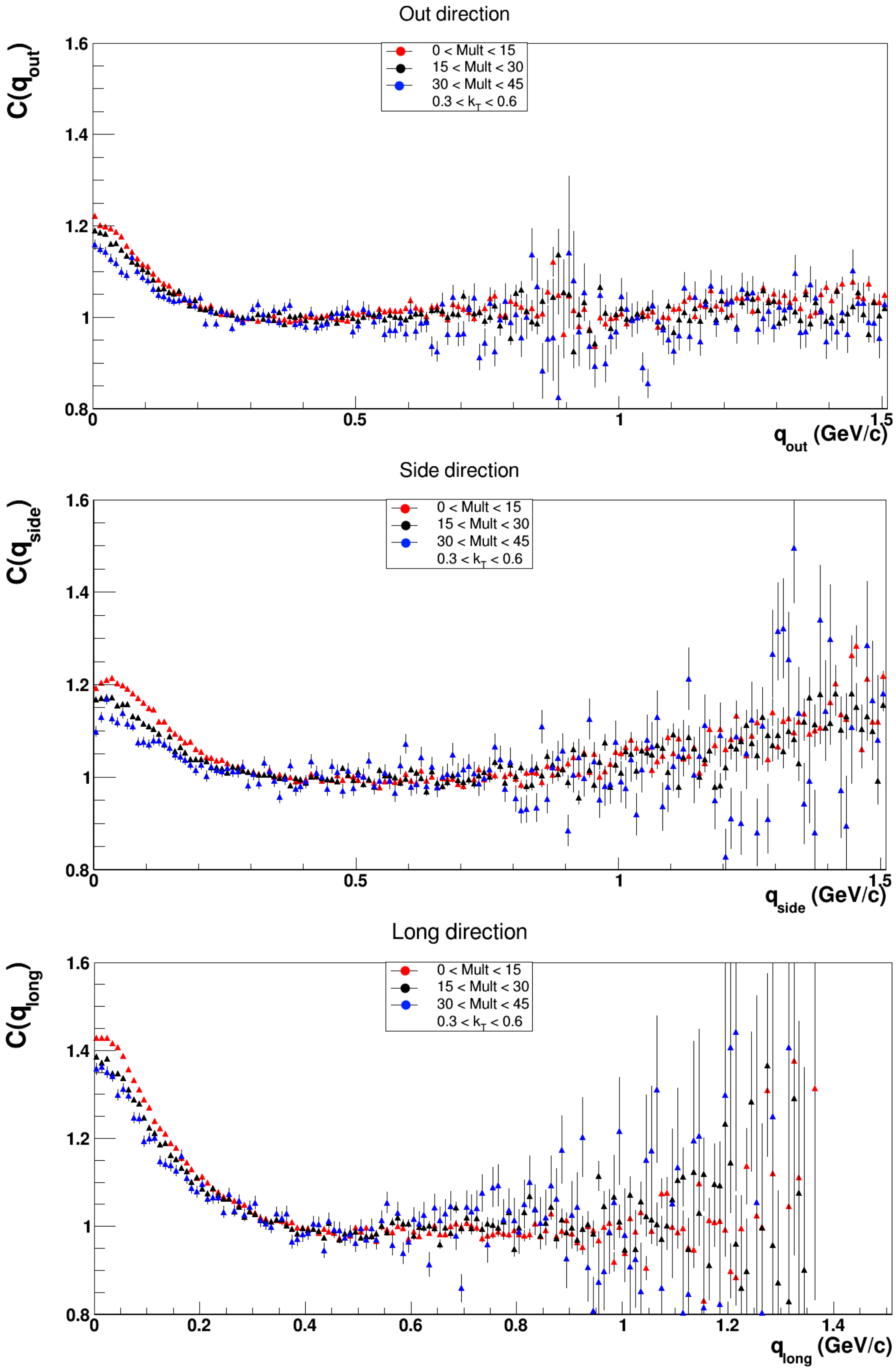

Figure 6.23: The multiplicity dependence of 3-dimensional correlation functions for the positive charged pions for $0.3 < k_T < 0.6$.

Chapter 7

Conclusion

The main goal of this work was to perform an analysis of the femtoscopic study of two-particle correlations for identical positive and negative charged pions from minimum bias $p+Au$ collisions at $\sqrt{s_{NN}} = 200\,GeV$ collected by the STAR experiment.

Applying the selected criteria, the 1-dimensional correlation functions for pairs of identical pions were extracted. Functions were constructed for three multiplicity and four average pair transverse momenta (k_T) bins. In these correlation functions clear k_T and multiplicity dependencies has been observed.

For the extraction of the HBT parameters in 1-dimensional case three approaches were used. In the first one we used two simple models of the correlation functions, namely Gauss and Levy correlation functions that did not include the Coulomb interaction. Extracted HBT radii were measured as a function of k_T and multiplicity. From the results one can see clear dependence of scale parameters R_L and R_{inv} on k_T. Interestingly, the dependence of these parameters on the multiplicity is not very strong. Levy α parameter does not show any dependence on the k_T and multiplicity. Its values for different k_T and multiplicity bins lay in range $\sim 0.9-1.6$. In the second case we used the same fitting models as in the previous case. However, fitting ranges for different k_T and multiplicity bins were chosen trying to minimize the non-femtoscopic effects. From the extracted scale parameters R_L and R_{inv} we can observed the same behavior as in the previous case. However, the behavior of the α parameter changed a significantly. We can observed that the this parameter became almost constant ($\sim 1.2 - 1.4$). The fact that the α parameter is not equal to 2 indicates that the source is of non-Gaussian shape. In the third case a model based on the Gaussian distribution and including include the Coulomb interaction was applied. However, this model fails to describe the data especially for the smaller sources at higher k_T. This failure of this model can be caused by non-femtoscopic effects and non-Gaussian shape of the source. In all the three ways mentioned above the λ parameter shows the same non-monotonic behavior.

In 3-dimensional analysis we extracted correlation functions in the longitudinally co-moving frame. Here we showed that multiplicity and k_T dependence of these functions can be observed. However, the extraction of the HBT parameters is complicated because the non-femtoscopic effects influence our functions significantly. In near future it is planned to study the 3-dimensional correlations function with the use of decomposition into spherical harmonics.

Chapter 8

Appendices

8.1 Appendix A

We have the shape of the correlation function in the form

$$C_F(\vec{q},\vec{k}) = 1 \pm \int cos(x^\sigma q_\sigma) d(x^\mu, k^\mu) d^4 x_\mu. \tag{8.1}$$

Dot product of the four-momenta q^μ and x^μ is defined as

$$q \cdot x = q^\mu x_\mu = q_0 x_0 - \vec{q} \cdot \vec{x} \tag{8.2}$$

Using this for product and Mass-shell constraint, $q_0 = \vec{\beta} \cdot \vec{q}$ in 8.1 we can write

$$\begin{aligned} C_F(\vec{q},\vec{k}) &= 1 \pm \int cos(x_0 q_0 - \vec{x} \cdot \vec{q}) d(x^\mu, k^\mu) d^4 x_\mu \\ &= 1 \pm \int cos(\vec{\beta} \cdot \vec{q} t - \vec{x} \cdot \vec{q}) \int d(\vec{x}, t, k^\mu) dt d\vec{x} \\ &= 1 \pm \int cos[(\vec{\beta} t - \vec{x}) \cdot \vec{q}] \int d(\vec{x}, t, k^\mu) dt d\vec{x}. \end{aligned} \tag{8.3}$$

Utilizing of the fact that cosine is even function $cos(x) = cos(-x)$, we can write

$$C_F(\vec{q},\vec{k}) = 1 \pm \int cos[(\vec{x} - \vec{\beta} t) \cdot \vec{q}] \int d(\vec{x}, t, k^\mu) dt d\vec{x} \tag{8.4}$$

Now we use simple substitution

$$\vec{r} = \vec{x} - \vec{\beta} t \rightarrow \vec{x} = \vec{r} + \vec{\beta} t \ \rightarrow d\vec{x} = d\vec{r} \tag{8.5}$$

Using this substitution we can rewrite out correlation function

$$C_F(\vec{q},\vec{k}) = 1 \pm \int cos(\vec{r} \cdot \vec{q}) \int d(\vec{r} + \vec{\beta} t, t, k^\mu) dt d\vec{r}. \tag{8.6}$$

From the On-shell approximation we know that $k_0 = \sqrt{m^2 + \vec{k}^2}$, therefore we can write

$$S_{\vec{k}}(\vec{x}) = \int d(\vec{r} + \vec{\beta} t, t, k_0, \vec{k}) dt, \tag{8.7}$$

and finally we can write down the right hand side of the equation 5.17

$$C_F(\vec{q},\vec{k}) = 1 \pm \int cos(\vec{r}\cdot\vec{q})S_{\vec{k}}(\vec{r})d\vec{r}, \tag{8.8}$$

where function $S_{\vec{k}}(\vec{r})$ is Relative source function.

8.2 Appendix B

We will start with the general shape of the correlation function

$$\begin{aligned} C_F(\vec{q},\vec{k}) &= \frac{P(\vec{p_1})P(\vec{p_2}) \pm \int d^4x_{1\mu}d^4x_{2\nu}S(x_1^\mu,p_1^\mu)S(x_2^\nu,p_2^\nu)cos((p_1-p_2)^\sigma(x_1-x_2)_\sigma)}{P(\vec{p_1})P(\vec{p_2})} \\ &= 1 \pm \frac{\int d^4x_{1\mu}d^4x_{2\nu}S(x_1^\mu,p_1^\mu)S(x_2^\nu,p_2^\nu)cos((p_1-p_2)^\sigma(x_1-x_2)_\sigma)}{\int d^4x_{1\mu}d^4x_{2\nu}S(x_1^\mu,p_1^\mu)S(x_2^\nu,p_2^\nu)}. \end{aligned} \tag{8.9}$$

In the following step we utilize Smoothness approximation ($p_1^\mu \approx p_2^\mu \approx k^\mu$), definition of the relative momentum $q^\mu = (p_1 - p_2)^\mu$ and a fact that the cosine function can be rewrited through the exponential function ($e^{ix} = cos(x) + isin(x)$), where we will keep in mind that we use only real part of the exponential function.

$$\begin{aligned} C_F(\vec{q},\vec{k}) &= 1 \pm \frac{\int d^4x_{1\mu}d^4x_{2\nu}S(x_1^\mu,k^\mu)S(x_2^\nu,k^\nu)e^{(q^\sigma(x_1-x_2)_\sigma)}}{\int S(x_1^\mu,k_1^\mu)d^4x_{1\mu}\int S(x_2^\nu,k_2^\nu)d^4x_{2\nu}} \\ &= 1 \pm \frac{(\int d^4x_{1\mu}S(x_1^\mu,k^\mu)e^{iq^\sigma x_{\sigma 1}})(\int d^4x_{1\nu}S(x_1^\nu,k^\nu)e^{-iq^\sigma x_{\sigma 2}})}{\left|\int S(x_1^\mu,k_1^\mu)d^4x_{1\mu}\right|^2} \end{aligned} \tag{8.10}$$

Since the interesting region of the correlation function is situated at very small q^μ, we will decompose the correlation function around point $q^\mu = 0$ to the second degree of Taylor series.

The first derivation

$$\begin{aligned} \frac{d(C_F(\vec{q},\vec{k})-1)}{dq^\alpha}\Big|_{q^\alpha=0} &= \frac{d}{dq^\alpha}\Big[\frac{(\int d^4x_{1\mu}S(x_1^\mu,k^\mu)e^{iq^\sigma x_{\sigma 1}})(\int d^4x_{1\nu}S(x_1^\nu,k^\nu)e^{-iq^\sigma x_{\sigma 2}})}{\left|\int S(x_1^\mu,p_1^\mu)d^4x_{1\mu}\right|^2}\Big]_{q^\alpha=0} \\ &= \Big\{\Big[\frac{(i\int d^4x_{1\mu}x_1^\alpha S(x_1^\mu,k^\mu)e^{iq^\sigma x_{\sigma 1}})(\int d^4x_{2\nu}S(x_2^\nu,k^\nu)e^{-iq^\sigma x_{\sigma 2}})}{\left|\int S(x_1^\mu,p_1^\mu)d^4x_{1\mu}\right|^2}\Big] \\ &-\Big[\frac{(\int d^4x_{1\mu}S(x_1^\mu,k^\mu)e^{iq^\sigma x_{\sigma 1}})(i\int d^4x_{2\nu}x_2^\alpha S(x_2^\nu,k^\nu)e^{-iq^\sigma x_{\sigma 2}})}{\left|\int S(x_1^\mu,k_1^\mu)d^4x_{1\mu}\right|^2}\Big]\Big\}_{q^\alpha=0} = 0 \end{aligned} \tag{8.11}$$

The second derivation

$$\begin{aligned} \frac{d(C_F(\vec{q},\vec{k})-1)}{dq^\beta dq^\alpha}\Big|_{q^\beta=q^\alpha=0} &= -2\Big\{\frac{(\int d^4x_{1\mu}S(x_1^\mu,k^\mu)x_1^\alpha x_1^\beta)(\int d^4x_{2\nu}S(x_2^\nu,k^\nu))}{\left|\int S(x_1^\mu,k_1^\mu)d^4x_{1\mu}\right|^2}+ \\ &\frac{(\int d^4x_{1\mu}S(x_1^\mu,k^\mu)x_1^\alpha)(\int d^4x_{2\nu}S(x_2^\nu,k^\nu)x_2^\beta)}{\left|\int S(x_1^\mu,k_1^\mu)d^4x_{1\mu}\right|^2}\Big\}. \end{aligned} \tag{8.12}$$

Using relation which represents average with the emission function

$$\langle f \rangle = \frac{\int d^4x_\mu f(x^\mu) S(x^\mu, k^\mu)}{\int d^4x_\mu S(x^\mu, k^\mu)}, \tag{8.13}$$

with using this average formula we can rewrite the second derivation as follow

$$\frac{d(C_F(\vec{q}, \vec{k}) - 1)}{dq^\beta dq^\alpha}\Big|_{q^\beta = q^\alpha = 0} = -2[\langle x^\alpha x^\beta \rangle - \langle x^\alpha \rangle \langle x^\beta \rangle] = -2\langle \tilde{x}^\alpha \tilde{x}^\beta \rangle, \tag{8.14}$$

where we utilized notation $\tilde{x_\mu} = x_\mu - \langle x_\mu \rangle$. In equation 5.18 we parametrized our correlation function with Gaussian

$$C(\vec{q}, \vec{k}) = 1 \pm e^{-q^\mu q^\nu B_{\mu\nu}}. \tag{8.15}$$

Now, when we do Taylor series of $(C_F(\vec{q}, \vec{k}) - 1$ to the second degree

$$C(\vec{q}, \vec{k}) - 1 = \frac{(\int d^4x_{1\mu} S(x_1^\mu, k^\mu) e^{iq^\sigma x_{\sigma 1}})(\int d^4x_{1\nu} S(x_1^\nu, k^\nu) e^{-iq^\sigma x_{\sigma 2}})}{\left| \int S(x_1^\mu, k_1^\mu) d^4x_{1\mu} \right|^2} \approx 1 - \frac{1}{2!} q_\mu q_\nu 2 \langle \tilde{x}^\mu \tilde{x}^\nu \rangle, \tag{8.16}$$

and when we compare the second degree of Taylor series of equation 8.15 and equation 8.16, we can see that

$$B_{\mu\nu} = \langle \tilde{x}_\mu \tilde{x}_\nu \rangle. \tag{8.17}$$

8.3 Appendix C

To reach a general form of HBT radii we will utilize exponent of the equation 5.20, where $\mu, \nu = 0, 1, 2, 3$

$$\begin{gathered}
q_\mu q_\nu \langle \tilde{x}^\mu \tilde{x}^\nu \rangle = \\
q_0 q_0 \langle \tilde{x}^0 \tilde{x}^0 \rangle - q_0 q_1 \langle \tilde{x}^0 \tilde{x}^1 \rangle - q_0 q_2 \langle \tilde{x}^0 \tilde{x}^2 \rangle - q_0 q_3 \langle \tilde{x}^0 \tilde{x}^3 \rangle - \\
q_1 q_0 \langle \tilde{x}^1 \tilde{x}^0 \rangle + q_1 q_1 \langle \tilde{x}^1 \tilde{x}^1 \rangle + q_1 q_2 \langle \tilde{x}^1 \tilde{x}^2 \rangle + q_1 q_3 \langle \tilde{x}^1 \tilde{x}^3 \rangle - \\
q_2 q_0 \langle \tilde{x}^2 \tilde{x}^0 \rangle + q_2 q_1 \langle \tilde{x}^2 \tilde{x}^1 \rangle + q_2 q_2 \langle \tilde{x}^2 \tilde{x}^2 \rangle + q_2 q_3 \langle \tilde{x}^2 \tilde{x}^3 \rangle - \\
q_3 q_0 \langle \tilde{x}^3 \tilde{x}^0 \rangle + q_3 q_1 \langle \tilde{x}^3 \tilde{x}^1 \rangle + q_3 q_2 \langle \tilde{x}^3 \tilde{x}^2 \rangle + q_3 q_3 \langle \tilde{x}^3 \tilde{x}^3 \rangle = \\
q_0 q_0 \langle \tilde{x}^0 \tilde{x}^0 \rangle + q_1 q_1 \langle \tilde{x}^1 \tilde{x}^1 \rangle + q_2 q_2 \langle \tilde{x}^2 \tilde{x}^2 \rangle + q_4 q_4 \langle \tilde{x}^4 \tilde{x}^4 \rangle - \\
2q_0 q_1 \langle \tilde{x}^0 \tilde{x}^1 \rangle - 2q_0 q_2 \langle \tilde{x}^0 \tilde{x}^2 \rangle - 2q_0 q_3 \langle \tilde{x}^0 \tilde{x}^3 \rangle + \\
2q_1 q_2 \langle \tilde{x}^1 \tilde{x}^2 \rangle + 2q_1 q_3 \langle \tilde{x}^1 \tilde{x}^3 \rangle + 2q_2 q_3 \langle \tilde{x}^2 \tilde{x}^3 \rangle
\end{gathered} \tag{8.18}$$

Next we utilize

$$\begin{gathered}
q_\mu = (q_0, \vec{q}) \qquad \vec{q} = (q_o, q_s, q_l) \\
\vec{k} = (k_T, 0, k_l) = (\beta_o, \beta_s \beta_l) \\
q_0 = \vec{\beta} \vec{q}
\end{gathered} \tag{8.19}$$

so now we can edit four-momenta with vectors 8.19 above

$$
\begin{aligned}
q_1q_2 = q_oq_l, \quad q_1q_3 = q_oq_l, \quad q_2q_3 = q_sq_l, \\
q_1q_1 = q_0^2, \quad q_2q_2 = q_s^2, \quad q_3q_3 = q_l^2, \\
q_0q_0 = (\beta_oq_o + \beta_lq_l)^2, \\
q_0q_1 = (\beta_oq_o + \beta_lq_l)q_o, \\
q_0q_2 = (\beta_oq_o + \beta_lq_l)q_s, \\
q_0q_3 = (\beta_oq_o + \beta_lq_l)q_l.
\end{aligned} \tag{8.20}
$$

Substituting relation 8.20 to the equation 8.18 we get

$$
\begin{aligned}
q_\mu q_\nu\langle\tilde{x}^\mu\tilde{x}^\nu\rangle = (\beta_oq_o + \beta_lq_l)^2\langle\tilde{x}^0\tilde{x}^0\rangle - 2(\beta_oq_o + \beta_lq_l)q_o\langle\tilde{x}^0\tilde{x}^1\rangle \\
-2(\beta_oq_o + \beta_lq_l)q_s\langle\tilde{x}^0\tilde{x}^2\rangle - 2(\beta_oq_o + \beta_lq_l)q_l\langle\tilde{x}^0\tilde{x}^3\rangle \\
+2q_oq_s\langle\tilde{x}^1\tilde{x}^2\rangle + 2q_oq_l\langle\tilde{x}^1\tilde{x}^3\rangle + 2q_sq_l\langle\tilde{x}^2\tilde{x}^3\rangle + \\
q_o^2\langle\tilde{x}^1\tilde{x}^1\rangle + q_s^2\langle\tilde{x}^2\tilde{x}^2\rangle + q_l^2\langle\tilde{x}^3\tilde{x}^3\rangle
\end{aligned} \tag{8.21}
$$

In the final step we sum all terms corresponding to the certain momentum

$$
\begin{aligned}
q_o^2 : \beta_o^2\langle\tilde{x}^0\tilde{x}^0\rangle - 2\beta_o\langle\tilde{x}^0\tilde{x}^1\rangle + \langle\tilde{x}^1\tilde{x}^1\rangle = \langle(\tilde{x}^1 - \beta_o\tilde{x}^0)^2\rangle \\
q_l^2 : \beta_l^2\langle\tilde{x}^0\tilde{x}^0\rangle - 2\beta_l\langle\tilde{x}^0\tilde{x}^3\rangle + \langle\tilde{x}^3\tilde{x}^3\rangle = \langle(\tilde{x}^3 - \beta_l\tilde{x}^0)^2\rangle \\
q_s^2 : \langle\tilde{x}^2\tilde{x}^2\rangle \\
q_oq_s : 2\langle\tilde{x}^1\tilde{x}^2\rangle - 2\beta_o\langle\tilde{x}^0\tilde{x}^2\rangle = 2\langle(\tilde{x}^1 - \beta_o\tilde{x}^0)\tilde{x}^2\rangle \\
q_sq_l : 2\langle\tilde{x}^2\tilde{x}^3\rangle - 2\beta_l\langle\tilde{x}^0\tilde{x}^2\rangle = 2\langle(\tilde{x}^3 - \beta_l\tilde{x}^0)\tilde{x}^2\rangle \\
q_lq_o : 2\beta_o\beta_l\langle\tilde{x}^0\tilde{x}^0\rangle - 2\beta_l\langle\tilde{x}^0\tilde{x}^1\rangle + 2\langle\tilde{x}^1\tilde{x}^3\rangle - 2\beta_o\langle\tilde{x}^0\tilde{x}^3\rangle = \\
2\langle(\tilde{x^1} - \beta_o\tilde{x^0})(\tilde{x^3} - \beta_l\tilde{x^0})\rangle
\end{aligned} \tag{8.22}
$$

One then finds that the HBT radius parameters measure different combinations of the spatial and temporal extent of the collision system

$$R_o^2 = \langle(\tilde{x}_o - \beta_o\tilde{t})^2\rangle \tag{8.23}$$

$$R_s^2 = \langle\tilde{x}_s^2\rangle \tag{8.24}$$

$$R_l^2 = \langle(\tilde{x}_l - \beta_l\tilde{t})^2\rangle \tag{8.25}$$

$$R_{os}^2 = 2\langle(\tilde{x}_o - \beta_o\tilde{t})\tilde{x}_s\rangle \tag{8.26}$$

$$R_{ol}^2 = 2\langle(\tilde{x}_o - \beta_o\tilde{t})(\tilde{x}_l - \beta_l\tilde{t})\rangle \tag{8.27}$$

$$R_{sl}^2 = 2\langle(\tilde{x}_l - \beta_l\tilde{t})\tilde{x}_s\rangle. \tag{8.28}$$

For expression 8.23-8.28 we can also use quite different notation where $\tilde{x} = \tilde{x}_o$, $\tilde{y} = \tilde{x}_s$ and $\tilde{z} = \tilde{x}_l$.

8.4 Appendix D

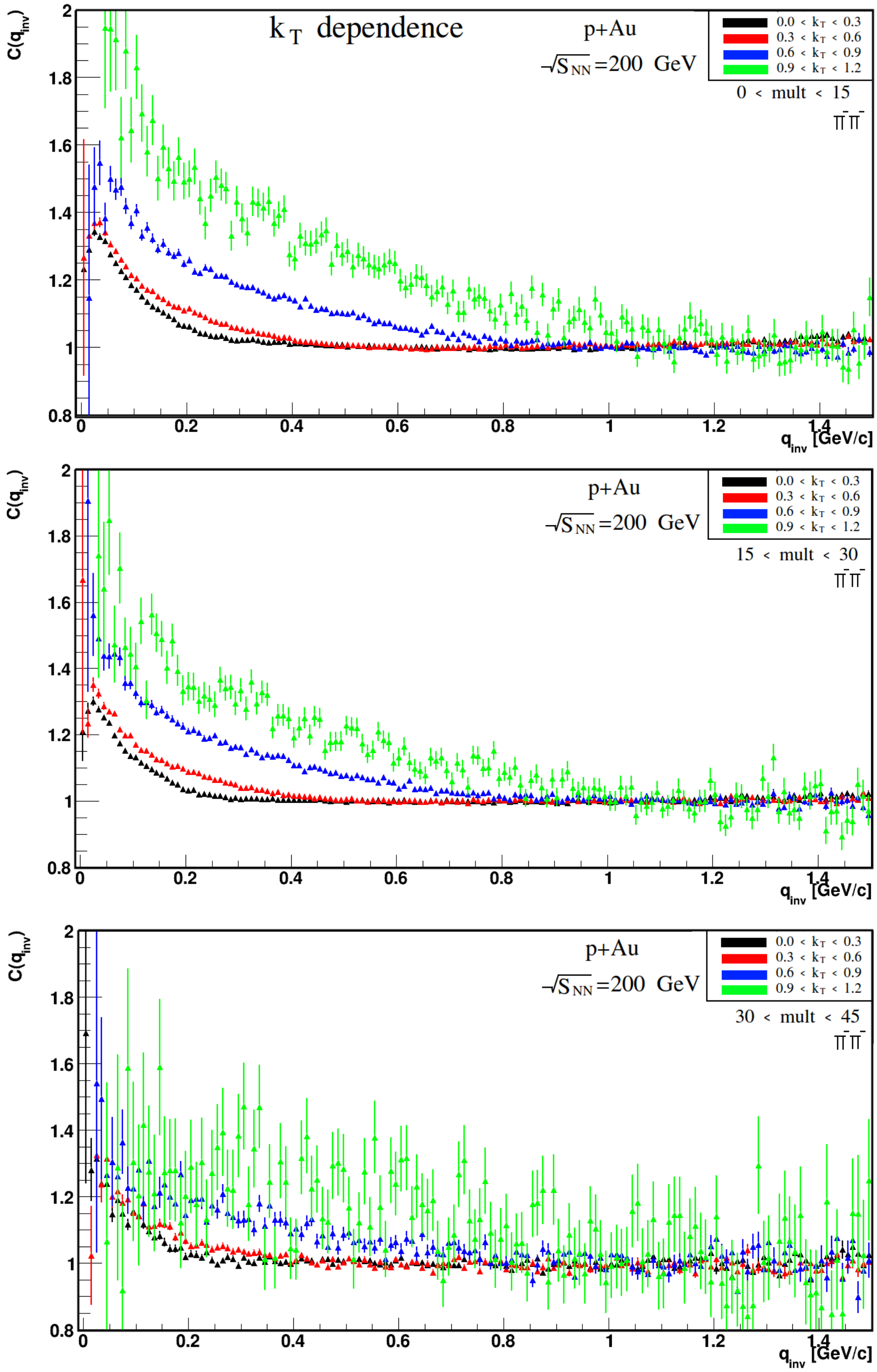

Figure 8.1: 1-dimensional correlation functions for the negative charge pions for 4 k_T bins and 3 multiplicity bins.

The fits of the correlation functions for the multiplicity range $15-30$ (Fig.8.2) and $30-45$ (Fig.8.3) for positive pions where fits were performed up to $1.5\,GeV/c$.

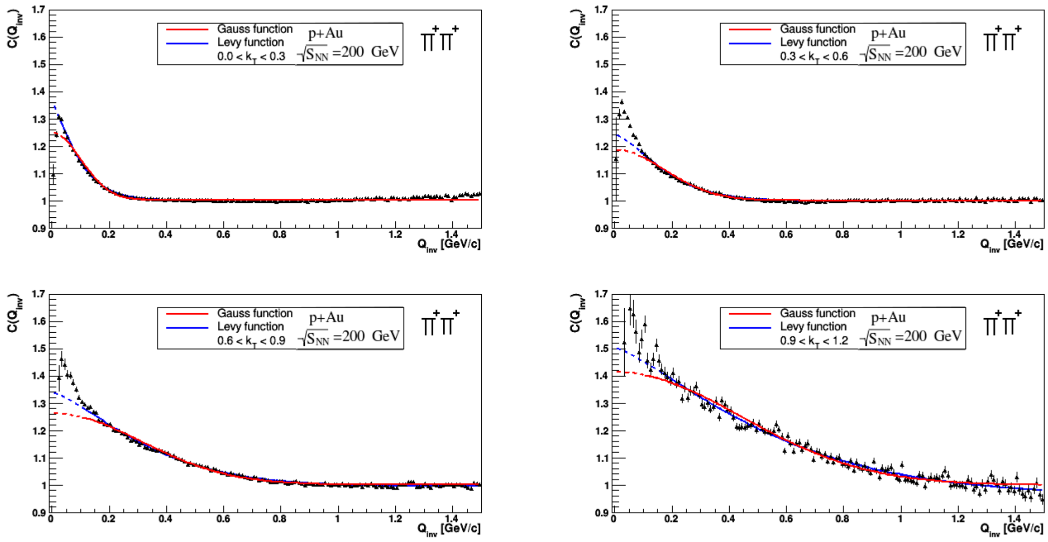

Figure 8.2: Correlation functions for the positive pion in multiplicity range $15-30$ for 4 different k_T bins.

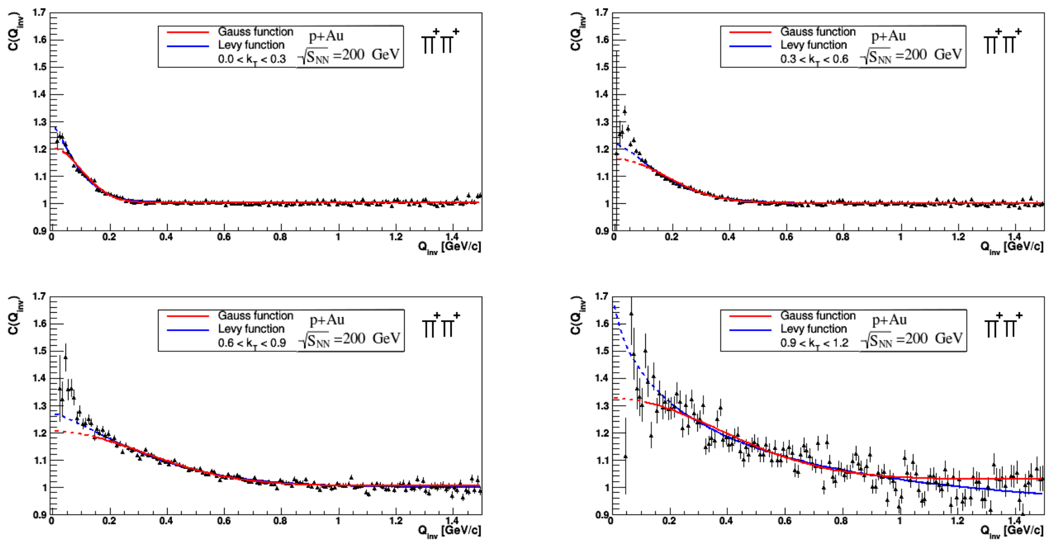

Figure 8.3: Correlation functions for the positive pion in multiplicity range $30-45$ for 4 different k_T bins.

The fits of the correlation functions for the multiplicity range $0-15$ (Fig.8.4), $15-30$ (Fig.8.5) and $30-45$ (Fig.8.6) for negative pions where fits were performed up to $1.5\,GeV/c$.

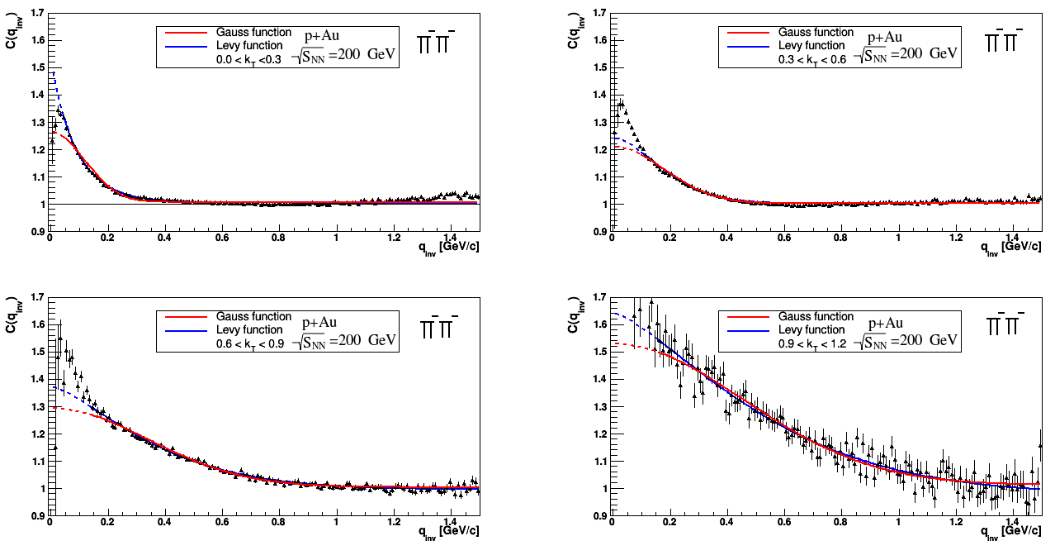

Figure 8.4: Correlation functions for the negative pion in multiplicity range $0-15$ for 4 different k_T bins.

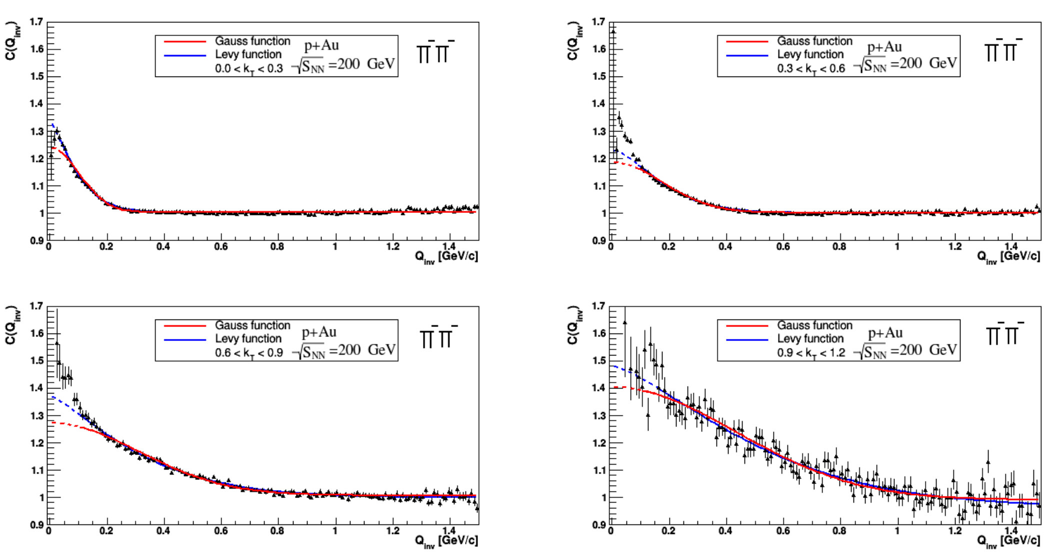

Figure 8.5: Correlation functions for the negative pion in multiplicity range $15-30$ for 4 different k_T bins.

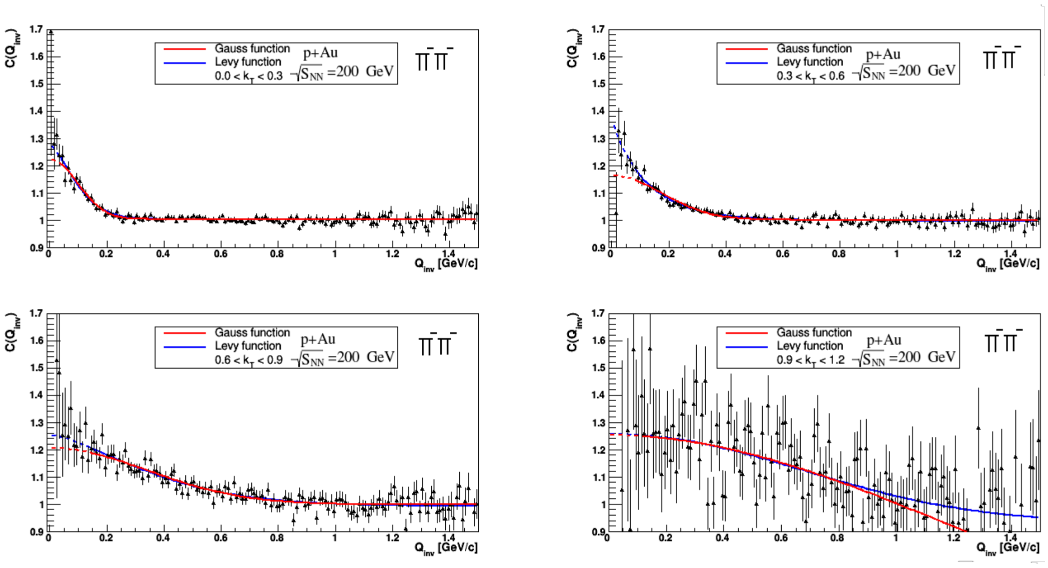

Figure 8.6: Correlation functions for the negative pion in multiplicity range $30-45$ for 4 different k_T bins.

The fits of the correlation functions for the multiplicity range $15-30$ (Fig.8.7) and $30-45$ (Fig.8.8) for positive pions. These fits were performed for different fitting ranges for each multiplicity and k_T bin.

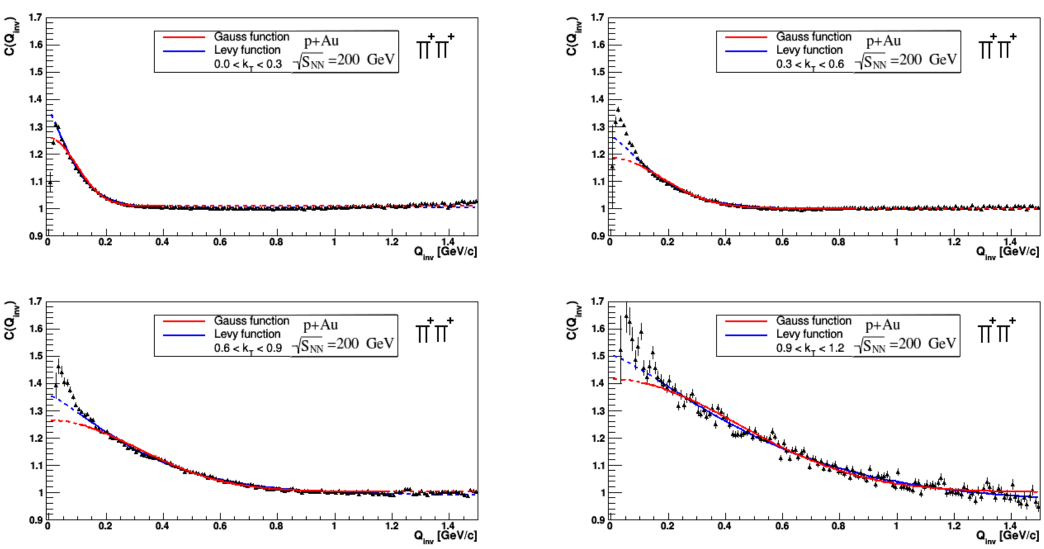

Figure 8.7: Correlation functions for the positive pion in multiplicity range $15-30$ for 4 different k_T bins.

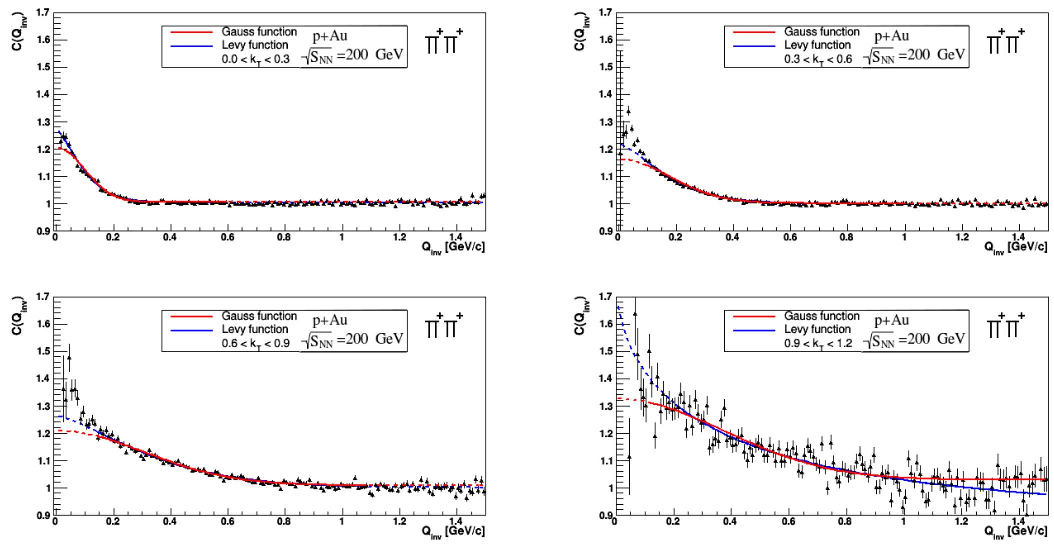

=

Figure 8.8: Correlation functions for the positive pion in multiplicity range $30-45$ for 4 different k_T bins.

The fits of the correlation functions for the multiplicity range $0-15$ (Fig.8.9), $15-30$ (Fig.8.10) and $30-45$ (Fig.8.11) for negative pions where fits were performed for different fitting ranges for each multiplicity and k_T bin.

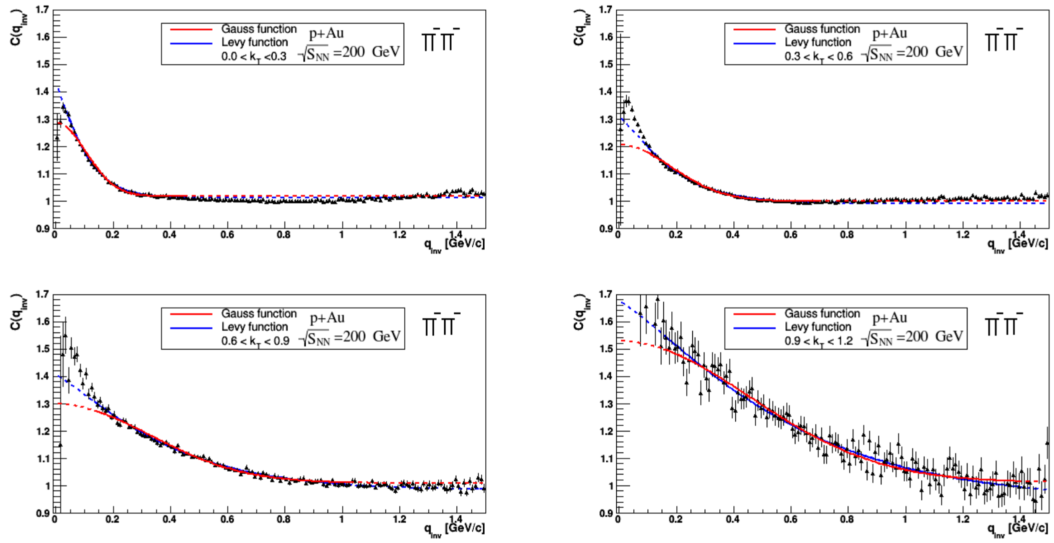

Figure 8.9: Correlation functions for the negative pion in multiplicity range $0-15$ for 4 different k_T bins.

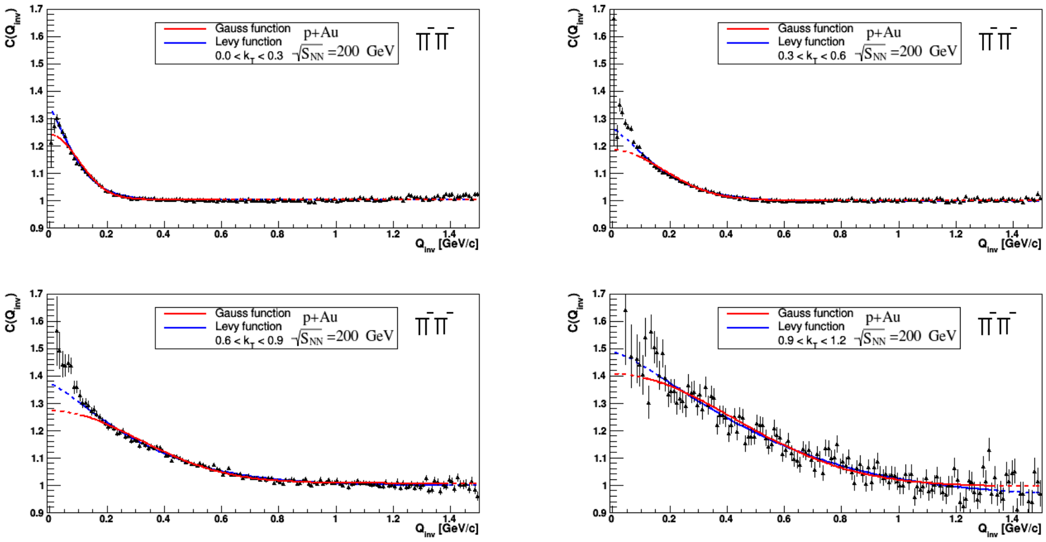

Figure 8.10: Correlation functions for the negative pion in multiplicity range $15-30$ for 4 different k_T bins.

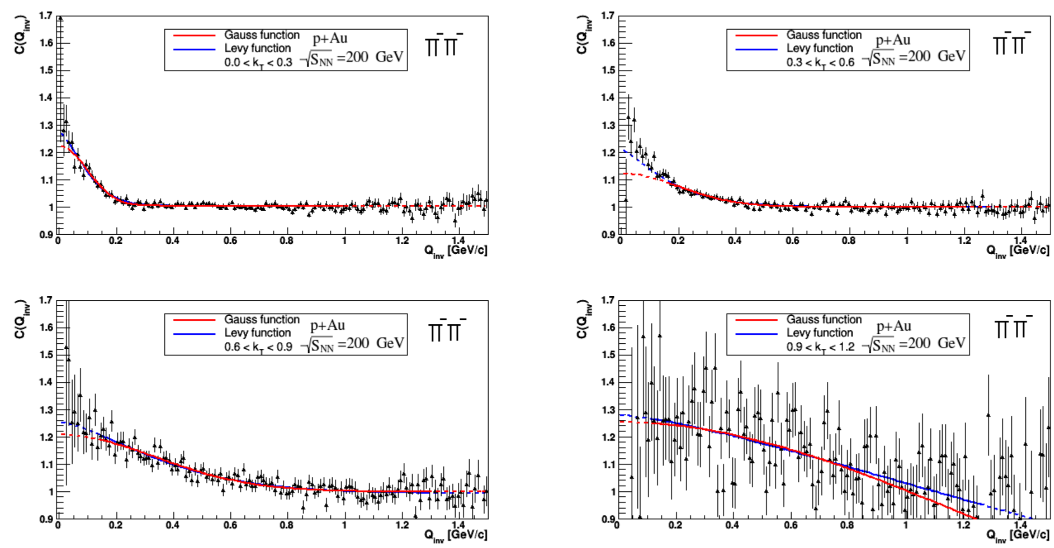

Figure 8.11: Correlation functions for the negative pion in multiplicity range $30-45$ for 4 different k_T bins.

The fits of the correlation functions for the multiplicity range $15-30$ (Fig.8.12) and $30-45$ (Fig.8.13) for the pair of positive pions. These fits were performed for whole k_T including Coulomb interaction.

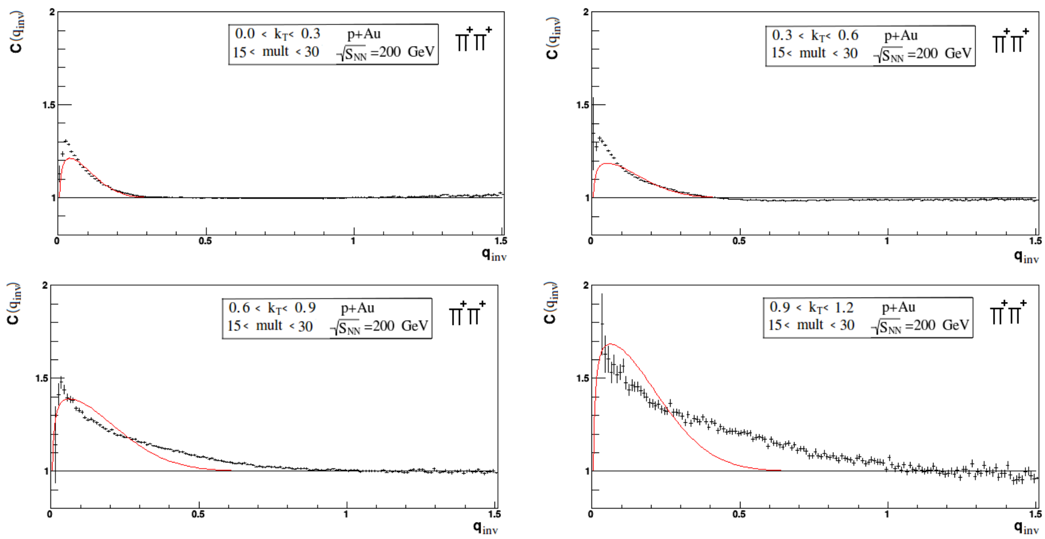

Figure 8.12: Correlation functions for the positive pion in multiplicity range $15-30$ for 4 different k_T bins.

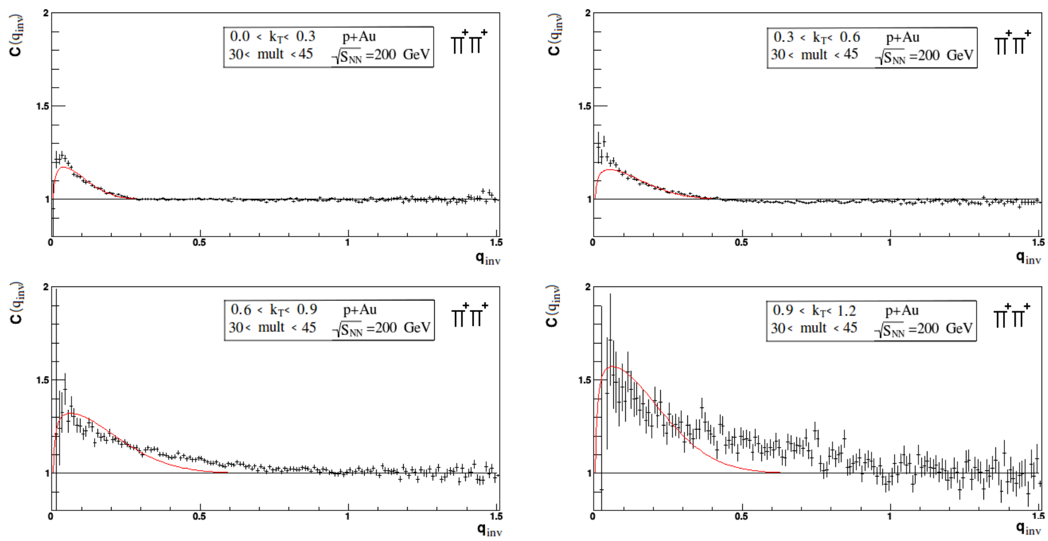

Figure 8.13: Correlation functions for the positive pion in multiplicity range $30-45$ for 4 different k_T bins.

The fits of the correlation functions for the multiplicity range $0 - 15$ (Fig.8.14), $15 - 30$ (Fig.8.15) and $30 - 45$ (Fig.8.16) for negative pions where fits were performed for whole k_T including Coulomb interaction.

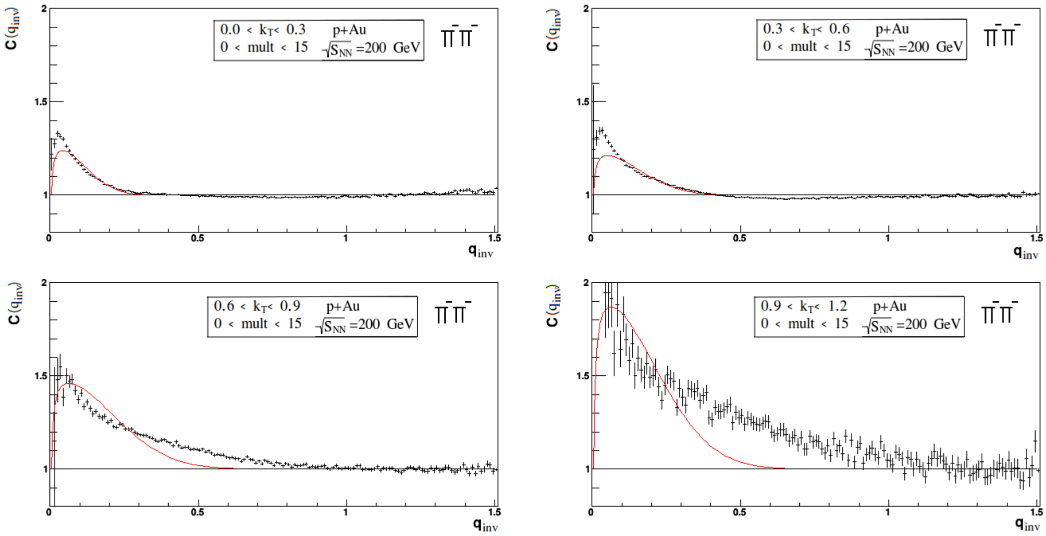

Figure 8.14: Correlation functions for the negative pion in multiplicity range $0-15$ for 4 different k_T bins.

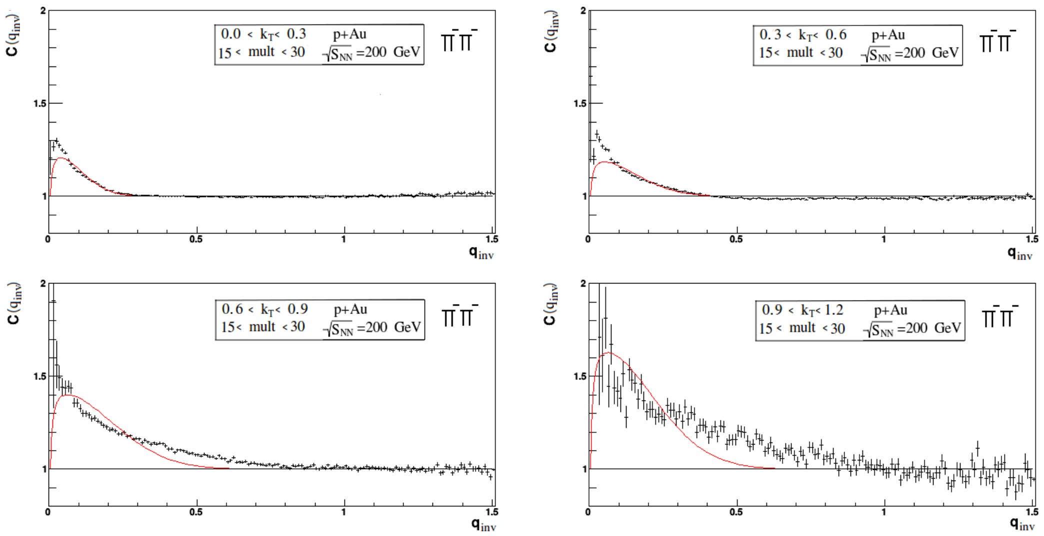

Figure 8.15: Correlation functions for the negative pion in multiplicity range $15 - 30$ for 4 different k_T bins.

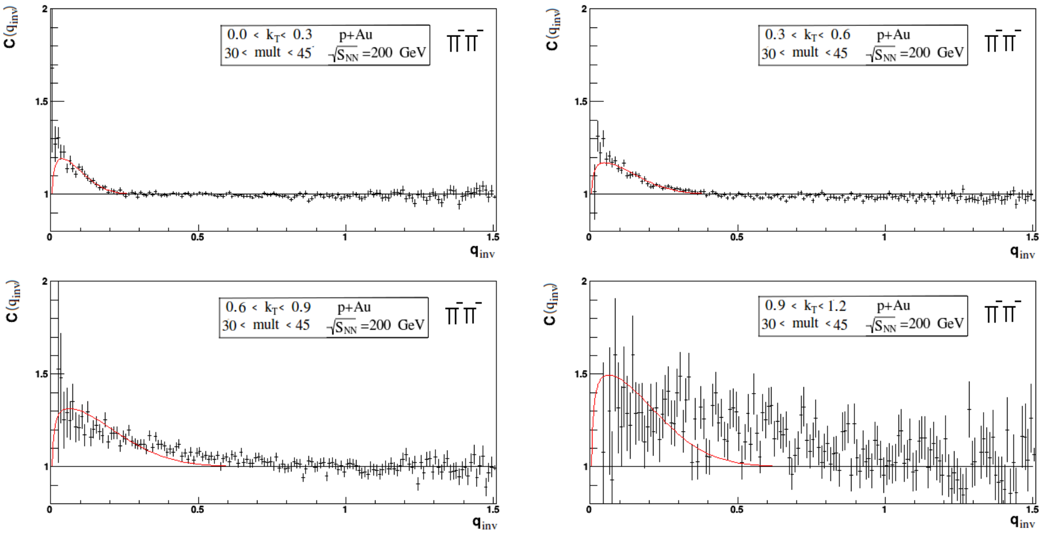

Figure 8.16: Correlation functions for the negative pion in multiplicity range $30 - 45$ for 4 different k_T bins.

Bibliography

[1] A Modern Indroduction to Nuclear Physics. http://www.physics.umd.edu/courses/Phys741/xji/chapter1.pdf. Accessed: 2017-04-4.

[2] Asymptotic Freedom and the Coupling Constant of QCD. http://backreaction.blogspot.cz/2007/12/asymptotic-freedom-and-coupling.html. Accessed: 2017-04-3.

[3] Brookhaven National Laboratory. Laboratory, brookhaven national. http://www.star.bnl.gov. Accessed: 2017-04-23.

[4] Conceptual design report. https://drupal.star.bnl.gov/STAR/files/StarCDR.pdf. Accessed: 2017-04-23.

[5] Evolution of collisions and QGP. https://particlesandfriends.wordpress.com/2016/10/14/evolution-of-collisions-and-qgp/. Accessed: 2017-04-10.

[6] Experimental test of Asymptotic Freedom. arxiv.org/pdf/hep-ex/0606035. 2006-06-15.

[7] Fundamental Forces and Yukawa Theory. http://cronodon.com/Atomic/Fundamental_Forces.html. Accessed: 2017-04-1.

[8] How Low Can RHIC Go? https://www.bnl.gov/rhic/news2/news.asp?a=1870&t=today. Accessed: 2017-04-6.

[9] HTRA Galway. http://slideplayer.com/slide/4823367/. Accessed: 2017-07-12.

[10] Lectures on Quantum Chromodynamics. https://www.nikhef.nl/~h71/Lectures/2015/Other/qcdlecture.pdf. Accessed: 2017-04-3.

[11] NASA gallery. https://www.nasa.gov/. Accessed: 2018-03-11.

[12] Nuclear Science and Technology - STAR experiment. https://nsww.org/projects/bnl/star/index.php. Accessed: 2018-04-18.

[13] Polarimetry. `https://wiki.bnl.gov/rhicspin/Polarimetry`. Accessed: 2017-04-15.

[14] Proposal for a Large Area Time of Flight System for STAR. `https://www.star.bnl.gov/public/tof/publications/TOF_20040524.pdf`. Accessed: 2017-04-25.

[15] Quantum Chromo Dynamics. `https://www.nikhef.nl/~h24/qcdcourse/section-6.pdf`. Accessed: 2018-04-29.

[16] Standart model. `http://www.eskesthai.com/search/label/Standard%20model`. Accessed: 2017-03-31.

[17] STAR Trigger Introduction. `http://www.star.bnl.gov/public/trg/trouble/operating-trigger/introduction/index.html#intro`. Accessed: 2018-03-11.

[18] The Standard Model. `https://home.cern`. Accessed: 2018-03-28.

[19] BI Abelev, Aggarwal, et al. Centrality dependence of charged hadron and strange hadron elliptic flow from s nn= 200 gev au+ au collisions. *Physical Review C*, 77(5):054901, 2008.

[20] BI Abelev, Aggarwal, et al. Measurements of ϕ meson production in relativistic heavy-ion collisions at the bnl relativistic heavy ion collider (rhic). *Physical Review C*, 79(6):064903, 2009.

[21] Alberto Accardi and Miklos Gyulassy. Cronin effect vs. geometrical shadowing in d+ au collisions at rhic. *Physics Letters B*, 586(3-4):244–253, 2004.

[22] L Adamczyk, Adkins, et al. Centrality and transverse momentum dependence of elliptic flow of multistrange hadrons and ϕ meson in au+ au collisions at s n n= 200 gev. *Physical review letters*, 116(6):062301, 2016.

[23] L Adamczyk, James K Adkins, Agakishiev, et al. Measurement of elliptic flow of light nuclei at 200, 62.4, 39, 27, 19.6, 11.5, and 7.7 gev at the bnl relativistic heavy ion collider. *Physical Review C*, 94(3):034908, 2016.

[24] L Adamczyk, JK Adkins, Agakishiev, et al. Bulk properties of the medium produced in relativistic heavy-ion collisions from the beam energy scan program. *Physical Review C*, 96(4):044904, 2017.

[25] L Adamczyk, JK Adkins, G Agakishiev, MM Aggarwal, Z Ahammed, NN Ajitanand, I Alekseev, DM Anderson, R Aoyama, A Aparin, et al. Measurement of d 0 azimuthal anisotropy at midrapidity in au+ au collisions at s n n= 200 gev. *Physical review letters*, 118(21):212301, 2017.

[26] L Adamczyk, STAR Collaboration, et al. Beam energy dependence of jet-quenching effects in au+ au collisions at/snn= 7.7, 11.5, 14.5, 19.6, 27, 39, and 62.4 gev. *arXiv preprint arXiv:1707.01988.*

[27] J Adams, MM Aggarwal, Ahammed, et al. Pion interferometry in au+ au collisions at 200 gev. *Physical Review C*, 71(4):044906, 2005.

[28] John Adams, Clemens Adler, Aggarwal, et al. Azimuthally sensitive hanbury brown-twiss interferometry in au+au collisions at 200 gev. *Physical review letters*, 93(1):012301, 2004.

[29] John Adams, Clemens Adler, MM Aggarwal, Z Ahammed, J Amonett, BD Anderson, M Anderson, D Arkhipkin, GS Averichev, SK Badyal, et al. Pion-kaon correlations in central a u+ a u collisions at s n n= 130 g e v. *Physical review letters*, 91(26):262302, 2003.

[30] A Adare, S Afanasiev, Aidala, et al. Comparison of the space-time extent of the emission source in d+au and au+au collisions at 200 gev. *arXiv preprint arXiv:1404.5291*, 2014.

[31] Andrew Adare, S Afanasiev, C Aidala, NN Ajitanand, Yasuyuki Akiba, H Al-Bataineh, J Alexander, K Aoki, Y Aramaki, ET Atomssa, et al. Neutral pion production with respect to centrality and reaction plane in au+ au collisions at s nn= 200 gev. *Physical Review C*, 87(3):034911, 2013.

[32] SV Akkelin and Yu M Sinyukov. Deciphering nonfemtoscopic two-pion correlations in p+ p collisions with simple analytical models. *Physical Review D*, 85(7):074023, 2012.

[33] SV Akkelin and Yu M Sinyukov. Deciphering nonfemtoscopic two-pion correlations in p+ p collisions with simple analytical models. *Physical Review D*, 85(7):074023, 2012.

[34] Guido Altarelli and Theory Unit CERN, Department of Physics. Collider physics within the standard model: a primer. *arxiv.org/pdf/1303.2842.pdf.*

[35] M Anderson, J Berkovitz, W Betts, R Bossingham, F Bieser, R Brown, M Burks, M Calderón de la Barca Sánchez, D Cebra, M Cherney, et al. The star time projection chamber: a unique tool for studying high multiplicity events at rhic. *Nuclear Instruments and Methods in Physics Research Section A: Accelerators, Spectrometers, Detectors and Associated Equipment*, 499(2-3):659–678, 2003.

[36] Christopher Daniel Anson. *Energy dependent Hanbury-Brown and Twiss interferometry and the freeze-out eccentricity of heavy ion collisions at STAR*. The Ohio State University, 2014.

[37] Rajeev S. Bhalerao. A viscous blast-wave model for relativistic heavy-ion collisions. *arXiv:1508.05878 [nucl-th]*.

[38] Hans Bichsel. A method to improve tracking and particle identification in tpcs and silicon detectors. *Nuclear Instruments and Methods in Physics Research Section A: Accelerators, Spectrometers, Detectors and Associated Equipment*, 562(1):154–197, 2006.

[39] FS Bieser, HJ Crawford, J Engelage, Eppley, et al. The star trigger. *Nuclear Instruments and Methods in Physics Research Section A: Accelerators, Spectrometers, Detectors and Associated Equipment*, 499(2):766–777, 2003.

[40] Giuseppe E Bruno, NA57 Collaboration, et al. New results from the na57 experiment. *Journal of Physics G: Nuclear and Particle Physics*, 30(8):S717, 2004.

[41] Z Chajecki, TD Gutierrez, MA Lisa, M Lopez-Noriega, et al. Aa versus pp and da: A puzzling scaling in hbt@ rhic. *arXiv preprint nucl-ex/0505009*, 2005.

[42] Zbigniew Chajecki and Mike Lisa. Global conservation laws and femtoscopy of small systems. *Physical Review C*, 78(6):064903, 2008.

[43] M.N. Chernodub. Background magnetic field stabilizes qcd string against breaking. *arXiv:1001.0570 [hep-ph]*, 2010.

[44] T Csörgő, S Hegyi, and WA Zajc. Bose-einstein correlations for levy stable source distributions. *The European Physical Journal C-Particles and Fields*, 36(1):67–78, 2004.

[45] S. S. Adler et al. Bose-einstein correlation of charged pion pairs in au+au collisions at $s_{NN} = 200$ gevs. *Phys. Rev. Lett. 93, 152302 (2004).*

[46] S. S. Adler et al. Elliptic flow of identical hadrons in au+au collisions at $s_{NN} = 200$ gevs. *Phys. Rev. Lett. 91, 182301 (2003).*

[47] S. S. Adler et al. Production of phi at midrapidity in at a center of mass energy per nucleon of 200 gev in au+au collisions at relativistic energies. *Phys. Rev. C72, 014903 (2005).*

[48] Marek Gaździcki. Entropy in nuclear collisions. *Zeitschrift für Physik C Particles and Fields*, 66(4):659–662, 1995.

[49] Marek Gaździcki. M. gaździcki and d. röhrich, z. phys. c 65, 215 (1995). *Z. Phys. C*, 65:215, 1995.

[50] V Greco, Che Ming Ko, and P Levai. Partonic coalescence in relativistic heavy ion collisions. *Physical Review C*, 68(3):034904, 2003.

[51] David J. Gross and Frank Wilczek. Ultraviolet behavior of non-abelian gauge theories. *Phys.Rev. Lett., 30:1343–1346*, 1973.

[52] Thomas D Gutierrez. Pion interferometry from pp and dau collisions at rhic. *arXiv preprint nucl-ex/0403012*, 2004.

[53] Brooke A. Haag. Characterization of au+au collisions at $s_{NN} = 200$ gev from star: from meson production in ultra-peripheral collisions to high-pt azimuthal correlations in central collisions. Dissertation thesis, Sonoma State University-2001, University of California at Davis-2003, 2009.

[54] Amaresh et al. Jaiswal. Relativistic heavy-ion collisions. *arXiv:1404.3294 [nucl-th].*

[55] Frithjof Karsch. Lattice results on qcd thermodynamics. *arXiv preprint hep-ph/0103314*, 2001.

[56] Adam Kisiel, Fabrice Retiere, and P Szarwas. Non-identical particle correlations in star as a probe of emission asymmetries and radial flow. *Acta Phys. Polon.*, 35:47–53, 2004.

[57] R Lednicky, S Panitkin, and Nu Xu. Search for delays between unlike particle emissions in relativistic heavy-ion collisions. *arXiv preprint nucl-th/0304062*, 2003.

[58] Jindřich Lidrych. Non-identical kaon femtoscopy at star experiment. diploma thesis, CZECH TECHNICAL UNIVERSITY IN PRAGUE, 2016.

[59] Michael Annan Lisa, Scott Pratt, Ron Soltz, and Urs Wiedemann. Femtoscopy in relativistic heavy ion collisions: two decades of progress. *Annu. Rev. Nucl. Part. Sci.*, 55:357–402, 2005.

[60] WJ Llope, J Zhou, T Nussbaum, Hoffmann, et al. The star vertex position detector. *Nuclear Instruments and Methods in Physics Research Section A: Accelerators, Spectrometers, Detectors and Associated Equipment*, 759:23–28, 2014.

[61] Mercedes López Noriega. *Pion interferometry in AuAu collisions at a center of mass energy per nucleon of 200 GeV.* PhD thesis, The Ohio State University, 2004.

[62] W.Betts et al. M.Anderson, J.Berkowitz. The star time projection chamber: A unique tool for studying high multiplicity events at rhic2. *arXiv:nucl-ex/0301015*.

[63] Stanislaw Mrowczynski. Quark-gluon plasma. *arXiv preprint nucl-th/9905005*, 1999.

[64] Takafumi Niida. Measurements of quantum interference of two identical particles with respect to the event plane in au+au collisions at a center of mass energy of 200 gev at rhic-phenix. Dissertation thesis, University of Tsukuba, 2013.

[65] VA Okorokov. Lévy distributions for one-dimensional analysis of the bose–einstein correlations. *Advances in High Energy Physics*, 2017, 2017.

[66] Sandra S Padula. Hbt interferometry: Historical perspective. *Brazilian journal of physics*, 35(1):70–99, 2005.

[67] Jean-François Paquet, Chun Shen, Gabriel S Denicol, Matthew Luzum, Björn Schenke, Sangyong Jeon, and Charles Gale. Production of photons in relativistic heavy-ion collisions. *Physical Review C*, 93(4):044906, 2016.

[68] Scott Pratt. The long slow death of the hbt puzzle. *Nuclear Physics A*, 830(1-4):51c–57c, 2009.

[69] Scott Pratt. Resolving the hanbury brown–twiss puzzle in relativistic heavy ion collisions. *Physical review letters*, 102(23):232301, 2009.

[70] F Retiere, STAR collaboration, et al. Non-identical particle correlation analysis as a probe of transverse flow. *Nuclear Physics A*, 715:591c–594c, 2003.

[71] Fabrice Retiere and Michael Annan Lisa. Observable implications of geometrical and dynamical aspects of freeze-out in heavy ion collisions. *Physical Review C*, 70(4):044907, 2004.

[72] Baldo Sahlmüller, ALICE Collaboration, et al. Direct photon measurement in pb–pb collisions at snn= 2.76 tev with alice. *Nuclear Physics A*, 956:421–424, 2016.

[73] Michal Sumbera. Selected results on strong and coulomb-induced correlations from the star experiment. *Brazilian Journal of Physics*, 37(3A):925–932, 2007.

[74] MJ Tannenbaum. Highlights from bnl and rhic 2015. In *THE FUTURE OF OUR PHYSICS INCLUDING NEW FRONTIERS: Proceedings of the International School of Subnuclear Physics*, pages 393–412. World Scientific, 2017.

[75] Markus H. Thoma Thomas Peitzmann. Direct photons from relativistic heavy-ion collisions. *arXiv:hep-ph/0111114*, 2002.

[76] David Tlustý. Study of open charm production in p+p collisions at star. Dissertation thesis, Czech Technical University in Prague, 2014.

[77] Boris Tomasik and Urs Achim Wiedemann. Central and non-central hbt from ags to rhic. *arXiv preprint hep-ph/0210250*, 2002.

[78] Boris Tomasik and Urs Achim Wiedemann. Central and non-central hbt from ags to rhic. In *Quark-Gluon Plasma 3*, pages 715–777. World Scientific, 2004.

[79] CD White. The cornell potential from general geometries in ads/qcd. *Physics Letters B*, 652(2-3):79–85, 2007.

[80] CA Whitten Jr and STAR Collaboration. The beam-beam counter: A local polarimeter at star. In *AIP Conference Proceedings*, volume 980, pages 390–396. AIP, 2008.

[81] CA Whitten Jr, Ahovi Kponou, Yousef Makdisi, and Anatoli Zelenski. The beam-beam counter: A local polarimeter at star. In *AIP Conference Proceedings*, volume 980, pages 390–396. AIP, 2008.

[82] Urs Achim Wiedemann and Ulrich Heinz. Particle interferometry for relativistic heavy-ion collisions. *Physics Reports*, 319(4):145–230, 1999.

[83] Urs Achim Wiedemann, Pierre Scotto, and Ulrich Heinz. Transverse momentum dependence of hanbury-brown–twiss correlation radii. *Physical Review C*, 53(2):918, 1996.

[84] Yi-Fei Xu, Jin-Hui Chen, Yu-Gang Ma, Ai-Hong Tang, Zhang-Bu Xu, and Yu-Hui Zhu. Physics performance of the star zero degree calorimeter at relativistic heavy ion collider. *Nuclear Science and Techniques*, 27(6):126, 2016.

[85] Kohsuke Yagi, Tetsuo Hatsuda, and Yasuo Miake. *Quark-gluon plasma: From big bang to little bang*, volume 23. Cambridge University Press, 2005.

[86] Chajecky Zbigniew. *Global conservation laws and femtoscopy at RHIC*. PhD thesis, The Ohio State University, 2009.

[87] Hanna Zbroszczyk. Studies of baryon-baryon correlations in relativistic nuclear collisions registered at the star experiment. Dissertation thesis, Warsaw University of Technology, 2008.